

Faculty of Sciences
Department of Physics and Astronomy

A COMPREHENSIVE STUDY OF *TESS* MAIA STAR TIC 202431888

by

LISTER VIVIAN KGWATALALA
Student ID number: 21100034
BSc (Radiation and Health Physics) (UoB), MSc (BIUST)

A Dissertation Submitted to the Faculty of Sciences in Fulfillment of the Requirements for the Award of the Master of Science in Physics of BIUST

Supervisors:
Dr. Ceren Ulusoy
Department of Physics and Astronomy
Faculty of Sciences,
BIUST
ulusoyc@biust.ac.bw

Assoc. Prof. Ivanka Stateva
Bulgarian Academy of Sciences
Institute of Astronomy with National Astronomical Observatory
Rozhen, Bulgaria
stateva@astro.bas.bg

October 2024

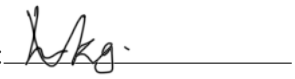
Declaration Regarding the Work and Copyright

Candidate: LISTER VIVIAN KGWATALALA
Student ID: 21100034

Thesis Titled: A Comprehensive Study of *TESS* Maia star TIC 202431888.

I, the **Candidate**, certify that the dissertation is all my own original work and that I have not obtained a degree in this University or elsewhere on the basis of any of this work.

This dissertation is copyright material protected under the Berne Convention, the Copyright and Neighbouring Rights Act, Act. No. 8 of 2000 and other international and national enactments, in that behalf, on intellectual property. It must not be reproduced by any means, in full or in part, except for short extracts in fair dealing; for researcher private study, critical scholarly review or discourse with an acknowledgement, without the written permission of the office of the Postgraduate School, on behalf of both the author and the BIUST.

Signature: Date: 18/10/2024

Primary Supervisor: Dr. Ceren Ulusoy

I, the Candidate's **Primary Supervisor**, hereby confirm that I have inspected the above titled thesis and, to the best of my knowledge, it is based on the original work of the candidate.

Signature: Date: 18/10/2024

Contents

Acknowledgements ii

Dedication iii

Abstract iv

List of Figures v

List of Figures vii

List of Tables viii

List of Tables viii

List of Abbreviations ix

Research Output xii

1 Introduction 1

1.1 Context and Rationale 1

1.2 Problem Statement 3

1.3 Aim 5

1.4 Objectives 6

1.5 Thesis Outline 6

2 Literature Review 7

2.1 Classification of Variable Stars 7

2.1.1 Extrinsic Variables . . . 7
2.1.2 Intrinsic Variables . . . 10
2.2 Asteroseismology . . . 12
2.2.1 Modal Behaviour of Pulsating Stars . . . 13
2.2.2 Driving Mechanisms . . . 18
2.3 GAIA HR Diagram and Maia Stars . . . 22
2.3.1 Evolution of Massive Stars . . . 23
2.3.2 B-type stars . . . 26
2.3.3 A-Type Stars . . . 28
2.4 Maia-type stars . . . 29
2.4.1 Existence of the presumed Maia stars . . . 29
2.4.2 Pulsations in Maia stars: Justifications . . . 31
2.5 Asteroseismological studies of B-type stars . . . 34
2.6 Hypotheses for Anomalous Pulsations . . . 35
2.6.1 Rapid Rotation Hypothesis . . . 35
2.6.2 Binary Hypothesis . . . 36
2.6.3 Observational Uncertainties Hypothesis . . . 36
2.7 Challenges to Current Models . . . 36

3 Spectroscopy and Photometry **38**

3.1 Introduction . . . 38
3.2 Spectroscopy . . . 38
3.2.1 Spectral Classification . . . 38
3.2.2 Stellar Parameters . . . 42

3.2.3 Stellar Atmospheres . . . 46
3.2.4 Observational Effects . . . 53
3.2.5 Model Atmospheres . . . 55
3.2.6 Spectral Energy Distribution (SED) Analysis with VOSA . . . 59
3.3 Photometry . . . 60
3.3.1 Transiting Exoplanet Survey Satellite-*TESS* . . . 60
3.3.2 Band-pass . . . 61

4 Data Analyses **63**
4.1 Frequency Analysis of TIC 202431888 . . . 63
4.2 Ground-based Spectroscopic Observations . . . 67
4.2.1 Spectroscopic Data Analysis of TIC 202431888 . . . 67
4.2.2 The location of TIC 202431888 on the HR Diagram . . . 70

5 Summary, Discussion and Conclusions **72**
5.0.1 Summary . . . 72
5.0.2 Discussion on the MAIA Classification Conundrum . . . 75
5.0.3 Conclusions . . . 77

Bibliography **78**
Appendix A . . . 88

Acknowledgements

I would like to express my deepest gratitude to my thesis advisor Dr. Ceren Ulusoy, for her unwavering guidance, mentorship, patience, kindness, and continuous motherly support throughout the entire research process. The expertise, encouragement and commitment have been instrumental in shaping this thesis. You have indeed opened a door for me. To my Co-Supervisor Prof. Ivanka Stateva, thank you for the constructive feedback, thoughtful contributions as it was a great impact for a successful completion of this study.

I am profoundly thankful to The NAO-Rozhen Observatory, Bulgaria for their generous time allocation, the dedicated effort in observations, and the provision of valuable data that made this study possible. All this was made possible by my Co-supervisor Prof. Ivanka Stateva. The resources and support provided by the observatory have significantly contributed to the success of this research. I am also grateful to the Botswana International University of Science and Technology for providing an academic environment and access to resources essential for the completion of this research. Special thanks to the staff and faculty who have been supportive throughout my academic journey.

Heartfelt thanks to my family and friends for their encouragement, understanding, financial support and above all a mother's love. A special note of appreciation goes to Mr Trust B Khohliwe, who stood by me during the challenging phases of this academic journey. There were times when I contemplated quitting, felt reluctant to come to school, and even experienced moments of depression. Mr Khohliwe played an invaluable role in keeping me grounded, providing unwavering support with bible sessions, prayer and being a constant source of strength.

I acknowledge the grace of God, my faith has been a constant source of solace and resilience.

Dedication

To my mother and grandmother, who dedicated their lives to shaping me into the person I am today.

Abstract

We present a detailed study of Maia type variable star, TIC 202431888 observed by the *TESS* satellite (Ricker et al., 2015) for the first time in literature. A new group of variable stars with late B or early A-type characteristics was initially proposed based on radial velocity observations of the prototype star, Maia, which is a member of the Pleiades star cluster as indicated by Struve (1955) and by Struve et al. (1957). During the following years, several studies also identified a short list of possible Maia candidates, but they were later classified into different variability groups. Maia variables are characterized by multiple high frequencies that occur between the red edge of the β Cephei and the blue edge of the δ Scuti instability strips. It is possible that these stars are being driven by a pulsating mechanism that is not yet understood, and the high frequencies observed in late B-type stars still lack an explanation based on our current knowledge. However, stellar variability is being rediscovered by recent space missions like *TESS* through analysing unprecedented data sets, allowing for the detection of oscillations with very low amplitudes and they have been promising in solving the classification puzzle of Maia phenomenon among B-type stars.

This study aims to examine common characteristics of Maia variables (MAIA) to investigate comparable or distinct features in the star TIC 202431888 listed among the classified Maia stars by Balona & Ozuyar (2020). For this reason, the *TESS* photometry and high-dispersion ground-based spectroscopy were used. Spectroscopic observations were obtained with the 2-m RCC telescope at Rozhen, Bulgaria. From the spectroscopic observations, the atmospheric parameters, the projected rotational velocity $v \sin i$, and chemical abundance of selected elements of TIC 202431888 were determined as well as the evolutionary track of the star in the HR diagram has been presented. The frequency analysis of the *TESS* photometry resulted in the detection of the two highest peaks at $f_1 = 19.32\ d^{-1}$ and $f_2 = 22.10\ d^{-1}$, along with a few combinations and harmonics. Our results indicate that TIC 202431888 is a Maia-type variable star with low amplitude and high frequency values exceeding 5 d^{-1}, and its stellar parameters are in line with those observed between δ Scuti and B-type variables, which are classified as MAIAU by Balona (2023a). Also, we are in agreement that MAIA should continue to refer to these stars by their observed distinctive features, which are contrary to current models, until accurate classification distinctions for instability regions are established (Balona, 2023a).

List of Figures

1.1 The positioning of SPB/δ Cephei hybrids, SPB, Maia, δ Cephei in the HR diagram (Balona et al., 2015a). 2

1.2 The plot of period against effective temperature of pulsating stars (Balona & Ozuyar, 2020). 5

2.1 Classification of variable stars adopted from Eyer & Mowlavi (2008). 8

2.2 Phases of a spectroscopic binary system characterized by circular orbits on a 30-day orbital period (hypothetical) Bradt (2008). 9

2.3 Variable stars in the HR diagram (Christensen-Dalsgaard, 2004) . . . 11

2.4 Phase diagrams of OBAF-type pulsators on the MS (De Ridder et al., 2023). 12

2.5 A 3D simulation of convection inside a large star Anders et al. (2023) 13

2.6 Hydrostatic equilibrium inside a MS star (Mr Toogood's Physics, 2023), the components of the equation (Davies, 2023). 14

2.7 The star's g-mode propagations (Aerts et al., 2010). 16

2.8 The star's p-mode propagation's Aerts et al. (2010). 17

2.9 Opacity curve as a function of temperature (Kippenhahn et al., 1990). 19

2.10 HR diagram derived from Gaia Data Release 2 observations (Collaboration et al., 2018). 22

2.11 Spectroscopic evolution of massive pulsating stars in the HR diagram by *TESS* (sectors 1–13) adopted from Burssens et al. (2020). 26

2.12 The amplitude distribution in δ Scuti and Maia star (Balona, 2023a). 30

2.13 The distribution of $v \sin i$ for Maia variables among MS stars and Maia/SPB stars in the same temperature range (Balona, 2023a). . . . 33

3.1 The Morgan-Keenan Spectral Types summary (Bruce MacEvoy, 2013). 39

3.2 From left to right:Continuous Spectrum, Emission Spectrum, and Absorption Spectrum (NASA, 2021). 41

3.3 Energy levels of a H atom (Winckel, 2016). 42

3.4 An illustration of emission line (right) and an absorption line (left) for BAT99 126 (Janssens et al., 2021). 49

3.5 Element abundances as a function of the nuclear mass number (A) (Karttunen et al., 2007). 49

3.6 Variations in Absorption Lines across stars with different temperatures (CNX, 2023). 50

3.7 Illustration of a spectrum showing the spectral lines (FROGS, 2023). 50

3.8 The components of an absorption line showing EW illustrated in grey adopted from (Letarte, 2007). 51

3.9 The *TESS* spectral response function (black line) along with Johnson-Cousins and SDSS z filter curves for comparison (Ricker et al., 2015). 62

4.1 The normalized *TESS* data for the star TIC 202431888 available in the sectors 57 and 58. 64

4.2 The computed amplitude spectra of TIC 202431888 from the *TESS* photometry in the sectors 57 and 58. 66

4.3 2m RCC telescope at NAO-Rozhen IANAO,PenchoMarkishki (2023). 67

4.4 The observed (dots) and synthetic (solid line) spectra of TIC 202431888 for the Balmer line, Hα. 68

4.5 The same as in Fig 4.4 but for the region of He I λ 4471 Å and Mg II λ 4481 Å. 68

4.6 The same as in Fig 4.4 but for the region around λ 4500 Å. 69

4.7 The evolutionary track of TIC 202431888 and its location. 71

5.1 A comparison of Projected rotational velocities for Maia, β Cephei and SPB-type stars in the same effective temperature range. 73

5.2 The location of certain pulsating stars in the H-R diagram. Solid Lines refer to Zero-Age Sequence Models from Bertelli G. (2009). . . 75

List of Tables

3.1 Distinctive spectral lines at their temperature ranges (Collaboration, 2023). 52

3.2 Wavelengths of various elements for specitic spectral lines (Collaboration, 2023). 53

4.1 *TESS* Input Catalogue Parameters given for TIC 202431888. 63

4.2 Parameters of the resulting frequencies of TIC 202431888. 66

5.1 Orbital Paramets from SB9 74

List of Abbreviations

β Beta

δ Delta

γ Gamma

κ Kappa

H Hydrogen

C: Carbon

O: Oxygen

P: Phosphorus

S: Sulfur

Si: Silicon

Ti Titanium

Fe Iron

Cr Chromium

Ga Gallium

Na Sodium

Al: Aluminum

Ca: Calcium

Sc: Scandium

Ni: Nickel

Ba Barium

Mg: Magnesium

Mn: Manganese

TiO Titanium Oxide

HgMn Mercury-Manganese

Sr, Y, Zr Strontium, Yttrium, Zirconium

MS Main Sequence

CU Gaia Coordination Unit for Variability Processing

HD Henry Draper (Catalog)

EW Equivalent Width

RA Right Ascension

DEC Declination

OBJ OBJECT

HR Hertzsprung-Russell

O-C Observed–Calculated diagram

O-C Parts per thousand

SPB Slow Pulsating B-type

KIC Kepler Input Catalog

DS9 SAOImage DS9, SAOImage refers to the Smithsonian Astrophysical Observatory (SAO), DS9 is the ninth version of the software.

EBs Eclipsing Binaries

SBs Spectroscopic Binaries

SB1s Single-lined spectroscopic binaries

SB2s Double-lined spectroscopic binaries

CNO Carbon-Nitrogen-Oxygen

LTE Local Thermal Equilibrium

SED Spectral energy distribution

RoAp Rapidly oscillating Ap

TESS Transiting Exoplanet Survey Satellite

SDSS Sloan Digital Sky Survey

VALD Vienna Atomic Line Data Base

NASA National Aeronautics and Space Administration

ZAMS Zero Age Main Sequence

MAST Mikulski Archive for Space Telescopes

IRAF Image Reduction and Analysis Facility

TH-AR THORIUM-ARGON

HFOSC Himalaya Faint Object Spectrograph and Camera

FWHM Full Width at Half Maximum

CoRoT Convection, Rotation, and Planetary Transits

ET And Variable designation (ET) of an Andromeda constellation

SIMBAD Set of Identifications, Measurements, and Bibliography for Astronomical Data

BAT99 126 One rare multiple system of massive stars

MAIA Maia Variables

Barycenter The barycenter is the common center of mass around which two or more celestial bodies, such as stars or planets, orbit. It is the point where the combined mass of the system can be considered as concentrated.

Scientific Output

Conference presentations

1. **Lister Kgwatalala**; Ceren Ulusoy; Ivanka Stateva, XXXII IAU General Assembly, held 6-15 August, 2024 in Cape Town, South Africa Online at https://astronomy2024.org/wp-content/uploads/2024/07/Abstracts-book_July30.pdf

2. F. Z.; Squicciarini, V.; Ulusoy, Ceren ; **Kgwatalala, L.**; King, C.; Bonavita, M., 3rd Annual Conference of the African Astronomical Society (AfAS-2023), held 13-17 March, 2023 in Johannesburg, South Africa. Online at (Majidi et al., 2023)

3. Ulusoy, C.; Franchi, F.; Mpoeleng, D.; Mosalaosi, M.; Majidi, FZ.; Mabusha, K.; Kgomotso, T.; **Kgwatalala, L.**; King C, 3rd Annual Conference of the African Astronomical Society (AfAS-2023), held 13-17 March, 2023 in Johannesburg, South Africa. Online at (Ulusoy et al., 2023)

Chapter 1

Introduction

1.1 Context and Rationale

Variable stars have been instrumental in astrophysical research, providing insights into the dynamic and evolving nature of celestial objects (Hoffmeister & Kholopov, 1985; Sterken & Jaschek, 1996; Percy, 2007; Aerts, 2021). They are characterized by changes in their brightness, and/or other observable properties for example variations occuring at regular intervals (periodicity) over time, with fluctuations ranging from minuscule to substantial. These variations give a general understanding of the concept of variable stars, emphasizing the concept of stars as dynamic entities that can change their light output depending on the observer's perspective. Variations in apparent brightness are the primary criterion for identifying a variable star, but chemical structural changes within a star can also cause variations and alter the spectrum of the star. These elements collectively contribute to the distinctive rhythm of each star's performance, akin to a cosmic dance. Binaries, pulsating and eruptive stars are among the intriguing members of this class.

Pulsating stars, a significant subset of variable stars, exhibit rhythmic expansions and contractions, causing their brightness to oscillate periodically. This phenomenon is profoundly insightful, especially when contextualized within the Hertzsprung-Russell (HR) diagram, a fundamental tool in stellar astrophysics. The HR diagram plots stars based on their luminosity and temperature, effectively illustrating the life cycle and evolutionary phases of stars. The instability strip is a specific region where pulsating stars occupy, and it illustrates distinct patterns that reveal crucial information about their internal structures, evolutionary paths, and potential deaths (Catelan & Smith, 2015).

Asteroseismology refers to the study of variable stars with pulsations. It involves the study of stellar oscillations or seismic waves within stars (Aerts et al., 2010). By studying the natural oscillations in a star's brightness or spectra, researchers can decipher valuable information about its internal characteristics, including density, temperature, and chemical composition. This profound insight aids in validating

theoretical stellar models and refining our comprehension of stellar evolution, particularly for stars similar to the Sun. Asteroseismology offers a unique avenue to unravel the mysteries of exoplanetary systems, as oscillations can be influenced by the existence of planets orbiting around the star and the interiors of stellar across the HR diagram (Kurtz, 2022).

Along the zero-age main sequence (ZAMS) and the instability regions of β Cephei and SPB pulsating stars, there appears to be an unexplained region of variability. It is conceivable that there is an unidentified pulsating mechanism in these stars, and the high frequencies in late B-type stars are not yet understood. This region, situated on the cooler side of the β Cephei strip, is of significant interest for researchers, and its boundaries are defined by SPB stars. Maia-type stars also lie within this region as shown in Fig 1.1, and follow-up high-resolution spectroscopic observations can help to resolve questions related to unusual frequency patterns and period variations observed in late B-type and early A-type stars (Balona, 2023a). By exploring this intriguing aspect of early-type stars, we aim to enhance our knowledge of stellar evolution and improve the accuracy of theoretical models to observations (Balona, 2023b), thereby contributing to a deeper understanding of the broader astrophysical processes.

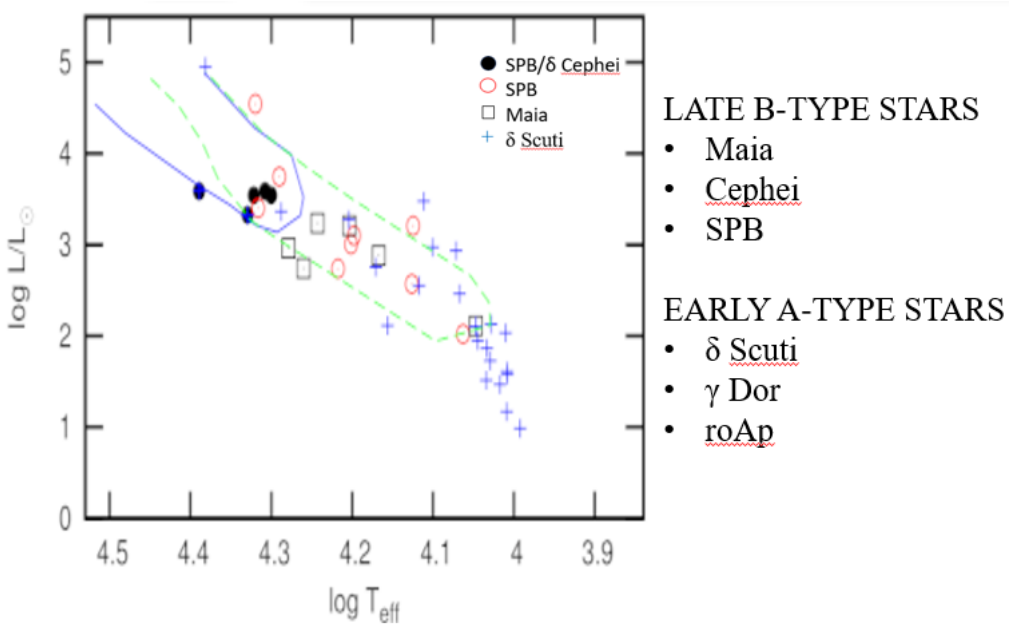


Figure 1.1: The positioning of SPB/δ Cephei hybrids, SPB, Maia, δ Cephei in the HR diagram (Balona et al., 2015a).

The theoretical HR diagram in Fig 1.1 depicts the positioning of SPB/δ Cephei hybrids with spectroscopic attributes as filled circles in black. Open circles in red indicate SPB stars with spectroscopic parameters, while open squares in black rep-

resent anomalous stars displaying high frequencies, referred to as Maia variables. Stars that do not pulsate, denoted by neither SPB, β Cephei, nor Maia classification, are represented by plus signs in blue. The continuous enclosed line indicates the theoretical instability strip for δ Cephei variables, while the dashed region indicates the theoretical instability strip for SPB variables.

1.2 Problem Statement

B-type stars, which exhibit spectral similarities to Maia stars, occupy the upper region of the HR diagram, characterized by surface temperatures ranging from approximately 10 000 to 30 000 K (Catelan & Smith, 2015). They are known for their high luminosities, which can range from tens to hundreds of thousands of times that of the Sun. Their high luminosity and relatively short lifespans make them invaluable in studying the early universe, providing insights into the formation and evolution of galaxies and the interstellar medium. Recent investigations have uncovered a diverse range of physical properties in B-type stars, including variations in chemical composition, rotational velocities, and pulsational behavior (De Ridder et al., 2023). These characteristics are strongly influenced by the intricate physical processes occurring within their interiors, such as nuclear fusion, convection, and magnetic fields.

Occasionally, ground-based observations have suggested the probable existence of high frequencies in some particular stars. The stars under consideration exhibit temperatures that do not meet the criteria for classification as δ Scuti stars or β Cephei stars (McNamara, 1985; Lehmann et al., 1995; Percy & Wilson, 2000; Kallinger et al., 2002). The stars in question were originally classified as Maia variables, a term derived from a study conducted by Struve (1955), which that documented the presence of short-term fluctuations in Maia, one of the stars inside the Pleiades cluster. Nevertheless, Struve subsequently renounced the notion of such variability (Struve et al., 1957). The recent observations conducted during the *Kepler/K2* space mission provided new insights. It was disclosed that Maia exhibits rotational variability with a period of 10 days and lacks high-frequency characteristics (White et al., 2017).

The development of a new category of low-amplitude B-type pulsators located between the SPB and δ Scuti instability areas is considered to be one of the most intriguing outcomes of the *CoRoT* mission The stars under consideration exhibit a remarkably broad range of frequencies, including those found in the β Cephei

frequency range (Degroote et al., 2009), and it is likely that they have similar associations with the Maia variables. Moreover, it has been shown that within the *Kepler* field, there exist B-type stars exhibiting high frequencies that do not meet the criteria for classification as β Cephei variables (Balona et al., 2015b, 2016). The irregular high frequencies in fast rotating late to mid-B stars were discovered by ground-based photometric observations done by Mowlavi et al. (2013), Lata et al. (2014) and Mowlavi et al. (2016). At present, there is a lack of clarity regarding the definitive classification of these stars as Maia variables. According to a study conducted by Salmon et al. (2014), which employed pulsating models to examine rotating B-type stars, it is proposed that frequencies of up to 10 d^{-1} might potentially be detected in mid- to late B-type stars. The proposed hypothesis posits that the observed stars may belong to the category of fast-rotating SPB stars, characterized by a reduction in apparent effective temperature resulting from gravity darkening specifically at the equatorial region. The study conducted by Szewczuk & Daszyńska-Daszkiewicz (2017) investigated instability regions in B-type stars, with a focus on the impact of slow-to-moderate rotation. According to their study, the presence of unstable prograde high-order gravity modes could be a possible explanation for the anomalous variables and Maia stars.

Placing Maia variables in the HR diagram is an intriguing challenge because of their unusual characteristics compared to B-type stars, which are found within the instability strip. Questions arise about the location of Maia stars as follows.

- How do they, with their unique pulsation behaviors, fit within the intricate framework of the HR diagram?
- Are they closely aligned with typical B-type stars, sharing the same spectral characteristics?
- Or do they exhibit deviations that position them in a distinct region?

Figure 1.2 shows the frequency of maximum amplitude for each star, with the size proportional to the logarithm of the amplitude. Two elliptical regions depict the predicted locations of low-degree unstable modes according to Miglio et al. (2007). The positions adopted for β Cephei, SPB, Maia, δ Sct, and γ Doradus (Dor) stars are outlined by dashed lines as an example of the T_{eff} problem depicting the overlap of the variables in this temperature range.

Precisely determining the location of Maia stars on the HR diagram is vital to unravel the mysteries surrounding their pulsation behaviors, their role in high-mass

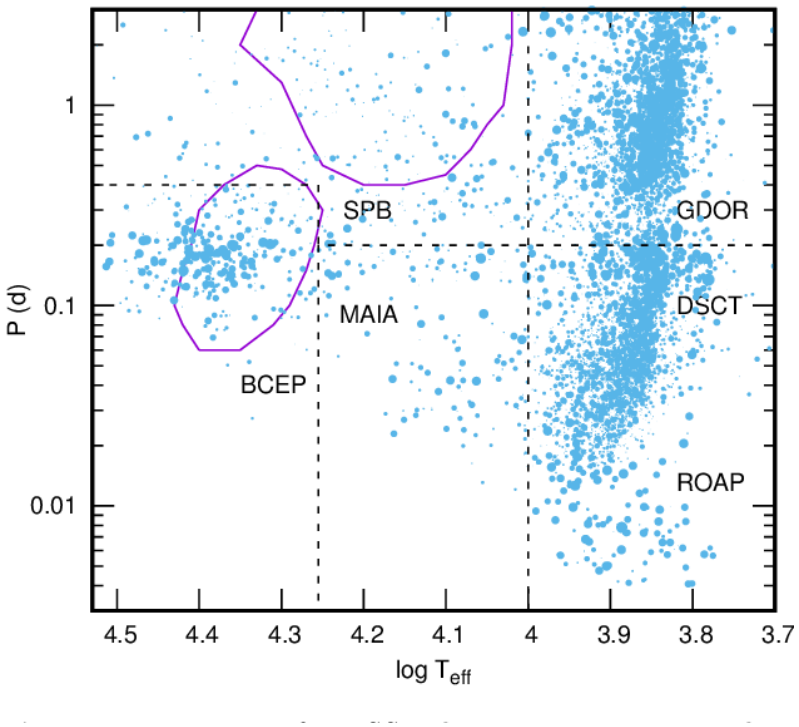


Figure 1.2: The plot of period against effective temperature of pulsating stars (Balona & Ozuyar, 2020).

star evolution, and their contributions to our understanding of the Universe's cosmic tapestry.

1.3 Aim

The purpose of this study is to examine the common characteristics of Maia variables (MAIA) and to determine if there are any comparable or distinct features in the star TIC 202431888, which was included in the classification of Maia stars by Balona & Ozuyar (2020). The characteristics of the selected target were investigated in a detailed way using *TESS* photometry and high-dispersion ground-based spectroscopy, which is the first time they have been studied in literature. The study seeks to explore the nature of the high-frequency pulsations observed in this late B-type star, which are not fully explained by current models, and to contribute to the understanding of the Maia phenomenon among B-type stars by analyzing both photometric and spectroscopic data.

1.4 Objectives

The objectives of this study is to:

- Conduct a comprehensive study of a selected Maia-type star candidate, situated within the instability strip to precisely determine their atmospheric characteristics, chemical composition, and internal structures.
- Investigate the reasons behind the absence of stellar pulsations in the concentrated band of the instability strip and explore how it impacts the evolutionary tracks and theoretical pulsation frequencies of early-type stars.
- Analyze the spectroscopic properties of the candidate Maia star in relation to their location on the HR diagram and their association with the cooler edge of the Cepheid strip, while also examining their boundaries defined by SPB-type stars (53 Persei stars) and δ Scuti stars.

1.5 Thesis Outline

Chapter 1 provides an overview of the research context, problem statement, objectives, and the structure of the thesis.

Chapter 2 reviews existing knowledge on variable stars, classification, asteroseismology, HR diagrams, and Maia-type stars.

Chapter 3 covers the significance of spectroscopy and photometry in studying variable stars, along with techniques, observations, and key instruments.

Chapter 4 presents data analyses of *TESS* photometry and ground-based spectroscopic observations.

Chapter 5 summarizes research results, discusses the the Maia classification conundrum, and makes conclusions.

Chapter 2

Literature Review

This chapter provides an introduction of the presumed Maia stars as intrinsic pulsating variables, their hypothesised driving mechanisms and their anticipated evolutionary path along the HR diagram based on literature.

2.1 Classification of Variable Stars

A star is classified as variable when its brightness fluctuates due to changes in its luminosity (Raman, 1964; Hoffmeister & Kholopov, 1985). Henrietta Leavitt (Mitchell, 1976) discovered over 2000 variable stars between 1907 and 1921, prior to her work of analyzing photographic plates. Leavitt was first assigned the task of examining the photographic plates to evaluate the brightness of stars. To make these comparisons, she frequently placed one plate onto another to examine how the star's brightness varied between exposures which produced significant knowledge to the nature of the Universe (Mariani, 2012). As a result, these changes in brightness differ, hence why there are different types and groups of variables.

The light curve forms of variables can be categorized into three groups: regular, semi-regular, and irregular. Contrary to irregular light curves, regular light curves recur throughout time with a clearly defined periodicity. Between these two categories of variability, there are semi-regular variables, which frequently have some repeatability. Variable stars were later classified into two main types, extrinsic and intrinsic, according to their observable characteristics, to improve our understanding (Motz & Weaver, 1989). In Fig 2.1, a variability tree diagram is presented, depicting various types of variable stars as well as their classifications.

2.1.1 Extrinsic Variables

Extrinsic variables are a fascinating group of celestial objects that exhibit fluctuations in brightness over time due to external factors such as eclipses, transits, and gravitational microlensing. These variations are typically caused by the presence



Figure 2.1: Classification of variable stars adopted from Eyer & Mowlavi (2008).

of another celestial body, such as a companion star, planet, or dust cloud, that affects the observed light from the primary star. Extrinsic variables have garnered significant attention in recent years, leading to a deeper understanding of their properties and their impact on our understanding of astrophysical phenomena (Sterken & Jaschek, 1996; Eyer & Mowlavi, 2008).

In the following section, we focus exclusively on spectroscopic binary stars, with the aim of providing an introduction to the properties of spectroscopic binary stars due to the spectroscopic binarity feature of the selected target, TIC 202431888, in the thesis.

2.1.1.1 Spectroscopic Binaries

Spectroscopic binaries are binary stars that can be classified as variable stars. The Doppler shifts of spectral lines indicate periodic oscillations in the radial velocity of the components in a binary system. If two sets of spectral lines oscillate in opposing directions in a star's spectrum, the star is classified as a double-lined spectroscopic binary. On the other hand, a star is referred to be a single-lined spectroscopic

binary if there is only one pair of lines. Certain intrinsic variable stars also exhibit cyclic changes in their radial velocity (Prša, 2006). However, they have distinct velocity and light curve properties that distinguishes them from the group of single-lined spectroscopic binaries. Observations of radial velocity show the presence of spectroscopic binaries. The more luminous component of such a binary system displays a continuously changing periodic velocity, causing rhythmic alterations in the wavelengths of its spectral lines.

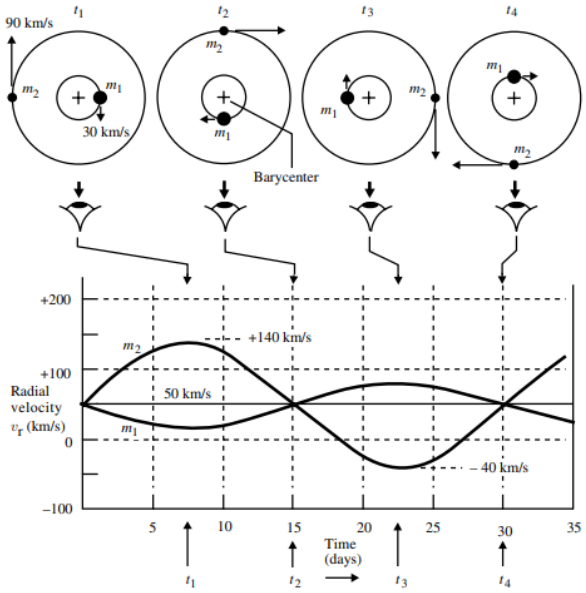


Figure 2.2: Phases of a spectroscopic binary system characterized by circular orbits on a 30-day orbital period (hypothetical) Bradt (2008).

Fig 2.2 shows four phases of a hypothetical spectroscopic binary with circular orbits and a 30-day period. The observer is in the orbit's plane. The mass of star 1 is three times that of star 2. The two stars are always on opposing sides of the barycenter, which is traveling away from the viewer at a constant radial velocity component of +50 km/s. In the upper left, the star speeds relative to the barycenter are displayed. Star 2 is three times farther out from the barycenter than star 1 due to its smaller mass; as a result, it must travel three times quicker to complete the orbit in the same amount of time as star 1. The astronomer's direction and observed Doppler velocities are displayed (Bradt, 2008). The non-relativistic Doppler shift offers a useful approximation, it is commonly used for binary systems that include normal stars (Bradt, 2008). Spectral double lines or Keplerian motion clearly indicate the binary nature (double lines). A curve representing radial velocity can be created by plotting radial velocities against time after converting wavelength shifts to radial velocities. Each binary system has a different radial velocity curve shape, which is determined by the orbital elements. It may only be feasible to detect spectroscopic

binary systems with two distinct sets of spectral lines (SB2s) when the two stars are at their greatest velocity separation, as the identification of this type is highly dependent on the resolution of the spectral lines. The secondary star is difficult to identify because of the possible fact that the companion is significantly less than the primary. It is clear that the observer's relative orientation is just as significant as the stars' orbital characteristics in these groups. An apparent orbit is the path that the stars appear to take in the sky when one estimates the location at different times during the orbital motion. In cases where the tilt of a binary system's orbit can be measured, such as eclipsing and visible binaries, it is possible to derive valuable information about the system's geometry and dynamics (Kamilla et al., 2011). Another way to measure an orbit is in relation to a star or the system's centre of mass. An orbit may also be measured relative to one of the stars or relative to the centre of mass of the system.

2.1.2 Intrinsic Variables

Intrinsic variables refer to stars that exhibit changes in brightness due to internal processes within the stellar interiors. These variables are very significant and valuable type of stars for astronomers since they provide a vast amount of information on the inner structure and models of stars. There are further categories for intrinsic variables depending on whether they show periodic pulsations or more explosive or eruptive occurrences (Levy, 1998).

2.1.2.1 Pulsating Stars

Pulsating stars regularly expand and contract their surface layers affecting the star's overall size and shape as well as their effective temperature and spectral characteristics. A pulsating star can also have non-radial pulsations, which are not centred on a central point and causing the star's form to sometimes diverge from a sphere, or radial pulsations, which revolve around a single point and keep the geometry of the star spherical. There are several pulsating star types illustrated by Fig 2.3 with various light curve characteristics as shown in Fig 2.4 (Catelan & Smith, 2015).

A schematic representation of the HR diagram in Fig 2.3 presents the positions of various groups of pulsating stars. In the diagram, the ZAMS is denoted by a dashed line, while continuous curves represent selected evolutionary tracks at different Solar masses ($M_{\odot}$). The horizontal branch is marked by a triple-dot-dashed line, and the

cooling curve for white dwarf stars is depicted by a dotted curve.

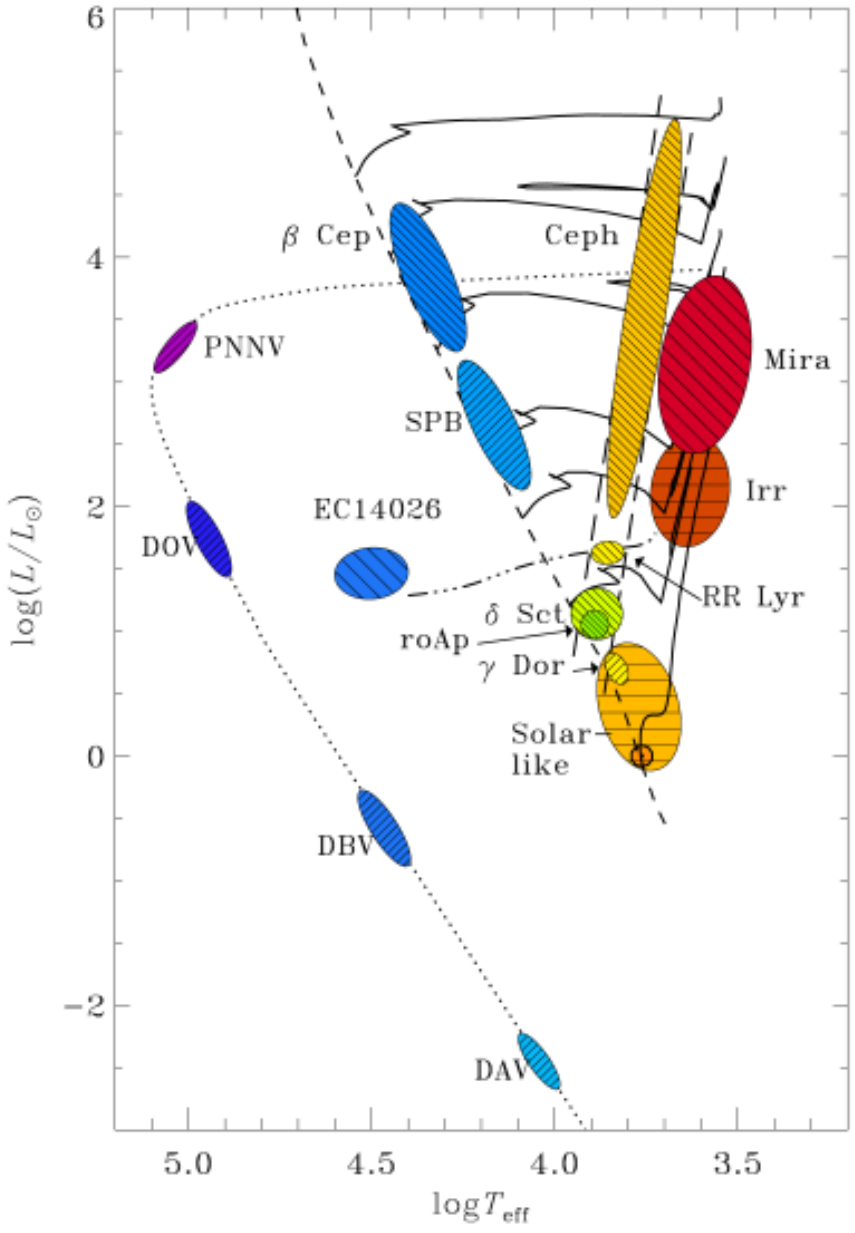


Figure 2.3: Variable stars in the HR diagram (Christensen-Dalsgaard, 2004)

Fig 2.4 below shows phase diagrams illustrating stars categorized as OBAF-type pulsators on the MS. The basic frequency μ_1 found in Gaia G-band photometry is synchronised with the diagrams. Three distinct situations are represented by each row, which runs from top to bottom: stars designated as β Cephei, δ Scuti, γ Dor, and SPB, respectively.

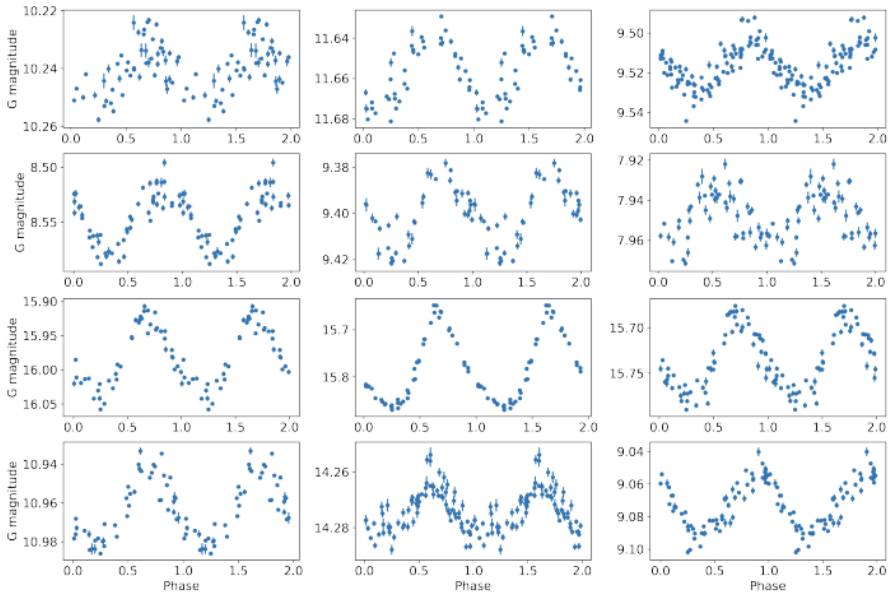


Figure 2.4: Phase diagrams of OBAF-type pulsators on the MS (De Ridder et al., 2023).

2.2 Asteroseismology

Asteroseismology, a captivating branch of astrophysics, endeavors to unravel the enigmatic internal structure and dynamics of stars by studying their intrinsic oscillations, or '*stellar music*'. Eddington's initial indication of this phenomenon in stars dates back to 1926 when he introduced the concept of stellar pulsation (Eddington, 1988). In his work, "The Internal Constitution of the Stars," published in the same year, he posed a fundamental question:

"At first sight it would seem that the deep interior of the Sun and stars is less accessible to scientific investigation than any other region in the universe. Our telescopes may probe farther and farther into the depths of space; but how can we ever obtain certain knowledge of that which is hidden behind substantial barriers? What appliance can pierce through the outer layers of a star and test the conditions within?"

In this context, during the mid-20th century, a novel idea emerged Asteroseismology. The introduction of new theories (Ledoux & Walraven, 1958) into stellar oscillations resulted in a unique understanding of the interiors of stars, and stellar seismology has become an essential tool for investigating celestial bodies beyond what can be directly observed. Fig 2.5 represents an example of a cutting-edge 3D simulation designed by scientists at Northwestern University to investigate how energy flows from the core to the surface of a massive star (Anders et al., 2023). This breakthrough

offers new perspectives on the characteristic twinkling of stars. Additionally, the research team transformed energy waves into sound, granting us the ability to listen to the internal dynamics of a star and its distinct twinkle.Below are different processes or techniques that are important to consider in order to study and analyze the periodic changes in a star's brightness '*twinkle*'.

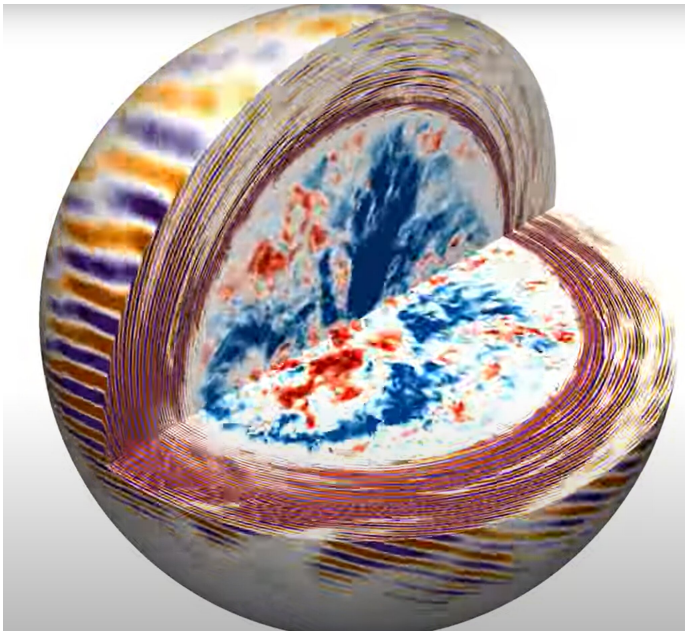


Figure 2.5: A 3D simulation of convection inside a large star Anders et al. (2023)

2.2.1 Modal Behaviour of Pulsating Stars

In general, stars are in hydrostatic equilibrium for most of their lifetimes; Mathematically, this state is expressed as:

$$\frac{dp}{dr} = -\frac{GM\rho}{r^2} \tag{2.1}$$

In this equation, m and (p) denote the mass and pressure contained within a certain radius r, while ρ refers to the density; G represents the gravitational constant (Cox, 2015). The prevailing belief is that the various pressures within a star counterbalance each other (hydrostatic equillibrum). Fig 2.6 clearly shows the gravity and expansion of the star that results in the hydrostatic equillibrum as well as the components of the equation 2.1 inside the MS star. However, this equation (2.1) does not account for all of the pertinent factors. As a result, stars do not strictly adhere to the conditions of hydrostatic equilibrium. In most cases, internal forces cannot be reconciled,

causing star matter to move due to local accelerations. A star's eigenmodes are typically classified as p, f, and g modes. These are pressure, gravity (buoyancy) and fundamental modes.

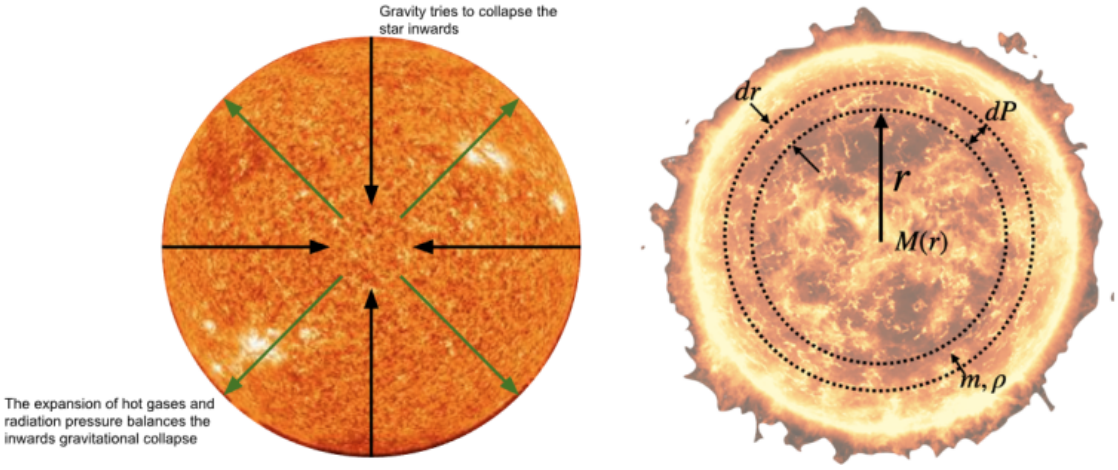


Figure 2.6: Hydrostatic equilibrium inside a MS star (Mr Toogood's Physics, 2023), the components of the equation (Davies, 2023).

Different types of stars, including SPB stars, β Cephei, γ Dor stars, δ Scuti stars, and rapidly oscillating Ap stars (roAp) [1]. The γ Dor stars pulsate in high-order gravity modes, while δ Scuti stars pulsate in low-order $p-$ and $g-$ modes. The $g-$ and $p-$ modes are explained in detailed on section 2.2.1.1. β Cephei stars pulsate in p-modes and gravito-inertial modes. SPB stars pulsate in gravito-inertial modes. RoAp stars pulsate in high-overtone magneto-acoustic modes (Kurtz, 2022). The strong magnetic fields influences the frequencies and characteristics of their pulsations. These modes arise from the interplay of internal forces, leading to the eigenmodes being typically classified as p, f, and g modes, representing pressure, fundamental and gravity (buoyancy) modes, respectively. The eigenmodes of stars are fundamental in characterizing their internal structure and behavior (Roxburgh, 2004). B- and A-type stars may exhibit mixed modes through the luminosity bump, both behaving like acoustic modes on the surface and like gravity modes in their core (Lindsay et al., 2022). Mixed modes occur in stars that are in the transition phase between the MS and the post-MS evolution.

In pulsating stars, buoyancy forces can lead to the excitation of various oscillation modes, such as gravity modes (g-modes) and pressure modes (p-modes). The Brunt-Väisälä frequency as a measure of the buoyancy forces present in a star's interior, which arise due to the variation of density with depth, determines the stability and

[1] roAp are a subset of magnetic chemically peculiar A-type (Ap) stars that exhibit rapid pulsations in their light curves stars, exhibit specific types of oscillation modes

behavior of oscillation modes within these celestial objects (Dhouib et al., 2021). The Brunt-Väisälä frequency is mathematically defined as:

$$N^2 = g\left(\frac{1}{\Gamma_1}\frac{d\ln P}{dr} - \frac{d\ln \rho}{dr}\right)$$

where:

- N^2 is the Brunt-Väisälä frequency,
- g is the local gravitational acceleration,
- P is the pressure,
- ρ is the density,
- Γ_1 is the adiabatic exponent.

This equation (2.2.1) encapsulates the interplay of pressure and density variations with depth in a star, and the resultant Brunt-Väisälä frequency provides a critical measure of the stability of different oscillation modes. It arises from the variation of pressure and density with radial distance (r) from the stellar center. If the Brunt-Väisälä frequency is positive ($N^2 > 0$), it signifies stability against vertical displacements, indicating that pressure modes can be excited within the star. Conversely, if the Brunt-Väisälä frequency is negative ($N^2 < 0$), it implies instability against vertical displacements, leading to the excitation of gravity modes (g-modes).

2.2.1.1 Gravity Modes (g-modes)

The g-modes also known as buoyancy and gravity are gravity modes that strive to reestablish the stars internal equillibrum, therefore these are basically internal modes of gravity inside a star. In areas where radiation is the primary means of energy transfer, gravitational modes are created. They specifically result from a fluid blob's upward adiabatic displacement. The fluid element and its surroundings have a variable density as a result of the displacement. If the square of the buoyancy (Brunt–Väisälä frequency) is greater than zero (Szabados & Kurtz, 2012), indicating that the component is heavier than the fluid that was displaced, the buoyancy will draw the blob back near its initial location. As a result, the element oscillates about its equilibrium location. Otherwise, the element is pushed out of equilibrium

by the buoyancy, which corresponds to convective instability. The blob is continuously being displaced in the convective zone. Because of this, standing waves are unable to develop in this area before finally disappearing (Christensen-Dalsgaard, 2003). The radiative zone of solar-like stars is located below the convective envelope. Gravity-modes are consequently restricted to the interior of the star since only modest amplitudes may reach the surface. Nevertheless, these modes are restricted beyond the convective core in the MS massive stars (Tarrant, 2010). With an increase in radial nodes, there is frequency reduction due to internal gravity modes of g-modes. Gravity modes, illustrated in Fig 2.7 are more frequently found in the center of stars, making them more susceptible to changes there. The diagram shows a g-mode with a frequency of $190\mu Hz$ and $l = 5$ (five nodal lines on the star's surface) is displayed. This g-mode is confined beneath the convective region, thereby containing insights into the core and radiative zone of the star.

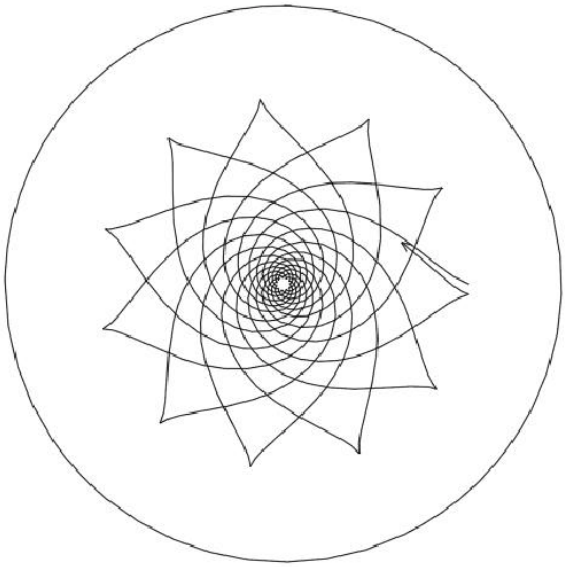


Figure 2.7: The star's g-mode propagations (Aerts et al., 2010).

2.2.1.2 Pressure Modes (p-modes)

The convective zone drives the radial movements of the star material in this sort of pulsation. Pressure is the restorative force that moves material from high-density to low-density areas. There has to be a cavity in order to create standing acoustic waves. At its edges, which differ from top to bottom, the waves are reflected. Near the top of the convective zone, resulting in a sudden drop in density and an exceedingly high acoustic cut-off frequency. The modes are situated between a turning point on the surface and one within,therefore almost all modes are internal

(Tarrant, 2010). The internal reflection of the pressure modes is made more understandable by the ray theory (Gough, 1984, 1986). A mode can be conceptualized as a collection of propagating sound waves. Since they are exposed to faster sound speeds, the deeper regions of the wave fronts propagate across the star faster. The propagation path diverges from the radial direction at the reflection point, though, and the wave travels horizontally there. From one mode to another, this trough's location in the cavity varies. A superposition of moving sound waves is referred to as a mode (Gough, 2012). Since they are exposed to faster sound speeds, the deeper parts of the wave fronts propagate across the star more swiftly. As a result, the wave propagates away from the reflection point and moves in a horizontal direction.

In this case, radial nodes are directly proportional to p-modes frequencies and an increase in the radial nodes number increases the p-modes frequencies. The frequencies appear to be similarly distributed according to the variational relation, in addition p-modes are more responsive to the star's surface conditions. There are clear formulae for the frequencies of p-modes in Adassuriya (2022).

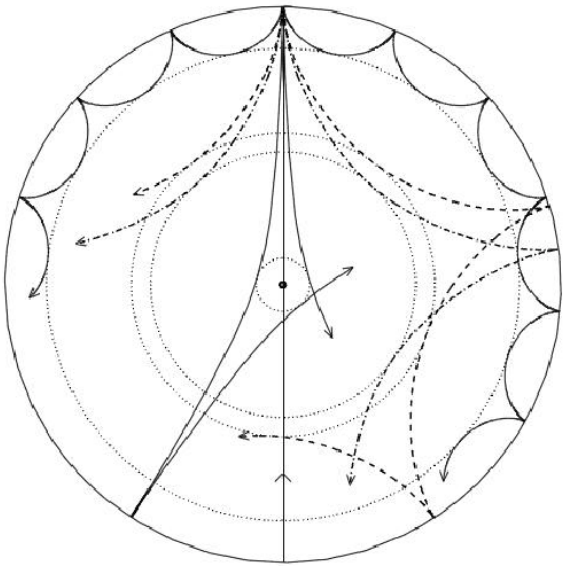


Figure 2.8: The star's p-mode propagation's Aerts et al. (2010).

The dashed circles in Fig 2.8 indicate the inner turning points where p-modes are refracted due to the rise in sound speed and subsequently reflected. Additionally, these acoustic waves experience reflection due to the rapid density decrease at the surface. The line intersecting the center represents the radial mode, while the others are p-modes of varying l values (75, 25, 20, and 2) with a frequency of $3\,000\mu Hz$, arranged in order of increasing depth.

In essence, both p- and g-modes have significant features. As mentioned radial nodes

are directly proportional to pressure modes frequencies and inversely proportional to gravity modes. While the g-modes include significant details about the deep interior, the p-modes provide information on the conditions in the star's outer area. If n (an integral value that describes the count of radial nodes in a pulsation mode) is greater than l, there is an exponential link for the two pulsation modes. As a result, pressure modes are approximately equally distributed apart, whereas g-modes show a rough space apart in frequency and period (Aerts et al., 2010). In addition, although pressure modes have periods that are equivalent to or less than those of the radial fundamental mode, gravity modes frequently pulsates with durations that are longer than those of the latter. Therefore, it is evident that radial pulsations always operate in pressure mode (Handler et al., 2004).

2.2.2 Driving Mechanisms

The pulsation mechanism in stars operates through the equilibrium between gravitational force and pressure. In a normal star, gravity pulls the matter inwards, while pressure from the heat and radiation from the star's core pushes outwards. The balance between the forces creates a stable state, with a constant rate of fusion reactions in the core. Pulsating stars experience disturbances, termed perturbation, disrupting their stable state that can come from a variety of factors, such as changes in chemical composition or variations in internal temperature of a star. This results in the outer layers of the star expanding and contracting, leading to a variation in the brightness of the star.

2.2.2.1 Opacity Mechanism ($\kappa\gamma$)

The $\kappa\gamma$ driving mechanism for pulsating stars deals with the behavior of partially ionized atoms and molecules in the outer layers of the star, which affects opacity and it can drive pulsations in the star (Weiss et al., 2004).

In a pulsating star, there are regions where the temperature and density change rapidly due to the star's oscillations. When the temperature drops below a certain threshold (Allen & Cox, 2000), some of the atoms in the star's outer layers become partially ionized, meaning that they lose some, but not all, of their electrons. These partially ionized atoms and molecules absorb light more effectively than their fully ionized or neutral counterparts, leading to a decrease in the star's overall opacity.

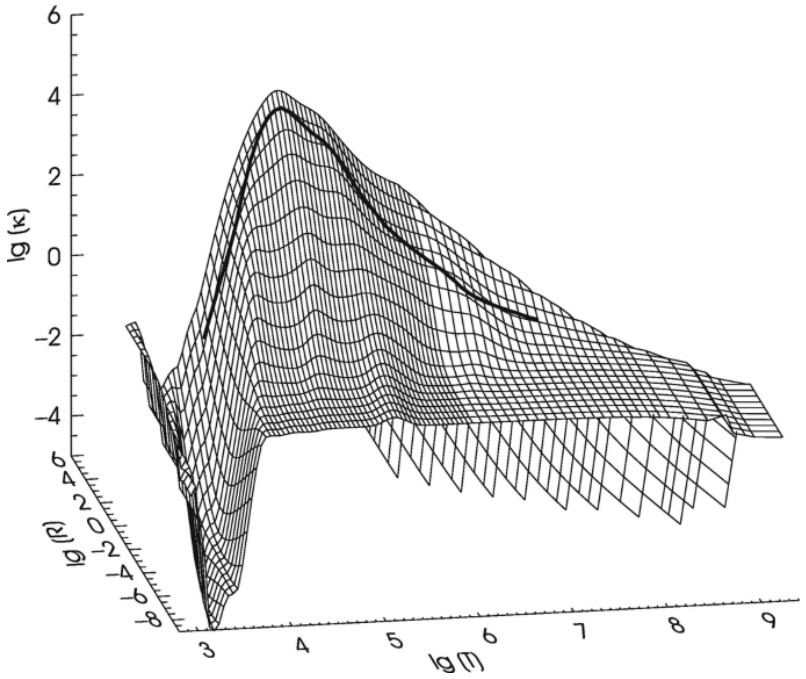


Figure 2.9: Opacity curve as a function of temperature (Kippenhahn et al., 1990).

The opacity mechanism can be described by Fig 2.9. At lower temperatures, the lack of photon energy for ionization and limited electron scattering results in low gas density and opacity. Conversely, higher temperatures lead to opacity primarily from pressure ionization and atomic collisions. Increased temperature reduces opacity as higher-energy photons are less efficiently absorbed (Tayler, 1994). It can also be described mathematically using the Kramer's law, which relates the opacity of a gas to its temperature and density. The law is expressed as:

$$\kappa = \kappa_0 \frac{\rho}{T^{\frac{3}{5}}} \tag{2.2}$$

where, κ is the opacity, κ_0 is a constant that depends on the specific properties of the gas, ρ represents the amount of gas density, and T denotes the temperature at which it exists (Baker & Kippenhahn, 1962). The exponent of $-\frac{3}{5}$ arises from the dependence of the opacity on the frequency of collisions between particles, which is proportional to $T^{-1.5}$, and the density of particles, which is proportional to ρ. When a star undergoes pulsations, the temperature and density in its outer layers change, causing the partial ionization zones to shift. As a result, the star's overall opacity also changes, affecting the balance of radiation pressure and gravity that drives the star's pulsations.

When the star collapses, a large amount of energy is used to increase ionization

within the partial ionization zone rather than heating the interior. There will be an increase in the opacity of the zone. As a result, the electromagnetic energy is successfully contained, hence increasing the pressure from outside on the zone; therefore, this mechanism describes the decrease in radiation. The expanding zone cools as it rises, in addition to generating variations in opacity and emanating pressure. Further cooling causes the ionized material to mix again. As a result, both the opacity and the external pressure suddenly drop, and the zone returns to its initial location. During a cycle, each pulsation cycle activates the partial ionization zone. In this case, a star is not fixed hence even minor fluctuations are amplified. This procedure keeps pulsations from diminishing. The κ-mechanism is the most effective explanation for the pulsations of stars (Kilkenny, 2013). The depths of the partial ionization zones have a major role in a star's pulsation characteristics and the temperature determines where they are located within the star. The areas are relatively near to the surface if a star is hotter than 7 500 K.

The mechanism is unable to start the acceleration required for pulsations because there is insufficient mass above the areas. Partial ionization zones, on the other hand, are very deep on the interiors of stars that are colder than 5 500 K. As a result, the system loses its ability to keep pulsations going. In order to determine whether or not pulsation movement occurs in stars, the position of the zone must be taken into account. The instability strip is a region located in the HR diagram associated with high density pulsating stars, and it may be that some variables have a well-defined driving zone. There are types of modes and their respective excitation mechanisms: upward and to the left of the HR diagram for opacity-driven acoustic modes, upward and to the right for opacity-driven internal gravity modes, and horizontal for stochastically excited modes (Christensen-Dalsgaard, 2004). The oscillations observed throughout on this dashed region are caused by a thermodynamic mechanism distinguishing between temperatures (warm and cool) surfaces. Cepheids, δ Scuti, RR Lyrae [2], as well as roAp stars are appropriate examples of variables which have a He II partial ionization zone and are in the warm segment of the strip, while Mira [3] stars as well as semi-regular variables are well known for H I (neutral hydrogen) and He II (singly-ionized helium) partial ionization zones situated in the cooler region of the strip, substantial and efficient convection is seen (Aerts et al., 2010)[4].

[2]RR Lyrae are A-type pulsating variable stars
[3]Mira are M-type long-period variable stars characterized by their pulsations
[4]OBAFGKM are the different spectral types of stars, see more details in section 3.2.1

2.2.2.2 The Effect of Stellar Rotation on Pulsations

According to De Ridder et al. (2022), stellar rotation can influence photometric oscillation amplitudes in two distinct ways. Firstly, it can alter the photometric visibility, which refers to how the pulsations are observed on the surface of the star. Secondly, rotation can impact the intrinsic oscillation amplitude, which represents the inherent magnitude of the oscillations. These two mechanisms highlight the multiple ways in which stellar rotation can impact the observed photometric behavior of pulsating stars.

Stellar rotation exerts a major impact on the pulsational behavior the late B-type and early A-type pulsators by altering the pulsation modes orientation and causing frequency splitting of the oscillation modes. Several studies have discovered that rotation has a considerable influence on the pulsation periods and amplitudes of late B-type stars, whereas others have discovered little or no effect. An illustrative study exploring the impact of rotation on late B-type pulsator is the research conducted by Degroote et al. (2010). They used high-quality spectroscopic and photometric data to study the pulsation properties of the B-type star HD 50230, which exhibits both radial and non-radial pulsations. They found that the non-radial modes in this star are strongly affected by rotation, with the pulsation periods and amplitudes varying significantly with rotation rate. The effect of rotation on late B-type pulsators was investigated in another study conducted by Dupret et al. (2004). A combination of theoretical modeling and observational data was employed to explore the pulsation properties of several B-type stars, including the well-known pulsator HD 129929. It was discovered that significant frequency splitting of the pulsation modes can be induced by rotation, and this phenomenon can influence the interpretation of the observed pulsation spectra.

Gravity darkening is a phenomenon present in all stars due to rotation. It causes a non-uniform temperature distribution across the star's surface, with the equator being hotter than the poles. This effect is particularly prominent in rapidly rotating stars and can impact the interpretation of pulsation patterns in pulsating stars. Rapid rotation leads to a reduction in the apparent T_{eff}, primarily caused by equatorial gravity darkening when observed equator-on. It shifts the star to cooler temperatures on the HR diagram and introducing new, relatively frequent gravito-inertial modes (Salmon et al., 2014).

2.3 GAIA HR Diagram and Maia Stars

In the Hertzsprung-Russell (HR) diagram, pulsations can be observed in different star classes and locations during different stages of stellar evolution.Gaia mission's Collaboration et al. (2018) ability to show the immense potential of integrated and homogeneously selected spectroscopic, astrometric, and photometric data to explore OBAF-type MS pulsators is the most important aspect of its project for asteroseismology is the vast array of sources for which it accumulates information.

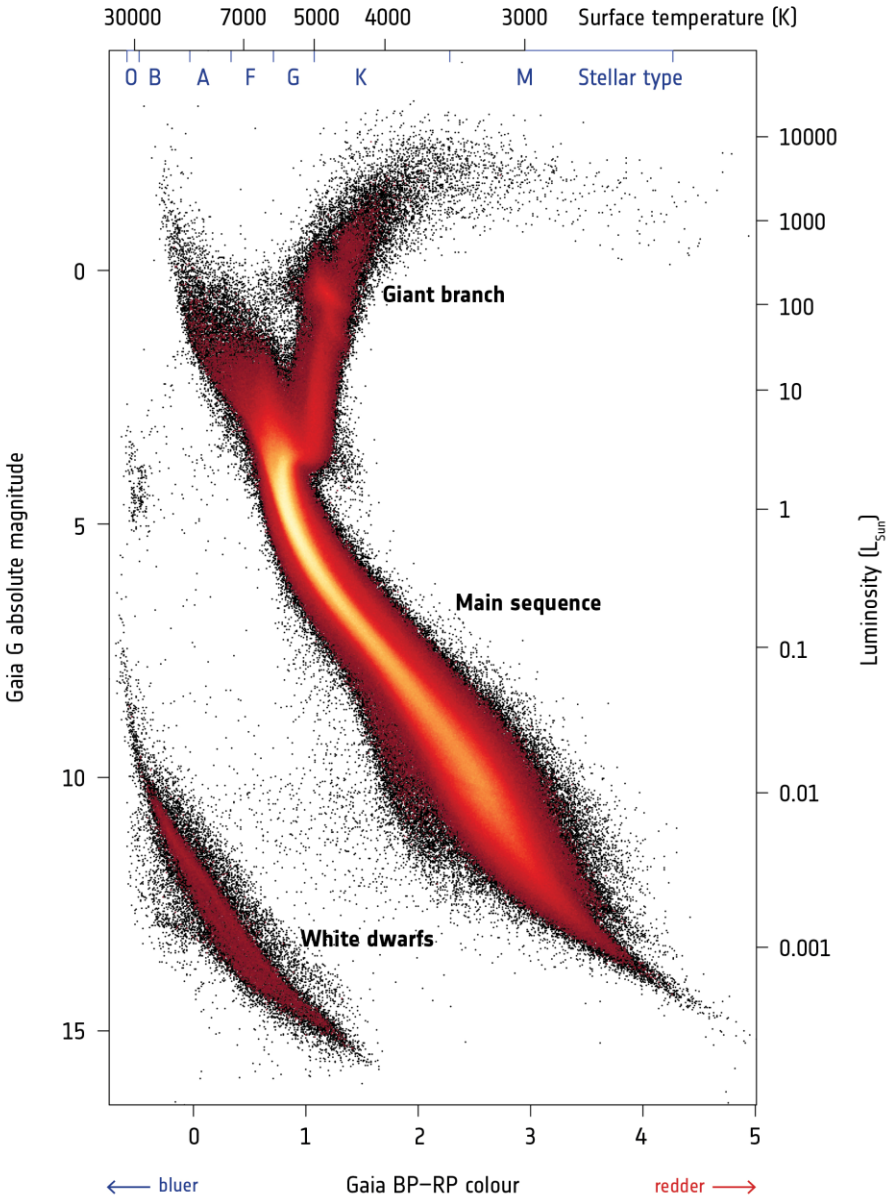


Figure 2.10: HR diagram derived from Gaia Data Release 2 observations (Collaboration et al., 2018).

The giants and supergiants, which are bright stars that have diverged from the MS region, and white dwarfs are among the principal classifications of stars found on the HR diagram. MS stars have a wide range of effective temperatures, but since they are more bright at higher temperatures, they tend to follow a band from the bottom right to the top left of Fig 2.10. The region encompasses stars ranging from the bright and hot O and B stars in the upper left corner to the cool and dim K and M stars in the bottom right corner. The MS phase constitutes the majority of a star's lifespan (Young, 2012). The Gaia DR3 atalog **?** is sufficiently acurate and precise to place OBAF-type pulsators across the HR diagram. Therefore, using Gaia photometry, the presence of Maia variables is now properly confirmed by **?**. The variability of these pulsators is still not fully understood by researchers

The Gaia mission offers a significant advantage in asteroseismology due to its extensive data collection from a large number of sources. It effectively demonstrates the potential of utilizing combined and uniformly sampled Gaia data, including photometric, spectroscopic, and astrometric information, to investigate pulsators of the OBAF-type MS.

Despite this progress, the variability of such pulsators remains inadequately understood. Previous studies (De Ridder et al., 2023; Aerts & Kolenberg, 2005; Salmon et al., 2014) observed that the frequencies of gravito-inertial modes in moderately to fast-rotating stars may readily shift within the context associated with p-modes. This phenomenon, particularly pronounced for g-modes with $|m| > 1$, m denotes the azimuthal order of a mode of oscillation, this complicates the classification of variability based solely on photometric frequencies. It highlights the propensity for misclassifications of B-type variables using photometric data alone, emphasizing the necessity for additional unbiased information, especially high-precision spectroscopy, for accurate interpretation of frequencies of these variables. Notably, the Gaia CU7 classifiers Eyer et al. (2013) do not yet include fast-rotating BAF-type pulsators as a separate variability class, based on recent Kepler-guided insights into their mode frequencies among pure p- and g- modes.

2.3.1 Evolution of Massive Stars

Massive stars are characterized by birth masses exceeding around four (4) times the Sun's mass. They have a vital influence in shaping the cosmos, from their formation to their eventual explosive deaths as supernovae (Kippenhahn et al., 1990; Maeder & Meynet, 2000; Maeder, 2008; Langer, 2012) with the gamma-ray bursts and the

progenitors of core-collapse (Heger et al., 2003; Tanvir et al., 2009; Smartt, 2009; Modjaz et al., 2019). Understanding how massive stars collapse depends on mapping supernovaes with respect to their progenitors. Recent studies (Meynet et al., 2013) have investigated the red supergiant problem, which refers to the difficulty in identifying the Type II-P supernovae progenitors. The exact conditions that leads to various types of gamma-ray bursts and supernovae are still not fully understood, but recent studies have made progress in identifying the progenitors of some types of supernovae.

Cold and dense molecular clouds form massive stars. Studies have shown that the high mass stars formation is a complex process that may be bimodal and does not necessarily lead to a ZAMS star. The phenomenon can be attributed to the H fusion in the core through the CNO (nuclear fusion reactions that convert H into He to release energy to maintain luminosity) whilst maintaining hydrostatic equilibrium (Langer, 2022). The formation process is influenced by factors such as turbulence, magnetic fields, and radiation feedback from nearby stars. Massive stars exhibit radiative envelopes and convective cores during the MS phase of their evolution, resulting in comparatively shorter MS lifetimes (Georgy et al., 2014; Gabriel et al., 2014; Paxton et al., 2018, 2019) and convective-boundry mixing as implemented numerically and convection and are important in determining their evolution as well as core masses. The amount of H available for nuclear burning is directly impacted by the mixing profile at both the radiative and convective regions interface and in the envelope (Miglio et al., 2008; Pedersen et al., 2018; Michielsen et al., 2019).

Rotation has a significant impact on the evolution path of massive stars. It induces mixing within the stellar interiors (Maeder & Meynet, 2000), which affects the theoretical models used to describe their evolution. However, these models rely on assumptions about mixing profiles that are yet to be empirically calibrated, see e.g. (Aerts, 2021; Serenelli et al., 2021) for detailed reviews). This introduces uncertainties in mass and age estimations. The interaction of metallicity levels, mass loss and rotation rates due to stellar winds further complicates the evolutionary modeling of high-mass stars. Nonetheless, the current models for mixing profiles in high-mass stars rely on assumed prescriptions and are controlled by multiple free parameters that lack empirical calibration. When determining the ages as well as masses of massive stars the sources of errors are significantly introduced in their models of theoretical evolution. The lack of empirical calibration for mixing profiles hinders our ability to accurately predict the evolution of these stars (Bowman, 2020).

Massive star's behaviour and evolution can be affected by magnetic field. It is es-

timated that a large-scale magnetic field with polar field strengths ranging from around 100 Gauss (G) to a couple kG exists in about 10% of high mass stars. Evolutionary models get more complicated when magnetic fields are present in high mass stars (Eldridge & Stanway, 2022). Studies have shown that magnetic fields could have an impact on the winds as well as the nebulae of massive stars. Intense radiation fields and line-driven winds in massive stars are driven by the high luminosity's of these stars (Langer, 2012). Radiation pressure on spectral lines on the surface of the star causes these winds. Mechanisms behind these winds are still not fully understood.

The evolutionary track of massive stars on the HR diagram is determined by their properties, alongside factors like metallicity and opacity, collectively shaping their thermal structure. Recent studies have delved into the interior structures of massive stars, emphasizing the presence of convective cores and radiative envelopes (Bowman, 2020). The κ-mechanism, a key driver of pulsations in high-mass stars, has been a subject of recent investigation. The physics of massive stars is still unresolved, despite their importance in the cosmos, and there are still many unanswered questions over all evolutionary stages (Eldridge & Stanway, 2022). The analysis by Mahy et al. (2020) emphasized the necessity to refine physical descriptions and parameters of massive stars by utilizing stringent observational limitations on the interiors of stars.

Furthermore, the interplay of diverse rotation rates, distinct metallicity ranges, and the evolutionary models of massive stars exhibit complex degeneracies due to the impact of mass loss by stellar winds. Consequences of binarity and mass transfer further compound theoretical uncertainties. Therefore, the presence of massive stars within multiple systems has been recognized as a significant factor in investigating and alleviating uncertainties related to model parameter uncertainties (Bowman, 2020).

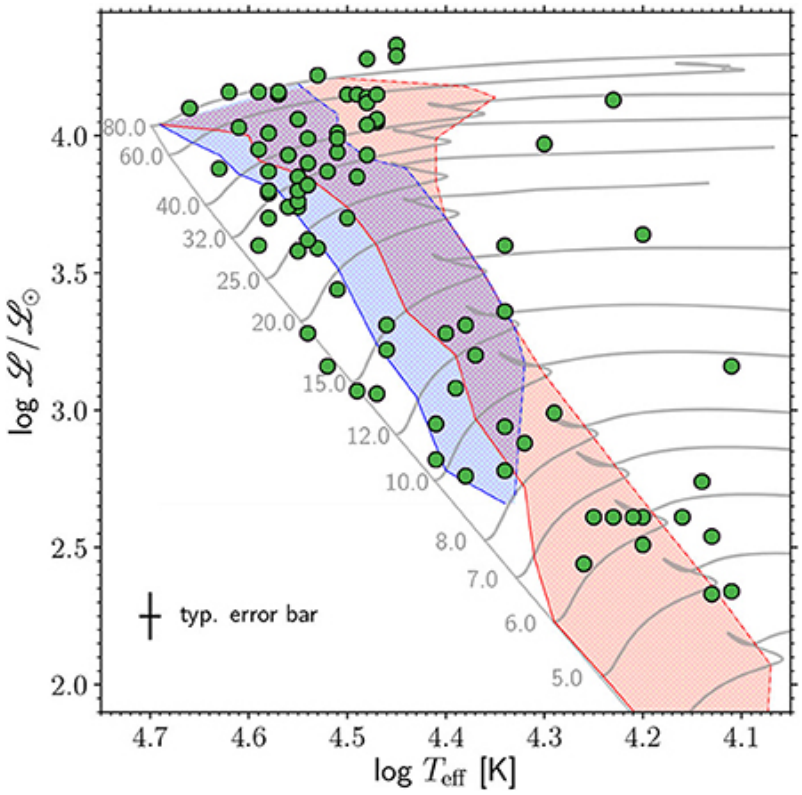


Figure 2.11: Spectroscopic evolution of massive pulsating stars in the HR diagram by *TESS* (sectors 1–13) adopted from Burssens et al. (2020).

Fig 2.11 is a representation of how massive stars evolve. The green circles show the spectroscopic data obtained using high resolution spectroscopy as indicated in the diagram which illustrates the spectroscopic evolution of massive pulsating stars in the HR diagram by *TESS* (sectors 1–13). *TESS* divides the sky into sectors for observation, each sector covers a specific area of the sky. The red and blue hatched sections represent the g- and p- modes in the theoretical instability regions, respectively, for MS stars. The solid gray lines indicates the non-rotating evolutionary tracks of stars at different masses ($M_\odot$), and the bottom-left corner shows a typical spectroscopic error bar (Burssens et al., 2020).

2.3.2 B-type stars

Habets & Heintze (1981) explain that B-type MS stars are those that have spectral type band luminosity class V with surface temperatures of about 10,000 to 30,000 K, such stars have masses that are 2 to 16 times greater than the Sun's. A B-type MS star (color index B-V) is a H-burning star of spectral type B which are extremely luminous and blue.

The cause of the fluctuations in light might be due to stellar pulsations, variations in the star's disk, rotation, or binarity. In the early 1900s, B-type stars were discovered to have spectroscopic and photometric variability (Guthnick, 1913; Frost, 1902), which was connected to radial and non-radial pulsations (Ledoux, 1951). It is stated that these pulsations are triggered by the localized increase in opacity imposed on by Iron (Fe) group components (so-called Z-bump) (Moskalik & Dziembowski, 1992). Various B-type stars have been studied over the years (Handler, 2012), and findings suggest that some of these stars pulsate in low-overtone p- and g-modes, some in high-overtone g-modes, and others actually exhibit both types of pulsations. Unfortunately, there is still much to learn about several aspects of their development; particularly, element mixing processes and the transfer of angular momentum. With an emphasis on unanswered questions, the extent to which we now understand the variety of B-star pulsation is questioned. There are a few B-type stars in the stellar classes B0-B3 that have particularly strong non-ionized He lines. These He-strong stars are chemically peculiar and hence named Be because of their strong magnetic fields in their photosphere. There are, however, He-weak B-type stars with strong H spectra and faint He lines. of spectral categories. For spectral types B7 to B9, there are unusual chemical compositions, HgMn rich stars. These Be stars have a significant H emission spectrum.

2.3.2.1 SPB Stars (Slowly Pulsating B-type Stars)

SPB stars are considered to be mid-type to late B-type pulsating variables that have periods ranging from 0.5 to 4 days (12 to 96 hours). The multi-periodic variations observed in SPB stars can only be attributed to pulsations (Waelkens, 1996). The fact that their periods of time are significantly longer than those expected for fundamental modes means that they must pulsate in non-radial g-modes in particular (Baldry, 1999). The star 53 Persei was used as a prototype for searching for and analyzing variability in hot blue stars, leading to the discovery of SPB (Waelkens & Rufener, 1985). Later, they located these stars in the MS region with spectral classifications ranging from mid to late B-type stars and periods of days per cycle $(0.5-3)d$ (Waelkens, 1991). The majority of stars with frequencies below 2.5 d^{-1} are categorized in this region. According to data taken from the work by Glebocki & Gnacinski (2005), the average rotational velocity ($v \sin i$) for B5–B9 MS stars with the normal spectral type range of SPB variables is $v \sin i = 144$ km s^{-1}. They are located slightly below the β Cephei stars in the HR diagram, which means they are less massive $(3-9)M_{\odot}$, multiperiodic high-order low-degree g-mode pulsators

(Hubrig et al., 2006). Using *TESS* photometry, Sharma et al. (2022) confirmed the extension of pulsations into cooler temperatures extending into the early A-type stars. The hypothesis is that these instances might be indicative of rapidly rotating SPB stars.

2.3.2.2 β Cephei Stars

For over a century, β Cephei variables have been a popular topic among the pulsating variable stars. To date, there have been numerous studies conducted to comprehend the variability in the well-known instability strip in the HR diagram. The class of β Cephei stars was initially described by Lesh & Aizenman (1978), saying that *"These stars share the very same short period for their brightness variation and radial velocity variation"*. β Cephei stars have about the $3-8$ hours of the pulsating period with low-order gravity (g)- and/or pressure (p)- modes. They exhibit multiple periodicity in the V band with amplitudes < 0.3 magnitudes. Their pulsations are characterized by both radial and non-radial modes, such as fundamental and low-overtone p- and g- modes, are likely to be unstable within the β Cephei classification (Moskalik, 1995). β Cephei stars are located along the MS and have spectral types O9 to B3 (Hubrig et al., 2006). According to a catalogue by Glebocki & Gnacinski (2005), the average projected rotational velocity ($v \sin i$) for O9-B3 MS stars which is the usual spectral type range of β Cephei variables is $v \sin i = 140$ km s^{-1}.

2.3.3 A-Type Stars

The surface temperature of A-type stars range from 7 600 to 10 000 K, and their masses are between 1.4 and 2.1 $M_{\odot}$. Strong H Balmer absorption lines in the spectra of these stars serve as their spectral signals. Section 2.3.3.1 explains the δ Scuti class of the early A-type pulsating stars that seem to merge well with the hypothesized Maia region and these stars may help or actually be providing definite challenges to our current stellar pulsation knowledge.

2.3.3.1 δ Scuti Stars

MS and sub-giant stars, primarily of spectral classes A and early F-type, constitute the majority of δ Scuti stars, exhibiting pulsations with amplitudes below 0.8 magnitudes. These stars display both radial and non-radial p- and g-modes, akin

to β Cephei stars. Stars with amplitudes exceeding 0.2 magnitudes are classified as High Amplitude Delta Scuti Stars (HADS). Observations from the *Kepler* satellite confirm low frequencies in all δ Scuti stars, undetectable by ground-based observations (Balona, 2014). Despite models suggesting instability, only for frequencies greater than 5 d^{-1}, precise examinations reveal unexplained low frequencies in all Scuti stars (Balona et al., 2015a). The region overlapping the blue edge of the γ Dor instability strip exhibits the highest amplitudes of low-frequency frequencies. γ Dor/δ Scuti hybrids, showcasing both high and low frequencies, are predominantly observed from the ground in this region of the HR diagram. The high-frequency pulsations in δ Scuti stars are attributed to the kappa (κ) and gamma (γ) mechanism in the He II ionization zone (Pamyatnykh, 2003). Pulsations in δ Scuti stars are believed to result from a combination of the star's rotation and internal structure, generating waves of pressure as the star rotates.

2.4 Maia-type stars

2.4.1 Existence of the presumed Maia stars

In 1955, Struve (1955) proposed the name 'Maia' for a group of variable stars ranging from the late B-type (B7III) to early A-type (A3II) stars. Later, it was discovered that Maia was neither a photometric variable (changes in its brightness) or radial velocity variations (spectroscopic variability), indicating that the strength of the star's He line fluctuated irregularly. In addition, the peculiar behavior of Maia was shown to be a fluctuating He line strength, which was thought to be nonperiodic. Moreover, there is no photometric proof to support Maia variability (Struve et al., 1957). Three decades later, an astronomer (McNamara, 1985) conducted another investigation to assess the photometric fluctuation of four stars in the 'Maia instability strip'. The main objective was to investigate the Maia class reality as variable, assuming that the class exists. To determine the pulsation characteristics of the stars and how they fit into the general conception of the upper MS. McNamara's results show spectrum features as well as the anticipated type of pulsation, indicating that the Maia phenomenon may just be an extension of the 53 Persei stars' cooler temperatures. There were several unsuccessful attempts to find short-term periodic variability in stars located between the β Cep and δ Scuti instability strips. The B9p star 'ET And' [5] was the most frequently cited example of a '*Maia pulsator*' in

[5]The B9p star ET And, also known as HD 13974, is a chemically peculiar B-type star located in the constellation Andromeda. The "p" in its spectral classification indicates that it exhibits

the late 1900s, with a photometric period of roughly 0.1 d^{-1}, which was a good bet (Panov, 1978).

Over the years, ground-based measurements have suggested the existence of a few questionable stars with high frequencies that are too hot to be δ Scuti but too cool to be β Cephei (McNamara, 1985; Lehmann et al., 1995; Percy & Wilson, 2000). Observations conducted on the *CoRoT* mission revealed the existence of an exclusive low-amplitude B-type pulsator class situated between the SPB and δ Scuti instability strips as a result of investigating the detected B-type variables with a wide frequency range reaching far into the β Cephei range (Degroote et al., 2009). During their survey of our part of the Milky Way galaxy to identify hundreds of Earth-size and smaller planets located within or in proximity to the habitable zone, *Kepler* space telescope found this hypothesized group of 'Maia' class (Balona et al., 2015a, 2016; Mowlavi et al., 2013; Lata et al., 2014) identified an unusual high frequencies in fast rotating late to mid-B stars using ground-based photometry. It was uncertain whether these stars were Maia variables or if there was an explanation for their pulsation parameters that were not understood. Salmon et al. (2014) discovered that a 10-day period may be observed in mid-to late B stars using pulsating models of rotating B stars. It was speculated that these may be fast-rotating SPB stars with gravity darkening near the equator, which decreases the apparent effective temperature.

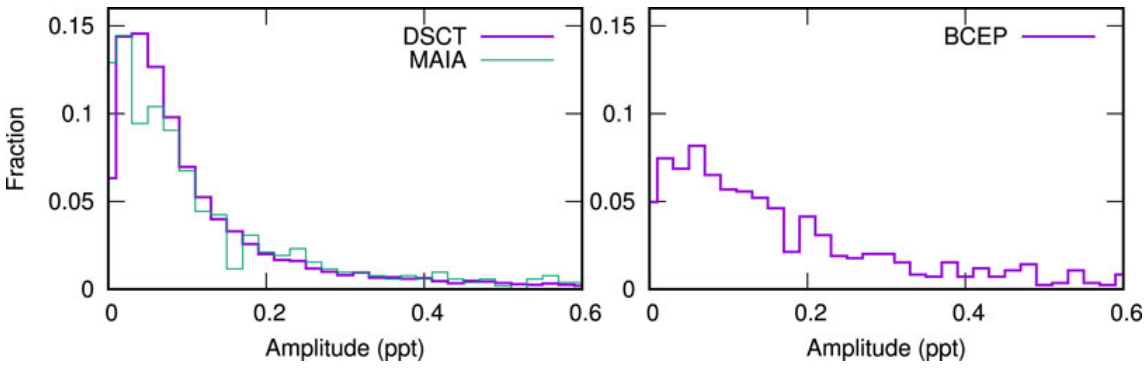


Figure 2.12: The amplitude distribution in δ Scuti and Maia star (Balona, 2023a).

Research findings indicate that it is challenging to distinguish the T_{eff} observed among δ Scuti and Maia variables, or between β Cephei and Maia stars among early-type stars. This lack of separation is supported by previous research in Fig 2.12 from a study by Balona (2023a), showing an amplitude distribution in δ Sct and Maia stars (left figure) and in β Cep stars (right figure), measured in ppt. The group

peculiarities in its spectrum, particularly in its chemical composition

of SPB stars, starting from B0 and extending to A0 (spectral types), integrates with the group of γ Dor stars, which spans the cooler end of the δ Scuti instability strip. The results suggest that there is significant overlap and no clear boundaries among the different variability groups in early-type stars.

Using the *TESS* satellite data, Balona & Ozuyar (2020) confirmed 131 potential Maia stars. Over the past few years, Hambly et al. (2022) also discovered a population of Maia stars through Gaia photometry. Balona & Ozuyar (2020) interpreted the existence of high frequencies in these stars due to rapid rotation in SPB stars.

Based on the analysis of the *TESS* data, Balona & Ozuyar (2020) concluded that stars that actually pulsate at frequencies higher than approximately 5 d^{-1} are familiar among B stars, for both late B- and early A- type stars. Surprisingly, they did not observe distinct regions of instability as predicted by theoretical models. Instead, they observed a smooth transition between the β Cephei variables, Maia stars, and δ Scuti stars. Similar smooth transitions were observed among the low-frequency pulsators. The SPB stars, which are found throughout the B-type MS, extend into the A star region and connect with the hot γ Dor variables.

2.4.2 Pulsations in Maia stars: Justifications

Asteroseismology is a useful technique for examining the pulsations of Maia stars as it offers insights about the interior of a star by probing beneath its surface. The purpose of asteroseismology is to measure the speed of sound across the star to identify the basic parameters of the star's structure as explained in details above.

2.4.2.1 Pulsation mechanism

A B-type star normally have deep absorption lines in its spectrum from the H Balmer lines. Be-type stars exhibit emission or partial emission in several Balmer lines, with the Hα and Hβ lines exhibiting the highest emission. The emission is caused by a gaseous disc that surrounds the star. The disc is produced by eruptions that occur occasionally. The eruptions have not been recognized as a cause. The eruptions are believed to be caused by stellar activity, according to another theory (Hernández et al., 2013). As for other classes of pulsating stars, the well-known mechanisms for stars like the SPB stars is the metal opacity bump and as for the δ Scuti stars they are driven by the He II bump. Kallinger et al. (2002) mentioned that there is no

known anormal opacity (unusual behavior in the absorption or scattering of light within the stellar atmosphere) explanation that may be causing pulsations in the presumed Maia area region. Rivinius (2013) had the most prevalent theory that the stars are on the verge of catastrophic rotation and that the mass loss is somehow caused by pulsations.

Prior to the Salmon et al. (2014) of observing more than 5 d^{-1} period in the late B-type stars, they presumed that these may just be rapidly rotating SPB stars with gravitational darkening at their equator decreasing their apparent effective temperature. Based on the physical observation that β Cepheids pulsates mostly in p-modes of low radial order and the SPB in g-modes of high radial order, the division between β Cephei and SPB stars appears justified. This suggests that they have different pulsational driving mechanisms function in different regions at different thermal timescales. In a previous study, there was also a hypothesis that these peculiar pulsating stars could be binary systems with a primary B star and a secondary δ Scuti variable. However, the substantial quantity of these unusual variables and the latest observations from both *CoRoT* and ground-based sources disagree with the proposed theory. Given that these stars cannot be classified as β Cephei or SPB stars, and their temperatures are too high to be classified as δ Scuti variables (Balona et al., 2011).

The significant finding by Balona (2019) is the widespread presence of starspots across the MS, which suggests the existence of surface convection in A and B stars. The inclusion of convection in theoretical models could potentially help to address the issues observed in these stars. However, it is important to note that convection might not be the sole factor contributing to the observed phenomena. Thus, considering convection in modelling can be advantageous, but other factors should be taken into account to fully understand observed behaviors.

No model can reproduce Maia variables successfully, or at least a few of the SPB/γ Dor stars that are located at the intersection of the cool edge of SPB variables with the hot edge of γ Dor stars. Two noteworthy observations challenge existing models: firstly, the presence of a considerable number of δ Scuti stars hotter than the predicted hot edge, extending well past T_{eff} = 10 000 K, where they converge with Maia variables; and secondly, the systematic decrease in ν_1 (frequency of the highest amplitude) observed in hot δ Scuti stars, establishes an additional connection between δ Scuti and Maia stars. This suggests a potential link between δ Scuti and Maia stars (Balona, 2023b).

2.4.2.2 Rotation

Gravity darkening can occur in any star, whether it is pulsating or not. In the light of this, there is no bias when contrasting the rotational velocities of Maia stars and MS stars in the same T_{eff} range. The presence of pulsations with periods comparable to that of β Cephei stars has been seen sometimes in late-B stars. These are the presumed 'Maia variables' (Balona et al., 2015b; Mowlavi et al., 2016; Balona & Ozuyar, 2020), in the late B-type variables despite the fact that the star Maia which is a 20 Tau/HD 23408, the alleged prototype of this class, is actually caused by chemical spots with no pulsations and also a mercury-manganese (HgMn) star with rotational modulation (White et al., 2017). For instance, there is a possibility of confusing a rapidly rotating β Cephei star for a Maia variable. In addition, gravito-inertial modes with frequencies that are greater than usual may exist in moderate to rapid rotators. It follows that fast rotating SPB star may likewise be misinterpreted for a 'Maia' star. Salmon et al. (2014) examined the suggested impacts concluding that their models can replicate the (Mowlavi et al., 2013, 2016) findings. Using pulsation models of fast-rotating MS B-type stars, (Saio et al., 2017) computed the properties of prograde sectoral g and retrograde r-modes driven by the κ mechanism centred on the Fe opacity peak. Concluding that the Period Luminosity (P-L) relation is described by prograde sectoral g-modes of rapidly rotating stars as explained by Mowlavi et al. (2016).

Therefore, Maia stars do not exhibit the characteristics of rapidly rotating SPB stars. Maia and SPB variables both have rotational velocities that are similar to those of typical MS stars (Balona, 2023a).

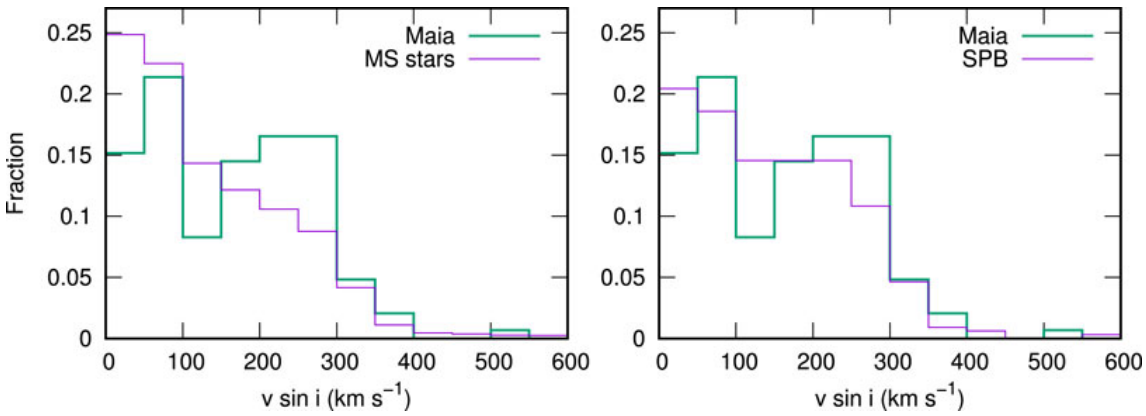


Figure 2.13: The distribution of $v \sin i$ for Maia variables among MS stars and Maia/SPB stars in the same temperature range (Balona, 2023a).

The distribution of $v \sin i$ for Maia variables among 6538 MS, 145 Maia and 323

SPB stars in the same temperature range ($10000 < T_{eff} < 18000$) is presented in Fig 2.13.

2.5 Asteroseismological studies of B-type stars

Before the Kepler mission's launch, it was widely accepted that in main-sequence B stars, the κ mechanism in the iron-group ionization zone accounted for the high-frequency pulsations observed in β Cephei stars and the low-frequency pulsations in cooler SPB variables. At the cooler end of the δ Scuti instability strip, γ Dor variables were thought to experience pulsations driven by the convective blocking mechanism Guzik et al. (2000). However, a major breakthrough came with the discovery that low-frequency γ Dor pulsations extend throughout the δ Scuti instability strip Grigahcène et al. (2010). This finding indicated that the difference between δ Scuti and γ Dor variables is more about mode selection rather than distinct pulsation mechanisms, as both types share the same instability region Balona (2018). This realization has raised questions about the assumptions related to convection in the upper main sequence.

The range of pulsating stars extends from β Cephei stars (spectral types B0–B3), which exhibit low-order pressure (p) and gravity (g) modes with frequencies greater than approximately 3.5 d^{-1}, to SPB stars (spectral types B3–B9), showing high-order g-mode oscillations with frequencies less than about 3.5 d^{-1} (**?**Aerts et al., 2010). δ Scuti stars (spectral types A2 to F5) exhibit high frequencies (greater than 5 d^{-1}), similar to β Cephei stars (Chang et al., 2013; Uytterhoeven et al., 2011). RoAp stars, which are chemically peculiar due to strong magnetic fields, show high-order pressure modes with frequencies exceeding 50 d^{-1} (Holdsworth et al., 2024). γ Dor stars (spectral types F2–F6) have low-frequency (less than 5 d^{-1}) g-mode pulsations (Uytterhoeven et al., 2011), while solar-like oscillators, with even later spectral types on the main sequence, display stochastic high-order p-mode oscillations with frequencies around 300 d^{-1} (Jackiewicz, 2021).

Our understanding of pulsations in these stars has evolved significantly over the past decade. For example, in roAp stars with strong global magnetic fields, (Balmforth et al., 2001) proposed that high-frequency pulsations are driven by the κ mechanism in the H/HeI partial ionization zone. Although these pulsations are stable in models, convection suppression at the magnetic poles causes instability, which explains the alignment of the pulsation and magnetic axes. Before the advent of photometric space observations, it was thought that a complete picture had been established:

stars with radiative envelopes were predicted to exhibit multiple p-mode pulsations driven by the κ mechanism, with unstable pulsation frequencies exceeding 5 d^{-1}, corresponding to δ Scuti stars. In cooler stars where convection becomes important, instability was attributed to the convective blocking mechanism, with frequencies less than about 5 d^{-1}, corresponding to γ Dor stars. The few known δ Scuti/γ Dor hybrids were satisfactorily explained by more advanced convection models (Dupret et al., 2005).

Despite the broad spectrum of pulsating stars, there remains a notable gap between spectral types B9 and A2. This gap exists because pulsations in B-type stars are driven by the κ mechanism in the iron-group ionization zone (Dziembowski et al., 1993), while δ Scuti stars experience pulsations driven by both the κ mechanism and/or turbulent mechanisms in the partial ionization zones of helium (Baker & Kippenhahn, 1962; Antoci et al., 2014) and hydrogen (Cunha et al., 2013). No known pulsation mechanisms fully account for observed pulsations in stars with spectral types between late B and early A, particularly those with intrinsic frequencies exceeding 3 d^{-1}. Despite these predictions, numerous B-type stars have been observed to pulsate outside the expected instability strips. For example, some stars hotter or cooler than the predicted boundaries of these strips exhibit pulsations that challenge existing models. These anomalies have prompted the development of several hypotheses to explain the underlying mechanisms responsible for these unexpected pulsations.

2.6 Hypotheses for Anomalous Pulsations

2.6.1 Rapid Rotation Hypothesis

One of the primary hypotheses proposed to explain the anomalous pulsations in B-type stars is the rapid rotation hypothesis (Aliçavuş et al., 2024). This hypothesis suggests that rapid stellar rotation can lead to significant deviations from spherical symmetry, causing gravity darkening—a phenomenon where the equatorial regions of a star become cooler than the poles. This temperature variation could potentially allow pulsations that would not normally occur in a non-rotating star. However, this hypothesis is not without challenges, as not all rapidly rotating B-type stars exhibit the expected pulsation characteristics, and some pulsators rotate at moderate speeds.

2.6.2 Binary Hypothesis

Another explanation involves the binary nature of some B-type stars (Aliçavuş et al., 2024). In this scenario, a pulsating star could be part of a binary system, where the observed pulsations are influenced by a companion star. For instance, a δ Scuti pulsator could be part of a binary system with a hotter B-type star, leading to the appearance of pulsations in regions of the H-R diagram where they would not typically be expected. This hypothesis is supported by the fact that many B-type stars are found in binary systems, though it does not account for all observed cases of anomalous pulsations.

2.6.3 Observational Uncertainties Hypothesis

The observational uncertainties hypothesis suggests that errors in determining stellar parameters, particularly effective temperature, could lead to the misclassification of stars (Aliçavuş et al., 2024). If the true $T_{\rm eff}$ of a B-type star differs significantly from the observed value, it might appear to be outside the expected instability strips, when in reality, it is not. This hypothesis highlights the importance of accurate spectroscopic data in asteroseismology and the need to carefully consider potential sources of error in observational data.

2.7 Challenges to Current Models

The discovery of pulsating B-type stars outside traditional instability strips highlights the limitations of existing asteroseismological models. One of the primary challenges is the inadequacy of current pulsation mechanisms to account for the full range of observed phenomena. The traditional κ mechanism, while effective in explaining pulsations in the β Cephei and SPB stars, does not account for the anomalous pulsations observed in stars like HD 42477 and the Maia variables. The star HD 42477, classified as an A0Vnne star, presents a notable case of p-mode pulsations occurring outside the traditionally expected regions of the H-R diagram. Kurtz et al. (2023) conducted an in-depth analysis of this star, ruling out several hypotheses, including temperature uncertainties, binary influence, and contamination by background pulsators. They concluded that the observed p-mode pulsations might be explained by coupling between p and g modes or by the classical κ-γ mechanism operating in the HeII ionization zone, a finding that challenges the conventional un-

derstanding of stellar pulsations. Maia variables, a class of stars initially thought to exhibit anomalous pulsations, have also been the subject of intense scrutiny. Some studies (Salmon et al., 2014) have suggested that these stars could be rapidly rotating SPB stars. However, subsequent observations revealed that Maia stars do not have significantly higher rotation rates than non-pulsating B-type stars. This finding raises questions about the validity of the rapid rotation hypothesis for Maia variables and suggests that other mechanisms may be at play.

Additionally, the presence of multiple driving mechanisms within a single star complicates the interpretation of pulsations. For example, the interaction between the κ mechanism and turbulent mechanisms in different layers of a star may result in complex oscillation patterns that are not adequately captured by current models. This suggests that a more comprehensive approach, integrating multiple driving mechanisms and considering the effects of factors such as surface convection and starspots, may be necessary to fully understand the pulsations of B-type stars.

Chapter 3

Spectroscopy and Photometry

3.1 Introduction

In this study, a comprehensive study is utilized to investigate and characterize the selected target TIC 202431888. The observational data are obtained from a combination of high-resolution spectroscopic ground-based observations and space-based mission for precise photometry. Various observational and analytical techniques are integrated to derive fundamental stellar atmospheric parameters, providing a comprehensive approach to asteroseismic studies. A detailed discussion of each step is provided in the sections that follow, outlining the procedures and tools used for data acquisition, analysis, and interpretation. The utilization of high-resolution spectroscopy measurements complements the photometric time-series analysis, contributing towards a more thorough understanding of the target's properties.

3.2 Spectroscopy

Spectroscopy, a foundational technique in astrophysical research, enables the examination of light emitted or absorbed by celestial objects to gain crucial insights into their physical properties and behaviour. This section provides an in-depth exploration of spectroscopy, beginning with spectral classification based on the Balmer series lines, followed by a comprehensive discussion of key stellar parameters, and concluding with the significance of spectral graphs and the instruments used for high resolution spectroscopy.

3.2.1 Spectral Classification

The Morgan-Keenan (MK) system (Morgan & Keenan, 1973) is a fundamental technique used in astronomy to categorise and understand stars based on their spectral features. The MK system as shown on Fig 3.1 is built upon the analysis of spectral lines that originate from electron transitions between different energy levels within

atoms and ions.

Spectral Class	Effective Temperature (K)	Colour	H Balmer Features	Other Features	M/M_{Sun}	R/R_{Sun}	L/L_{Sun}	Main Sequence Lifespan
O	28,000 - 50,000	Blue	weak	ionised He^+ lines, strong UV continuum	20 - 60	9 - 15	90,000 - 800,000	1 - 10 Myr
B	10,000 - 28,000	Blue-white	medium	neutral He lines	3 - 18	3.0 - 8.4	95 - 52,000	11 - 400 Myr
A	7,500 - 10,000	White	strong	strong H lines, ionised metal lines	2.0 - 3.0	1.7 - 2.7	8 -55	400 Myr - 3 Gyr
F	6,000 - 7,500	White-yellow	medium	weak ionised Ca^+	1.1 - 1.6	1.2 - 1.6	2.0 - 6.5	3 - 7 Gyr
G	4,900 - 6,000	Yellow	weak	ionised Ca^+, metal lines	0.85 - 1.1	0.85 - 1.1	0.66 - 1.5	7 - 15 Gyr
K	3,500 - 4,900	Orange	very weak	Ca^+, Fe, strong molecules, CH, CN	0.65 - 0.85	0.65 - 0.85	0.10 - 0.42	17 Gyr
M	2,000 - 3,500	Red	very weak	molecular lines, eg TiO, neutral metals	0.08 - 0.05	0.17 - 0.63	0.001 - 0.08	56 Gyr

Figure 3.1: The Morgan-Keenan Spectral Types summary (Bruce MacEvoy, 2013).

A star's spectrum contains spectral lines that result from the absorption or emission of light during electron transitions within atoms. These lines are specific to each element and ion, and collectively form a distinctive pattern, that serves as a stellar fingerprint. Interpreting spectral lines involves understanding both the atomic processes and the physical conditions within the stellar atmosphere to discern the lines resulting from electron transitions. This process occurs when electrons absorb or release photons with energies equal to the difference between their initial and final energy states. A photon's energy is determined by:

$$E = \frac{hc}{\lambda}. \tag{3.1}$$

The photon's energy as denoted by E, the photon's wavelength is λ, the Planck constant, $P = 6.62607015 \times 10^{-34}$ J·s), and the speed of light is $c = 299,792,458 m/s$. The wavelengths of the spectral lines are directly related to these energy differences and can be expressed using the Rydberg formula:

$$\frac{1}{\lambda} = R\left(\frac{1}{{n_1}^2} - \frac{1}{{n_2}^2}\right) \tag{3.2}$$

Where:

- λ represents the spectral line's wavelength
- R, the Rydbergs constant ($\approx 1.097 \times 10^7\,\mathrm{m}^{-1}$)
- n_2 and n_1 represents integers of energy states

The discernment of these lines and their precise wavelengths provides information about the elements and ions present in the star's outer layers. In the MK classification, the strength and presence of certain lines, especially those of H (e.g, Balmer lines), are used to determine a star's spectral type. The classifications are hot (O as the hottest) and M as the coolest. Recent discoveries (Kirkpatrick, 2005) have prompted the exploration of potentially revised classifications that are cooler than M, called L-class stars.

3.2.1.1 Types of Spectra

The spectral lines indicated in a spectrum can be either absorption or emission lines, depending on whether the energy transitions are from lower to higher or higher to lower energy levels, respectively. These lines appear as discrete features in a continuous spectrum, which is a distribution of light over a range of wavelengths (Ball, 2001; Robinson, 2007; Kaler, 2011; Pavia et al., 2014) as illustrated by Fig 3.2.

1. Continuous spectrum. A continuous spectrum can be characterized as a distribution of colours or wavelengths without distinct lines, which is commonly observed in astrophysical phenomena. This type of spectrum is typically generated when matter, such as solids, liquids, or dense gases, emits radiation across a broad range of wavelengths. The emitted radiation encompasses a wide variety of colours, creating a seamless band of colours resembling a rainbow.

2. Absorption spectrum. The absorption lines are observed when a cooler gas located between a celestial source, such as a star, absorbs specific wavelengths of light. These lines manifest as characteristic dips or dark gaps within the spectrum. The presence of absorption lines is due to the interaction between the light emitted by the source and the cooler intervening gas.

3. Emission spectrum. The emission lines occur when electrons within atoms undergo transitions to lower energy levels, emitting photons with precise energies. These emissions appear as distinct peaks of brightness within the spectrum. The emission lines are produced when electrons absorb energy and move to high energy states, and then transition back to lower energy states, releasing photons of specific energies.

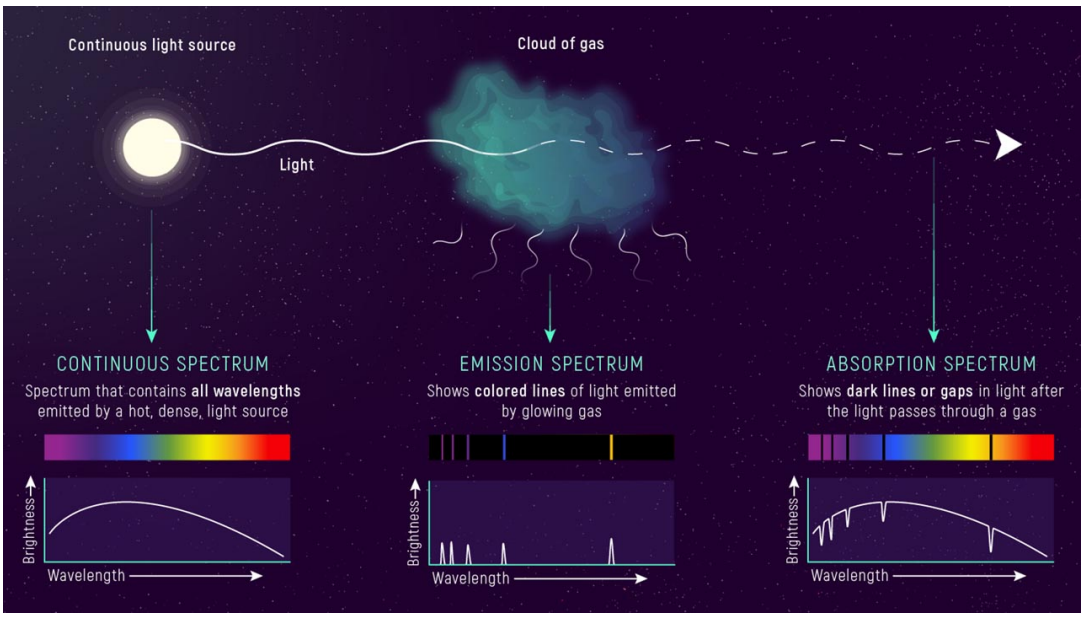


Figure 3.2: From left to right:Continuous Spectrum, Emission Spectrum, and Absorption Spectrum (NASA, 2021).

Fig 3.2 shows an illustration of the interrelation between the continuous spectrum of a star emitting light onto gas, an emission spectrum of luminescent gas, and an absorption spectrum for that particular gas. The diagram is divided into two segments. The upper half showcases a light wave emitted from a source passing through a gas cloud before emerging. The lower half showcases the three spectrum types in both visual and graphical formats.

3.2.1.2 Balmer Series

The visible part of the Electromagnetic (EM) spectrum contains a series of spectral lines known as the Balmer series indicated in Fig 3.3 that originates from electron transitions within H atoms. Johann Balmer was the first person to describe the empirical formula (Balmer, 1897) to calculate the wavelengths of the Balmer series; hence the series was named after him. The Balmer series lines are in the visible part of the EM spectrum and are denoted by the letters Hα, Hβ, Hγ, and so on, with Hα being the line with the longest wavelength.

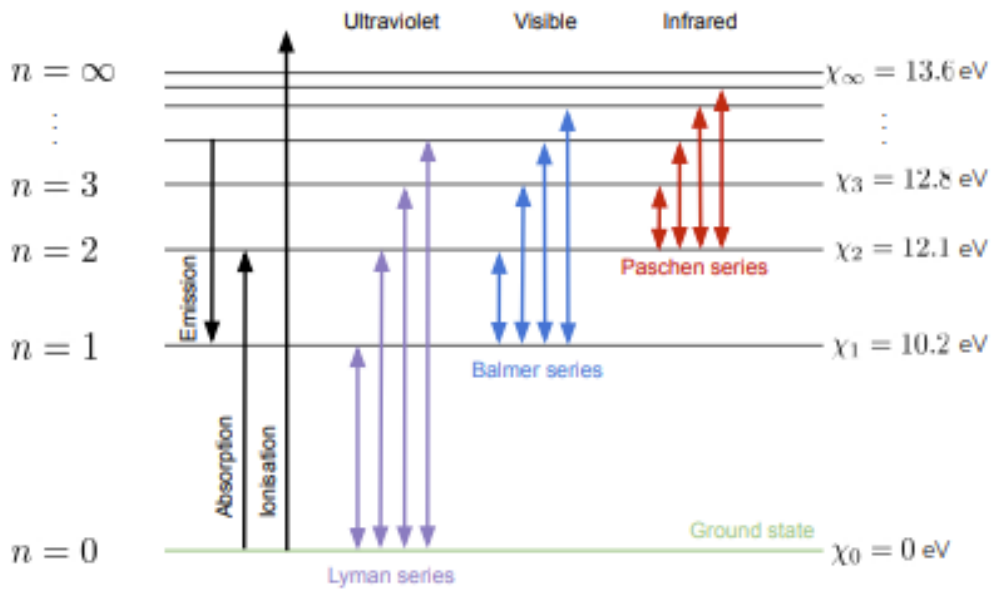


Figure 3.3: Energy levels of a H atom (Winckel, 2016).

Figure 3.3 illustrates the energy levels of a H atom, clearly showing different series including the Balmer series in blue.

3.2.2 Stellar Parameters

3.2.2.1 Effective Temperature

Effective temperature (T_{eff}) represents the temperature of a blackbody that emits an equal amount of energy as a star. As is defined, it is the bolometric surface brightness of a star (in units of K) and linked to the star's colour and spectral type (Massey et al., 2005). Stars emit energy across various wavelengths, but they have a dominant wavelength range for energy emission. Wilhelm Wien's investigations (Rechenberg, 1982) introduced the concept of a *'blackbody'* and revealed that a perfect blackbody's peak energy wavelength is inversely proportional to its temperature, known as Wien's Law. This law states that objects with varying temperatures produce a spectrum with peak wavelengths inversely corresponding to their temperatures.

$$\lambda_{\max} = \frac{b}{T}, \tag{3.3}$$

Where:

- $\lambda_{\max}$ is the peak wavelength of energy emission.
- b represents the Wien's displacement constant; $b \approx 2.8977 \times 10^{-3}\text{m} \cdot \text{K}$.
- T represents the absolute temperature (K).

3.2.2.2 Surface Gravity

Surface gravity (g) quantifies the gravitational attraction at the stellar surface. It is calculated using the formula:

$$g = \frac{GM}{R^2}. \tag{3.4}$$

The stellar mass is denoted by M, the radius by R, and the gravitational constant by G (Massey et al., 2005).

3.2.2.3 Apparent and Absolute Magnitude

Apparent magnitude (m) measures how bright a star is observed from Earth. It is a logarithmic scale, where brighter stars have lower magnitudes. Apparent magnitude is often used to classify stars based on their brightness. Absolute magnitude (M) is expressed as the intrinsic brightness of a stellar object. This is an apparent magnitude of an object placed at a standard distance of 10 parsecs, approximately 32.6 light-years, from Earth (Jaschek & Jaschek, 1990). The relationship between m and M is given by:

$$M = m - 5 \cdot \log_{10}(d) + 5. \tag{3.5}$$

3.2.2.4 Bolometric Magnitude

Bolometric magnitude (M_{bol}) takes into account the total energy output of a star across all wavelengths. The Stefan-Boltzmann law relates the luminosity (L) of a star with its effective temperature and radius (R) (Jaschek & Jaschek, 1990). Bolometric magnitude provides a measure of the intrinsic brightness of a star.

$$M_{\text{bol}} = -2.5 \log_{10} \left(\frac{L}{L_{\odot}} \right) + 4.74, \tag{3.6}$$

Where 4.74 ($M_{bol,\odot}$) represents the bolometric magnitude of the Sun. The bolometric magnitude is also related to the absolute visual magnitude (M_V) by the formula:

$$M_{\text{bol}} = M_V + BC, \tag{3.7}$$

Where BC, bolometric correction is a correction factor applied to the visual magnitude to account for the contribution of radiation at other wavelengths. The formula expresses how the total brightness of a celestial object across all wavelengths (bolometric magnitude) is related to its brightness in the visual part of the spectrum (absolute visual magnitude). The bolometric correction is added to the absolute visual magnitude to obtain the bolometric magnitude.

3.2.2.5 Luminosity

Luminosity (L) represents the total amount of energy emitted by a star per unit time. Luminosity is a fundamental parameter that provides insights into the energy output and evolutionary stage of a star. The Stefan-Boltzmann law is used to calculate L:

$$L = 4\pi R^2 \sigma T_{\text{eff}}^4, \tag{3.8}$$

where σ is the Stefan-Boltzmann constant (Jaschek & Jaschek, 1990).

3.2.2.6 Stellar Motion (Doppler Shift)

Stellar motion, indicated by the Doppler shift, provides information about the radial velocity of a star. The Doppler shift is quantified by the equation:

$$\frac{\Delta\lambda}{\lambda} = \frac{v_r}{c}, \tag{3.9}$$

where λ represents the rest wavelength, $\Delta\lambda$ as the wavelength shift, c represents the speed of light and v_r is the radial velocity. The Doppler shift allows astronomers to measure the motion of stars towards or away from Earth, providing insights into their kinematics and dynamics.

3.2.2.7 Metallicity $[M/H]$

While H and He constitute the predominant elements in a star, it is crucial to recognize the significance of other elements as well. The concept of metallicity encompasses various interpretations (Hinkel et al., 2014). The equation presented is expressed in relation to the solar abundance:

$$[M/H] = \log_{10}\frac{M}{H} - \log_{10}\frac{M_\odot}{H_\odot} \tag{3.10}$$

where M represents the number of particles for all metallic elements in a given star, H denotes the number of H particles in the same star (Matteucci, 2001), and $\odot$ signifies the corresponding values in relation to the Sun. This formulation defines the metallicity of the Sun as 0 (Martin & Morrison, 1998). It is important to note that metallicity does not account for the abundance of individual elements but rather captures a broader trend. While there are variations in the relative abundance between elements, they generally align with the composition of the Sun. This same formula applies to the assessment of individual element abundances as well, with M being substituted by the relevant element.

3.2.3 Stellar Atmospheres

The aim here is to cover the aspect of star atmosphere related to this study. This includes a short introduction to stellar spectral energy distribution (SED), spectrum elements, continuum, and spectrum lines. Observational effects are explained in section 3.2.4 while section 3.2.5 introduces the method of modelling stellar atmospheres. The following sections are based on the lectures on the Radiation Processing Astronomy Course by Winckel (2016).

3.2.3.1 Spectral Energy Distribution

The SED of a star illustrates the energy released across different wavelengths, representing the radiation emanating from the stellar atmosphere. Planck's law states that a celestial body in thermal equilibrium with its surroundings emits radiation throughout a broad spectrum of wavelengths. The SED of the star closely resembles the profile of the blackbody radiation curve, determining the effective temperature of a star. Estimating the total light intensity at each wavelength, SED can be created. When measuring light intensity in normal circumstances, a spectrum of insignificant wavelengths are covered by filters, called "pass bands". The majority of photometric systems use a set of pass bands that are calibrable against reference stars to quantify light intensity. Since the magnitude and intensity of these stars have been established, it is possible to determine the magnitude of the star in its pass band. The energy distribution of a blackbody at $\lambda \gg k_B T$ is represented as

$$B_\lambda(T) = \frac{2ck_BT}{\lambda^4} \tag{3.11}$$

This approximation is called the Rayleigh-Jeans tail, where Boltzmann constant is $k_B = 1.380649 \times 10^{-23}$ J K^{-1} which measures the relationship between temperature and the average kinetic energy of particles in a system. In the case of a massive star, the Rayleigh–Jeans equation (Pais, 1979) is already able to approximate the visual wavelength.

3.2.3.2 Spectrum

The star's spectrum provides comprehensive details about the characteristics of its radiation.It provides details concerning the elements in the star's atmosphere as well

as how they are populated in the distribution across their many transition stages. There are several particles that make up the stellar atmosphere. In less cooler stars, particles are ionized electrons and atoms, and in very cold stars there are more molecules and atoms. The radiation produced by the nuclear reaction of the star's nucleus interacts with these particles. Then we observe the radiation after the interaction. The interaction between radiation within a star layer and photosphere material, is determined by the radiation transfer equation. That is,

$$\frac{dI_\nu}{d\tau_\nu} = -I_\nu + S_\nu \tag{3.12}$$

The radiation returning from behind the star's inner layer is denoted by I_ν, whereas the radiation returning from the stars photosphere is represented by S_ν also called the source function. The parameter τ_ν quantifies the amount of radiation observed from beyond the star's layer, known as optical depth.The solution to the radiative-transfer equation varies with the wavelength. The spectral continuum is sometimes referred to as the foundation of the star's spectrum in the black-body radiation. Beyond this continuum, the existence of certain elements whose values are given by the radiative-transfer equation allows for the separation of several absorption and emission lines.

3.2.3.3 Continuum

A continuum is derived from a bf (bound-free transition) of ions and atoms, as well as a free-free transition referred to as Bremsstrahlung. bf transition refers to the process where an electron bound to an atom or ion absorbs sufficient energy to escape from the binding potential of the nucleus. This transition occurs when an incoming photon has energy equal to or greater than the ionization energy of the electron in its initial bound state. Also the electromagnetic radiation caused by the charged particles' acceleration or deceleration in the coulomb field, such as the collision of ions and electrons. Photon absorbance having energy equal to or greater than the ionization energy of electrons in the bound n-state produces the area of the continuum formed by bf-transitions.

The ground state is represented by an energy level $n = 0$, and the energy of an electron in a bound state, $n > 0$ is provided by, $\Delta\chi_{n0} = \chi_n - \chi_0$. The energy of the level n is denoted as χ_n, and $\chi_0 = 0$. Electrons that are free may arbitrarily contain huge amounts of kinetic energy ($\frac{mv^2}{2}$), m represented as the electron mass and v as

the velocity. **bf**-transitions are associated with a photon energy by,

$$h\nu = \chi_\infty - \chi_n + \frac{mv^2}{2} = \Delta\chi_\infty n + \frac{mv^2}{2} \quad , \tag{3.13}$$

In equation 3.13, $h = 4.135667 \times 10^{-15}\,\text{eV s}$, χ_∞ represents the energy required to ionize an atom in a ground state. Ionizing H in its ground state requires the energy of a photon to be $h\nu \geq 13.6\,\text{eV}$. Conversely, capturing an electron in its ground state produces a photon with energy $\geq 13.6\,\text{eV}$.

3.2.3.4 Spectral Lines

Spectral lines can either arise from absorption or emission as shown in Fig 3.4 in relation to the continuum. Absorption lines occur when specific wavelengths (see Fig 3.7) of photons are absorbed from an incident light, distinguishing them from other slightly varied photon wavelengths within the continuum. An emission line is produced when there is an abundance of photons at a particular wavelength compared to photons with slightly different wavelengths.

Spectral lines arise from a discrete transition between bound states of electrons, known as bb-transitions, which involves the transition of electrons between energy levels denoted by $n < \infty$. The transition to a higher energy level, called excitation, can occur through the absorption of kinetic energy, also known as collisional excitation or a photon absorbed (radiative excitation). The process of de-excitation, involving a transition to a lower energy level, can be induced either through a collisional de-excitation or through the photon emission (radiative de-excitation). Equation 3.14 determines the energy of a photon involved in a radiative transition.

$$h\nu = \chi_m - \chi_n = \Delta\chi_{mn} \tag{3.14}$$

In the case of the H atom, the transitions are categorized into series based on the energy levels participating in the electron jump. The Lyman series encompasses all transitions involving the ground state, with $n = 0$, while the Balmer series includes transitions associated with the first excited state $n = 1$. Similarly, the Paschen series includes transitions associated with $n = 2$.

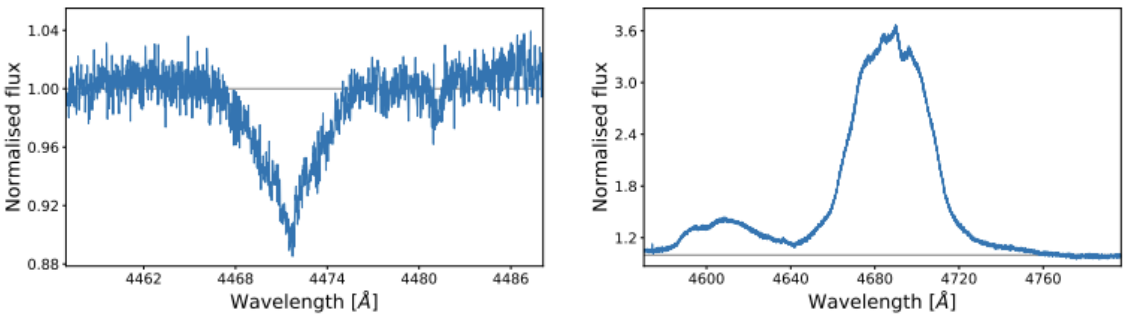


Figure 3.4: An illustration of emission line (right) and an absorption line (left) for BAT99 126 (Janssens et al., 2021).

Fig. 3.4 provides an illustration of both emission and absorption lines. There are just under a hundred naturally occurring elements, and about 300 isotopes in the solar system. The solar system has over 300 isotopes and somewhat less than 100 naturally occurring elements.

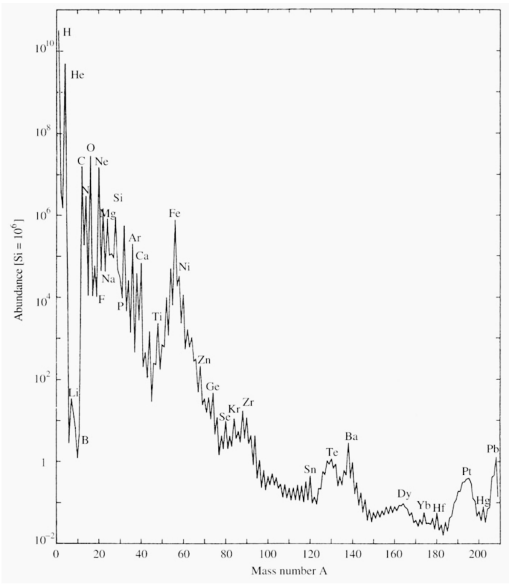


Figure 3.5: Element abundances as a function of the nuclear mass number (A) (Karttunen et al., 2007).

Fig. 3.5 shows the abundances of elements as a function of their nuclear mass number (A) in the solar system. Elements found in the periodic table are formed through a successive burning of lighter elements H to He and He further to C, O and heavier elements (eg. Fe).

Fig. 3.6 depicts magnitudes of absorption lines associated with diverse chemical components (atoms, ions, molecules), transitioning from hotter (left) to cooler (right) stars. It shows that our target might produce neutral He lines, strong H lines, weak ionized metal (e.g. Fe and Mg) lines.

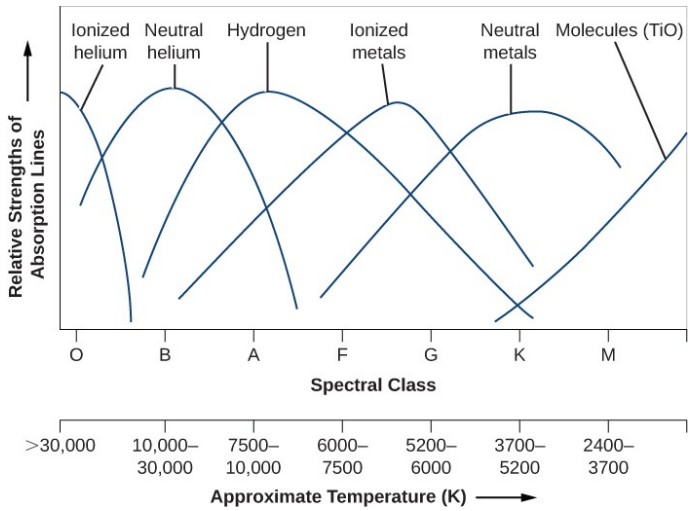


Figure 3.6: Variations in Absorption Lines across stars with different temperatures (CNX, 2023).

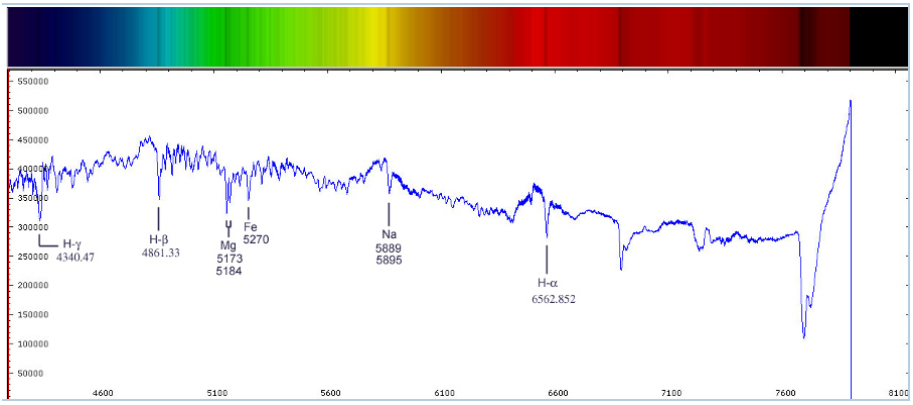


Figure 3.7: Illustration of a spectrum showing the spectral lines (FROGS, 2023).

Fig 3.7 shows spectral lines across the wavelength with black lines indicating absorption features present in the illustrated spectrum. These lines correspond to specific elements present in the star, as shown by the dips in the blue line spectrum.

3.2.3.5 Stellar abundance

The fundamental approach for ascertaining abundances relies on evaluating the intensity of an absorption line. This is achieved by initially estimating the spectrum's profile without the absorption line and subsequently quantifying the cumulative absorption concerning the reference. The equivalent width (EW), W_λ has the following relation to a residual flux of a spectral line:

$$W_\lambda = \int \left(1 - \frac{F_{\text{continuum}}(\lambda)}{F(\lambda)}\right) d\lambda \tag{3.15}$$

Where:

- W_λ is the EW of the spectral line.
- $F(\lambda)$ represents the flux of the spectral line at wavelength λ.
- $F_{\text{continuum}}(\lambda)$ is the flux of the continuum (the background) at the same wavelength λ.
- The integral sign $\int$ denotes the integration over the range of wavelengths where the spectral line is observed.

W_λ (expressed in Ångströms) of a completely opaque line signifies that it absorbs the entire amount of light as the observed line. As such, the faintest discernible line relies on factors like resolution and data noise, but relatively low equivalent widths below 0.01 Ångströms have been quantified using high-quality observations (Tennyson, 2019). Interpreting necessitates a model of the stellar atmosphere, entailing knowledge of the inherent absorption characteristics of an atom at the specific wavelength and the atom density in the corresponding absorbing state. By using measurements of EW, it is feasible to deduce the abundance of an element for which absorption lines within the gas in the stellar atmosphere are detectable and measurable. This process integrates the Boltzmann and Saha equations, considering the pressure and temperature of the gas, to compute the abundance of an element.

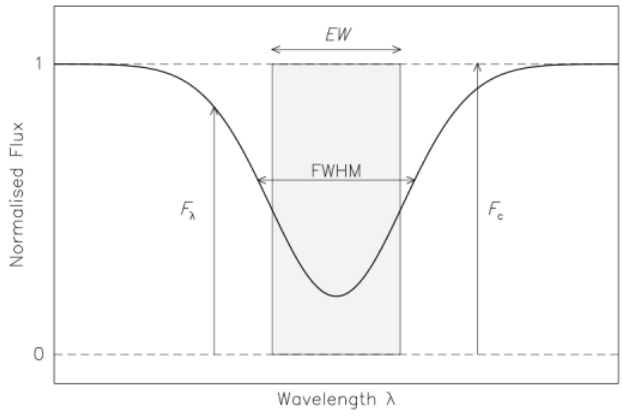


Figure 3.8: The components of an absorption line showing EW illustrated in grey adopted from (Letarte, 2007).

Fig 3.8 shows the Full Width at Half Maximum (FWHM) of a spectral line. Alternatively, it is the separation on the curve between the two points at which the intensity

drops to half of its maximal value. It also shows the width of a grey rectangle (EW) whose area is equal to that of the absorption line as shown.

The properties of a spectral line: its shape and intensity, are influenced by the abundance of the element N_a. In astrophysics, abundance measurements are expressed numerically and often compared to Solar values (stellar abundances). The metallicity of stars is commonly denoted by the number ratio of Fe atoms to H atoms per unit volume, relative to solar values:

$$[Fe/H] = \log_{10}\left(\frac{N_{\rm Fe}}{N_{\rm H}}\right)_{\rm star} - \log_{10}\left(\frac{N_{\rm Fe}}{N_{\rm H}}\right)_{\rm Sun}. \tag{3.16}$$

Here, $N_{\rm H}$ and $N_{\rm Fe}$ represent the numbers of H and Fe atoms in a unit volume. This expression provides a quantitative assessment of metallicity by comparing stellar abundances to the solar reference. Table 3.1 shows distinctive absorption and emission lines for each star. The unknown $T_{\rm eff}$ is determined by fitting an Hβ or Hα line profiles. Therefore, the identification of possible pulsating Maia candidates such as NGC 3766 (Mowlavi et al., 2013) and NGC 1893 (Lata et al., 2014) in open clusters is essential because the location of a star along the MS provides a more accurate measure of $T_{\rm eff}$.

Table 3.1: Distinctive spectral lines at their temperature ranges (Collaboration, 2023).

Spectral Type	**Temperature (K)**	**Spectral lines**
O	28 000 - 50 000	Ionized He
B	10 000 - 28 000	He, some H
A	7 500 - 10 000	Strong H, some ionized metals
F	6 000 - 7 500	H, ionized K and Fe
G	5 000 - 6 000	Neutral and Ionized metals, especially K
K	3 500 - 5 000	Neutral metals, Na
M	2 500 - 3 500	Strong TiO, very strong Na

To identify the positions of absorption and emission lines for various elements, Table 3.2 below outlines the approximate locations in the electromagnetic spectrum for some of the more commonly encountered elements.

Table 3.2: Wavelengths of various elements for specitic spectral lines (Collaboration, 2023).

Spectral lines	**Wavelengths (Å)**
Hα, Hβ, Hγ	6600, 4800, 4350
Ionized H and K lines	3 800 - 4 000
TiO	lots of lines from (4 900 - 5 200), (5 400 - 5 700), (6 200 - 6 300), (6 700 - 6 900)
G Band	4 250
Na	5 800
He (neutral)	4 200
He (ionized)	4 400

In addition Balona et al. (2016) determined the parameters for SPB/Maia-type stars as: the $T_{\rm eff}$, was found to be 18900 ± 660 K, *logg*, was determined to be 4.16 ± 0.17, and [Fe/H], was measured to be -0.4 ± 0.1. These values provide key insights into the characteristics of SPB/Maia-type stars.

3.2.4 Observational Effects

Various factors can introduce variations and distortions in the observed spectra and light curves, including interstellar reddening, limb darkening, atmosphere extinction, and gravity darkening. It is crucial to consider these effects when analyzing both spectroscopic and photometric data.

3.2.4.1 Interstellar Reddening

The light emitted by stars traverses the interstellar medium on its way to our telescopes, which is the region of space that exists between stars and comprises of gases and dust particles (Karttunen et al., 2003). Dust grains within this medium typically have sizes comparable to the wavelengths of visible spectrum photons. When starlight penetrates an interstellar medium, the light is scattered by both the dust and gas particles in the path of observation. The presence of dust grains with characteristic sizes results in visible and ultraviolet light being highly susceptible to scattering. In contrast, infrared radiation is less affected by this scattering phenomenon. As a consequence, fewer photons emitted by a star are detected by our telescopes due to scattering effects in the visible and ultraviolet ranges. However,

photons in the infrared range experience less scattering, allowing more of them to reach our telescopes for detection. This gives rise to the phenomenon known as interstellar reddening, causing stars to appear redder than their intrinsic colour (Dopita et al., 2003). Photometric data needs to be corrected for interstellar reddening, as neglecting this effect can lead to inaccurate magnitudes and flux measurements. The amount of reddening is determined by examining $B - V$ which is the colour index of an object and comparing it to $(B - V)_0$ which is its intrinsic colour index using the provided equation:

$$E(B - V) = (B - V) - (B - V)_0 = A_B - A_V \tag{3.17}$$

where A_B and A_V are the extinctions in the blue and visual bands, respectively.

3.2.4.2 Limb Darkening

The light detected by the telescope is not always from a similar stellar layer. Examining an imaging of the Sun shows that the periphery is not as bright as its central region. Limb darkening is an observational effect seen in stars, particularly those observed at an angle where their outer edges, or limb, are visible. This effect occurs because the temperature and density of a star's atmosphere decrease with increasing distance from its center. As a result, the intensity of radiation emitted by the outer layers of the star is lower compared to that emitted by its core. The light detected by telescopes emanates from specific depths in the interior of a star. A light beam must travel a certain distance in the stellar atmosphere before it may come into contact with a star material. Because of this, compared to radiation coming from the central region of the star, radiation that reaches the outskirts of a star originates from cool-higher layers, leading to the periphery of a star darkening. Limb darkening is contingent upon the angle of radiation leaving the star reference to the surface of the star (γ), which is represented by $\mu \equiv \cos\gamma$. As for stars that have low T_{eff} (eg. the Sun), limb darkening is best described by the linear-cosine law, which is a linear function of μ (Diaz-Cordoves et al., 1995). In contrast, for some stars which have $T_{\text{eff}} > 8,500\,\text{K}$, the square-root law, which is proportional to the square root of the angle ($\sqrt{\mu}$), provides a more accurate description of limb darkening (Diaz-Cordoves & Gimenez, 1992). Consequently, limb darkening influences the light curves of eclipsing binary star systems. When the eclipsing star transits in front of the other star, initially covering the limb, allowing less amount of light to be obstructed in comparison to the time it is centrally positioned. Therefore, this

dynamic results in alterations in the shape of the lower boundary of an eclipse.

3.2.4.3 Gravity Darkening

There is a necessity for the correction of gravity darkening due to the impact of the shape of a star being distorted, induced by the gravitational influence of a nearby companion or very rapid rotation. This is also explained in Section 2.2.2.2 on the effect of stellar rotation on pulsations. In these scenarios, the star takes on the appearance of an oblate spheroid, with the poles experiencing compression and, consequently, higher temperatures compared to the less dense equatorial regions. Consequently, the equator of the star becomes dimmed, while the poles exhibit heightened brightness. The phenomenon, often referred to as gravity brightening, is described in detail by White et al. (2012). Correcting for gravity darkening is essential as it ensures accurate interpretation and analysis of stellar data, particularly in situations involving binary star systems (Lara & Rieutord, 2012) or rapidly rotating stars (Lara & Rieutord, 2011), where this effect has a major impact in shaping the observed characteristics and behaviors of celestial bodies.

3.2.5 Model Atmospheres

The existence of spectral lines related to a specific atomic transition is influenced by the abundance of elements in that state or level population. For instance, if there is a minimal amount of single ionized Helium (He II), the corresponding spectral lines for the atomic transitions of He II will be either very faint or entirely absent. An existence or absence of a spectral line in the spectrum corresponding to the transition of an element/atom determines the spectral type of a star. Most of the star's life is derived from spectral lines emanating from its photosphere, which absorbs the continuum. Section 3.2.1 contains more information about the spectral classification .

The approximation of the stellar photosphere is called the **Local Thermal Equilibrium (LTE)** (Suslick, 2001). According to this estimation:

The different atomic levels of particles in their populations within a volume are in a state of chemical equilibrium regarding their populations (chemical equilibrium),

Every other force at every location counteract the pressure force at mechanical/hydrostatic equilibrium, all while maintaining a uniform temperature throughout that specific

volume (thermal equilibrium).

The combination of chemical and thermal equilibrium results in thermodynamic equilibrium. However, there is no thermal equilibrium throughout a star, as there is a significant temperature gradient from the very dense and hot core to the cooler furthest outer layer. Therefore, the idea that the temperature of a star is fixed cannot be made. However, in localized regions, typically in very thin layers, a consistent temperature is observed, and the criteria for thermal equilibrium are satisfied. Consequently, LTE is applied, making the assumption that relative population distributions with different atomic layers are only dictated by thermodynamic factors: which are electron pressure and temperature. There are two key mathematical expressions, namely the Boltzmann excitation law and the Saha ionization law, govern these relative populations (Suslick, 2001).

3.2.5.1 Excitation Law of Boltzmann

The Boltzmann relation describes how excitation states are distributed within the same ionization state, this implies that:

$$\frac{n_{r,s}}{n_{r,t}} \propto e^{-(\chi_{r,s}-\chi_{r,t})/k_B T}, \tag{3.18}$$

where $n_{r,t}$ and $n_{r,s}$ are the number densities of ionisation state r and in excitation level s and t, respectively, $\chi_{r,t}$ and $\chi_{r,s}$ are the corresponding energies.

3.2.5.2 Ionisation law of Saha

The Saha relation provides the proportion of number densities for two successive ionization levels in $n = 0$ (ground state), that is:

$$\frac{n_{r+1,0}}{n_{r,0}} \propto \frac{1}{N_e}(k_B T)^{3/2} e^{-(\chi_{\infty r,0})/k_B T} \tag{3.19}$$

Where N_e is the electron number density and the $\chi_{\infty r,0}$ is the ionisation energy of $n = 0$ with ionisation state r.

The occurrence of LTE can be postulated in situations where the pressure force is predominantly influenced by collision. In stellar atmospheres, where the density is

significantly lower, radiative processes play a crucial role. Under these conditions, the Boltzmann and the Saha equations respectively, no longer exclusively dictate the relative populations of various atomic levels, because the influence of the radiation field becomes significant. This situation leads to non-equilibrium conditions known as non-LTE.

In non-LTE circumstances, these equations exhibit interdependence among themselves as well as its radiation field and populations influence the radiation field. The resolution of equations under non-LTE conditions presents a challenging and intricate task. It is important to solve all equations concurrently with the equation of radiative transmission. Non-LTE model atmospheric codes that answer every equation concurrently have been developed. FASTWIND (Puls et al., 2005), TLUSTY (Lanz & Hubeny, 2003), Potsdam Wolf-Rayet model atmosphere code (PoWR) (Hamann & Gräfener, 2003) and the CMFGEN (Hillier & Miller, 1998) are a few examples of these codes.

3.2.5.3 Microturbulence Velocity

The microturbulence velocity, denoted as ν_t, impacts spectral lines by introducing broadening, leading to their desaturation. This phenomenon arises from small-scale motions in the photosphere and is treated as an additional thermal velocity in the absorption coefficient of the line. Desaturation primarily affects strong lines, while weak lines remain unaffected since an increase in ν_t broadens the line without significantly altering its depth, thereby conserving the equivalent width (EW). In the case of weak lines, the abundance is directly proportional to the EW. However, for saturated lines, an increase in ν_t broadens the wavelength range of absorption, resulting in desaturation where the equivalent width is no longer conserved. A typical value for ν_t is around 2km s^{-1} for MS stars, as adopted from Kupka et al. (1999). To determine ν_t for a star, one ensures that for a single element, the abundance remains independent of the EW of the line.

3.2.5.4 VALD Atomic Line Database

The Vienna Atomic Line Database (VALD) is a comprehensive online database containing information about atomic and molecular transition parameters. It provides data on the energy levels, wavelengths, and oscillator strengths of spectral lines for a wide range of chemical elements. The VALD database is utilized to produce a

synthetic spectrum line list. This line list includes information about the absorption lines which are expected to appear in a star's spectrum. These lines are crucial for the evaluation of synthetic and observed spectra. For this study we will employ the synthetic spectra method, utilizing the `SYNSPEC` code, particularly `SYNSPEC,54`, developed by Hubeny et al. (2021). The atmospheric modelling involves Kurucz LTE stellar atmosphere models generated using the `ATLAS12` code (Kurucz, 1993). Assuming a microturbulence of 2 kms^{-1}, a VALD line list is generated (Kupka et al., 1999).

3.2.5.5 Synthetic Spectra

Synthetic spectra are artificially generated spectra created through computer simulations. These spectra are computed based on theoretical models of stellar atmospheres, incorporating information about the identified absorption lines. The synthetic spectra are later compared to the actual observed spectra. This process is used to analyze the differences between the two, helping to derive information about the stellar atmosphere, such as temperature, pressure, and chemical composition (Palacios et al., 2010).

`ATLAS 12` provides model atmospheres in the range of 3 250 K $\leq T_{\mathrm{eff}} \leq$ 52 500 K (Kurucz, 1993). This iteration of the `ATLAS` LTE blanketed model atmospheres incorporates the Opacity Sampling technique to account for line opacity in stellar atmospheres. These models are based on assumptions of a plane-parallel geometry, hydrostatic and radiative equilibrium, and LTE. `ATLAS 12` models can be generated for specific individual abundances and microturbulent velocity values. Convection in `ATLAS 12` is implemented using the MLT (Mixing-Length Theory) formalism. In all the models, the microturbulent velocity, maintained as a constant throughout the depth, is set at 2km s^{-1}.

The continuous opacities in `ATLAS 12` remain consistent with those in `ATLAS 9`, including elements such as HI, H-, H2+, He I, He II, He- and various metallic absorbers like C I-IV, Mg I-II, Al I, Si I-II,Fe I, Ca II, N II-V, O II-VI, Ne I-VI. There are also other examples, such as electron scattering and (H, H2, and He I) Rayleigh scattering. Kurucz's CD-ROMs contain all of the atomic and molecular lines from which the line opacity is calculated.

`SYNSPEC` (Hubeny et al., 2021) is a versatile LTE spectrum synthesis program, and it takes input from an `ATLAS` model atmosphere and a comprehensive line list, dynamically choosing lines that contribute to the total opacity based on the physical

parameters of the specific model atmosphere. `SYNSPEC` subsequently solves the radiative transfer equation for each wavelength within a specified wavelength range corresponding to their specific resolution.

3.2.6 Spectral Energy Distribution (SED) Analysis with VOSA

3.2.6.1 The Kurucz ODFNEW/NOVER Atmosphere Models and PARSEC1.2 Model

The `Kurucz ODFNEW/NOVER` atmosphere models, developed by Castelli & Kurucz (2003), along with the `PARSEC1.2` model Bressan et al. (2012), constitute fundamental components in the computational framework employed for Spectral Energy Distribution (SED) analysis in astrophysics. SED analysis involves studying the energy output of celestial objects, such as stars or galaxies, across various wavelengths, providing insights into their properties, composition, and evolutionary stage. These models serve the primary purpose of characterizing the physical properties of stars based on observational data, particularly their spectral energy distributions. Leveraging input data consisting of photometric measurements obtained across various wavelengths and calculated stellar parameters such as temperature, surface gravity, and metallicity, the Kurucz atmosphere models simulate the intricate radiation processes occurring within stars, encompassing absorption, emission, and scattering of light.

The `PARSEC1.2` model provides evolutionary tracks (stellar isochrones), representing theoretical models of stellar evolution incorporating factors such as mass, age, and chemical composition. Through SED analysis, these models are fitted to observational data, facilitating parameter optimization to derive best-fit parameters that yield insights into the physical properties and evolutionary status of the stars under investigation. The output of SED analysis, including effective temperature, surface gravity, and metallicity, contributes significantly to diverse astrophysical studies such as stellar classification, age determination, and galaxy evolution.

3.2.6.2 VOSA (Virtual Observatory SED Analyzer)

VOSA (Virtual Observatory SED Analyzer) (Bayo et al., 2008) is a versatile and powerful tool specifically designed to efficiently analyze photometric data of celestial

sources. Its workflow begins by ingesting user-provided photometry tables, which can be in either American Standard Code for Information Interchange (ASCII) or Virtual Observatory Table (VOTable) format, containing essential information such as source identifiers, coordinates, distances, visual extinction values, filter names, observed flux/magnitude, and corresponding errors. Leveraging Virtual Observatory (VO) (Djorgovski & Williams, 2005) services, VOSA then queries multiple photometric catalogs, including well-known ones like 2MASS, Tycho-2, and Stromgren (Apellániz, 2006), to augment the available data and increase wavelength coverage.

Once the photometric data is gathered, VOSA proceeds to retrieve theoretical spectra from VO-compliant databases, such as the The Spanish virtual observatory (SVO) (Gutiérrez et al., 2006) theoretical data server, covering a range of physical parameters specified by the user. Using these datasets, VOSA calculates synthetic photometry for the observed filters, carefully considering the spectral resolution and response curves of each filter. It applies statistical tests to identify the best-fitting model that minimizes the reduced χ^2 value, providing users with the most accurate representation of the observed data.

With the best-fit model in hand, VOSA performs further analyses to estimate the total observed flux for each source and subsequently calculates their bolometric luminosity. This process takes into account user-provided distance values or assumes a generic value of 10 parsecs when distance information is unavailable.

Additionally, VOSA offers visualization capabilities by generating Hertzsprung-Russell (HR) diagrams, allowing users to explore the estimated parameters and compare them with different sets of isochrones and evolutionary tracks. Through interpolation among collections of isochrones and evolutionary tracks, VOSA provides estimates of the mass and age of individual sources, offering valuable insights into their physical properties and evolutionary status.

3.3 Photometry

3.3.1 Transiting Exoplanet Survey Satellite-*TESS*

TESS is designed to be a predominant exoplanet-hunting satellite, dedicated to observing planetary transits around luminous stars. It is a parametric algorithm that was devised to meticulously select 'high-priority' stars for short cadence observation. These selected stars encompass MS, subgiant, and red giant stars capable of exhibit-

ing detectable solar-like oscillations. The utilization of short cadence observation by *TESS* holds the potential to revolutionize both the domains of asteroseismology and exoplanetary science.

The spatial resolution of *TESS*, as outlined by Campante et al. (2016), corresponds to approximately 21.1 arcseconds per pixel. The system boasts a total of 1048 x 1048 usable pixels across its four cameras, enabling it to survey an expansive 24°x96° field of view. Its orbital trajectory involves two revolutions around Earth within a 27.4-day sector, during which data is downlinked while it resides at perigee for roughly 16 hours. Consequently, this leads to a relatively small data gap in comparison to the overall observational period. Notably, *TESS's* distinct bandpass captures a redder portion of the electromagnetic spectrum compared to *Kepler*, primarily due to the emphasis on locating Earth-like candidates around cooler red dwarf stars.

In 2018 April, NASA successfully launched the *TESS*, as detailed by Ricker et al. (2015). *TESS* systematically divides the celestial sphere into 26 sectors, effectively encompassing both the southern and northern skies with 13 sectors each. Within each sector, continuous observation is conducted for 27 days, allowing for comprehensive coverage of the entire sky over a span of approximately 2 years. Every sector offers a wide field of view measuring 24°×96°, producing 2-minute short cadence light curves for around 20,000 target stars. Additionally, it provides full-frame images every 30 minutes. Its primary mission objective is the detection of Earth-sized planets transiting luminous and nearby stars. Concurrently, its extensive and high-precision photometric data opens unprecedented avenues for studying binaries and variable stars, particularly those that are bright and prominent. Notably, a significant contribution to this realm is the catalog published by Balona & Ozuyar (2020), featuring 766 pulsating MS B-type stars observed by *TESS* in sectors 1–18, significantly expanding the available sample list.

3.3.2 Band-pass

For the current study, a band-pass of *TESS* satellite range from 600 to 1000 nm and the 400 nm width was found to be the most possible option for optical design. The outermost limit of silicon CCD sensitivity is represented by the red end of the spectrum. Additionally, the use of a long-pass filter with a 600 nm cut-on wavelength helps to limit the spectral response at its blue end, as discussed by Sullivan et al. (2015).

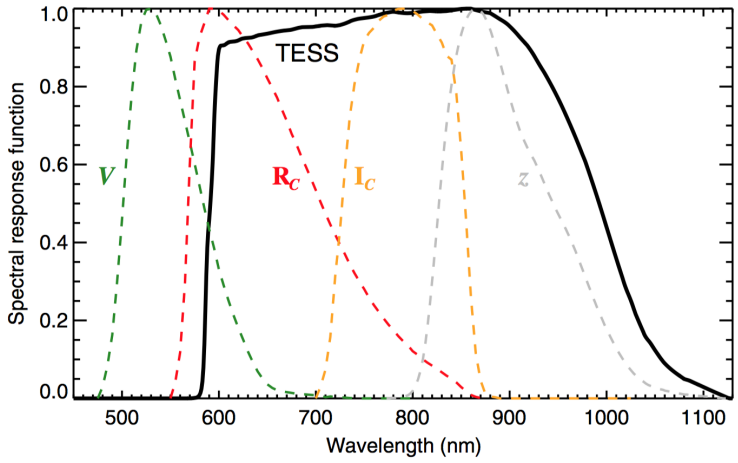


Figure 3.9: The *TESS* spectral response function (black line) along with Johnson-Cousins and SDSS z filter curves for comparison (Ricker et al., 2015).

Fig 3.9 reppresents the *TESS* spectral response function (depicted as a black line), comprising the long-pass filter transmission curve and the detector quantum efficiency curve. Filter curves as well as Johnson-Cousins, along with the SDSS z filter curve, are additionally showcased for comparative purposes. The maximum value of each function has been normalized to unity, as per the scaling approach outlined by Ricker et al. (2015).

Chapter 4

Data Analyses

Data analyses for the Maia star TIC 202431888 were carried out by using the *TESS* photometry and high-resolution ground-based spectroscopy. During the analyses the theoretical models were used in the following codes: `Kurucz ODFNEW/NOVER` (Castelli & Kurucz, 2003) and `PARSEC1.2` (Bressan et al., 2012) (for the HR diagram), Kurucz LTE stellar atmosphere models with the `ATLAS 12` code (Kurucz, 1993), and the `SYNSPEC 54` code Hubeny et al. (2021) (for stellar atmospheric paremeters, projected rotational velocity and metallicity).

4.1 Frequency Analysis of TIC 202431888

The Maia target TIC 202431888 was selected based on a study by Balona & Ozuyar (2020). The star was listed among the Maia-type stars and categorized as one of the high priority candidates to be investigated. Table 4.1 presents the fundamental properties presented by *TESS* using the *TESS* Input Catalogue (Stassun et al., 2018).

Table 4.1: *TESS* Input Catalogue Parameters given for TIC 202431888.

α (J2000) (deg)	δ (J2000) (deg)	Spec type	Mag	$T_{\rm eff}$ (K)	Radius ($M_\odot$)	Mass ($M_\odot$)	Distance (pc)
6.276711	53.046778	B9IVSi	5.7	11960	3.520	3.191	170.57

The light curves obtained from the *TESS* mission are publicly available through the Mikulski Archive of Space Telescope Portal (MAST) Data archive, on the MAST website Barbara A. Mikulski (2023). The MAST archive contains Simple Aperture Photometry (SAP) and the Pre-search Data Conditioning Simple Aperture Photometry (PDCSAP) flux files. The light curves are extracted and conditioned for instrumental contributions using a process called pre-search data conditioning (PDC) (Jenkins et al., 2016). The conditioned light curves are labelled the PDC-SAP flux in the FITS files. *TESS* light curves represent how the flux of pulsating

celestial objects changes over time. The light curves provides information about the pulsation periods and amplitudes of the pulsating celestal objects. Analyzing these data can provide details about stellar parameters, including composition and evolutionary stage (Lund et al., 2021). It is essential to convert the time-series data from the time domain to the frequency domain and depict it as a frequency spectrum. The *TESS*, with its high-precision photometry and extensive coverage, has provided valuable data for studying pulsating stars and advancing our understanding of their properties.

TIC 202431888 was observed with 120 s exposures in 2019, 2022, and the data were publicly available on the MAST in the *TESS* sectors 17, 57 and 58. For the frequency analyses, a total of 2012 continuous data points in the sector 57 and 58 were used.

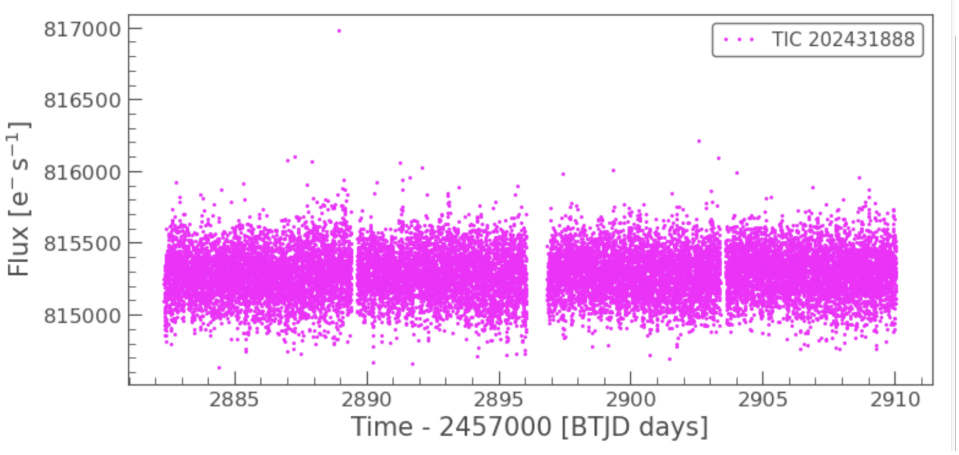


Figure 4.1: The normalized *TESS* data for the star TIC 202431888 available in the sectors 57 and 58.

Fig 4.1 shows the normalized *TESS* data in the selected sectors. In order to derive the light curves of TIC 202431888, time extraction, PDCSAP (Pre-search Data Conditioning Simple Aperture Photometry) flux values (F_i) and conversion of the magnitude values (m_i) were performed by using the formula as follows.

$$m_i = -2.5 \log F_i, \tag{4.1}$$

To analyze the *TESS* light curves of the candidate stars, the Fourier analysis and least-squares fitting method were employed to extract the dominant frequencies from the dataset. The `PERIOD04` software package (Lenz & Breger, 2005), which is specifically designed for analyzing time-series to determine the frequencies of periodic signals, was used for this technique. The least-square fitting formula was applied to the input data set, which produce an estimate of frequency and amplitude ($F1$)

from the periodgram, therefore this data is used as starting points for obtaining a least squares fit to the time-series data. Least square fitting formula:

$$f(t) = Z + \sum A_i \sin(2\pi(\Omega_i t + U_i)), \tag{4.2}$$

where Z is the zero level of magnitudes, A_i is the amplitude of the corresponding frequency, Ωi is the frequency value, t is time, and U_i is the phase of the given frequency. It measures the sum of sinusoidal oscillations. Each term in the summation represents a sinusoidal component with an amplitude, frequency and phase. The function $f(t)$ provides the value of the sum of these sinusoidal oscillations at any given time, which is used to model periodic phenomena with multiple frequency components. The difference between the best fit sinusoid and the original time-series data (residuals) allowed the search for additional significant signals that are present (pre-whitening). This is achieved by employing the signal-to-noise ratio: $S/N > 4$ threshold adopted as a criterion for the candidate stars, following the approach by Lenz & Breger (2005). During the analyses, the Rayleigh criterion was used to determine the minimum angular separation between two point sources that can be resolved by an optical instrument. The Rayleigh criterion is given by:

$$\theta = \frac{1}{\Delta T} \tag{4.3}$$

Equation 4.3 represents θ as the angular resolution, ΔT is the difference between the initial and final time taken for the extraction. If the peaks representing different frequencies are separated by a distance greater than the Rayleigh criterion value, it indicates that these frequencies are resolved and can be reliably identified as distinct pulsation modes. On the other hand, if the peaks are closer together than the Rayleigh criterion, they might overlap, making it challenging to confidently determine individual frequencies. This is important because the frequency separation between pulsation modes provides information about the internal structure and physical properties of the star (Kepler, 2008).

For TIC 202431888, the Rayleigh criterion was set at 0.002123 to separate genuine harmonics and combination frequencies by following equation 4.3.

Table 4.2: Parameters of the resulting frequencies of TIC 202431888.

ID	$f(\mathrm{d}^{-1})$	A(mag)	Phase	S/N
f_1	19.318549(34)	0.00094(1)	0.07770 (43)	35
f_2	22.101419(69)	0.00005(2)	0.97737 (88)	17
f_3	3.32822(95)	0.00003(2)	0.92816(120)	10
$f_4 \approx 2f_3$	6.65872(115)	0.00003 (2)	0.17382 (145)	10
f_5	11.74557(250)	0.00002(3)	0.336751 (315)	5
f_6	3.11397(148)	0.00002(3)	0.29974(188)	6
$f_7 \approx f_5 - f_3$	8.42079(147)	0.00002 (3)	0.57757(185)	9
$f_8 \approx f_4$	6.63581 (152)	0.00002 (3)	0.12753(213)	8
$f_9 \approx 2f_1 - f_4 - f_7$	23.54957(169)	0.00001(3)	0.01854 (213)	7
$f_{10} \approx f_4 + f_{10}$	15.06462(212)	0.00001(3)	0.85062(212)	7

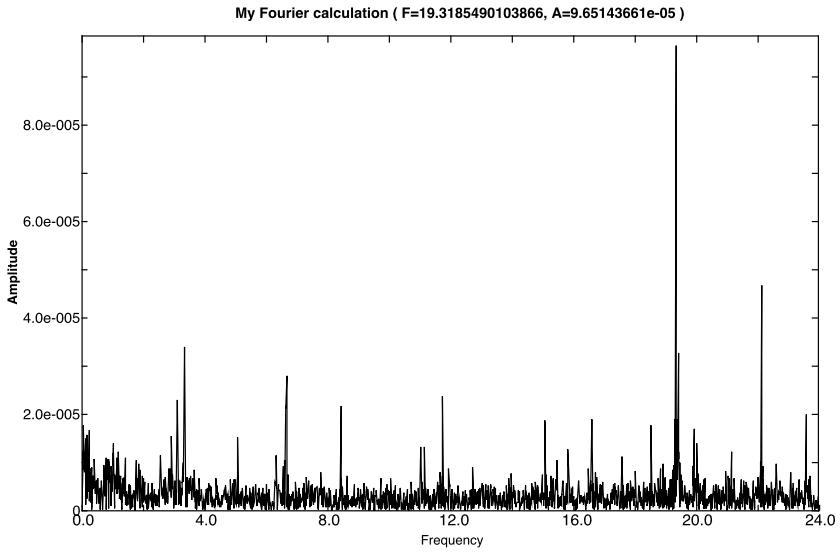


Figure 4.2: The computed amplitude spectra of TIC 202431888 from the *TESS* photometry in the sectors 57 and 58.

The frequency analysis of the *TESS* photometry yielded several genuine, harmonics, and combination frequencies. According to the results, the highest peaks are found to be at $f_1 = 19.32$ d^{-1} and $f_2 = 22.10$ d^{-1}, along with a few combinations and harmonics which are represented in Fig 4.2. The resulting frequencies are listed in Table 4.2.

4.2 Ground-based Spectroscopic Observations

4.2.1 Spectroscopic Data Analysis of TIC 202431888

It is essential to obtain a high-resolution spectra to enable the identification of fine spectral features, for precise measurement of radial velocities, and in-depth study of stellar atmospheres. The ability to discern closely spaced lines is important to derive fundamental stellar parameters, including $T_{\rm eff}$, $\log g$, metallicity, and $v \sin i$, by examining detailed features present in the spectra.

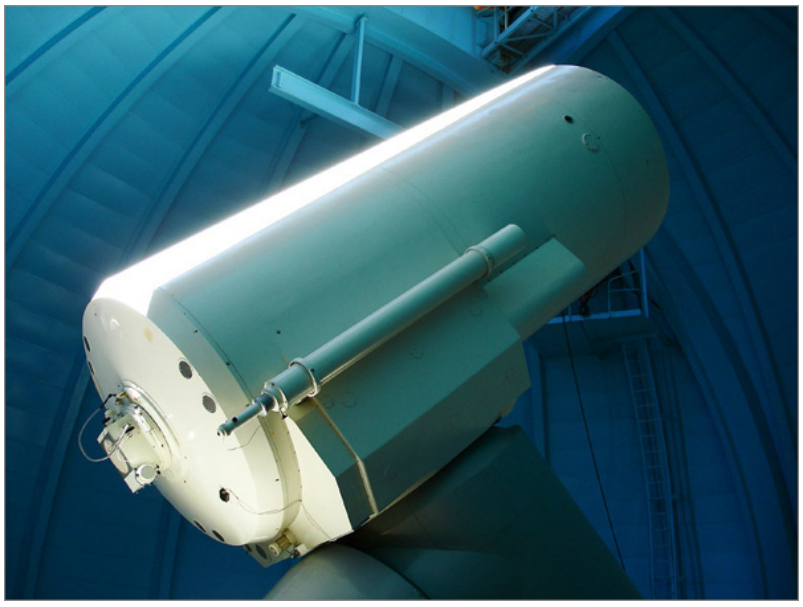


Figure 4.3: 2m RCC telescope at NAO-Rozhen IANAO,PenchoMarkishki (2023).

Therefore, the echelle spectrograph, ESpeRo, mounted on the 2-m RCC telescope at NAO-Rozhen (see Fig 4.3) was motivated by the need for high-resolution spectra for the Maia star TIC 202431888 to comprehensively analyze the spectral properties of the target. The acquired spectra cover a broad spectral range from 4 000 Å to 8 900 Å with a spectral resolution of approximately 35 000, particularly around the Balmer line, Hα, while maintaining a signal-to-noise ratio (S/N) of approximately 90 ensured reliable data quality (Stateva et al., 2010; Tomov et al., 2018; Avramova-Boncheva et al., 2022). To process the spectra we used the `IRAF` standard procedures (Tody, 1986) including bias subtracting, flat-fielding and wavelength calibration. The final spectra were adjusted to heliocentric wavelengths.

As TIC 202431888 is a hot star, the spectrum exhibits limited number of lines such as HI, He I, FeII, MgII, TiII, CrII. To obtain the atmospheric parameters we relied on the Balmer line, Hα. The best fit of Hα for the case of TIC 202431888 was

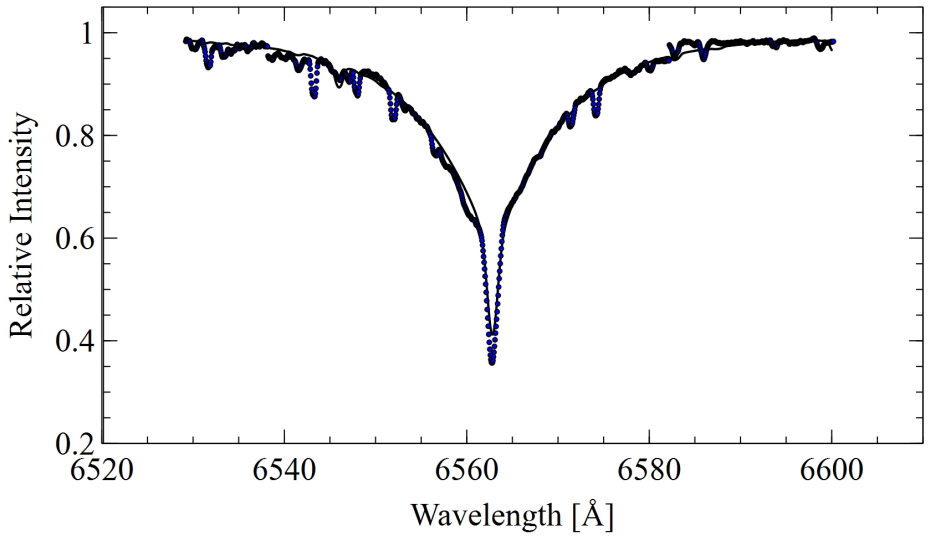


Figure 4.4: The observed (dots) and synthetic (solid line) spectra of TIC 202431888 for the Balmer line, Hα.

achieved for the atmosphere model with $T_{\rm eff} = 12\,325$ K, $\log g = 4.0$ (see Fig 4.4).

For determining the projected rotational velocity, we focused on Mg II $\lambda\,4481$ Å line. Analysis of the spectral line of Mg II $\lambda\,4481$ Å and certain Fe lines revealed optimal agreement between the synthetic and observed profiles for the projected rotational velocity, yielding $v \sin i = 30$ km s^{-1} (see Fig 4.5 and Fig 4.6).

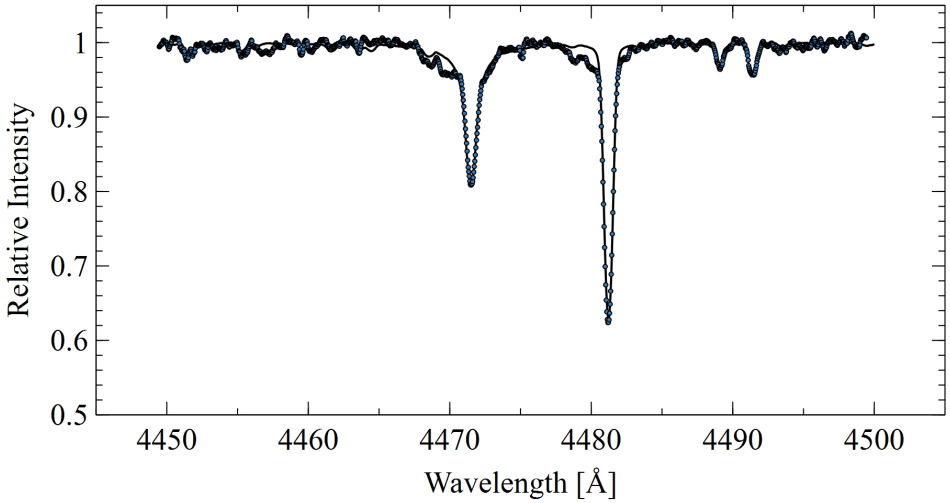


Figure 4.5: The same as in Fig 4.4 but for the region of He I $\lambda\,4471$ Å and Mg II $\lambda\,4481$ Å.

The relative strength of these spectral lines is a good indicator for the effective temperature, as these lines come from the same atomic transition, but only in a different

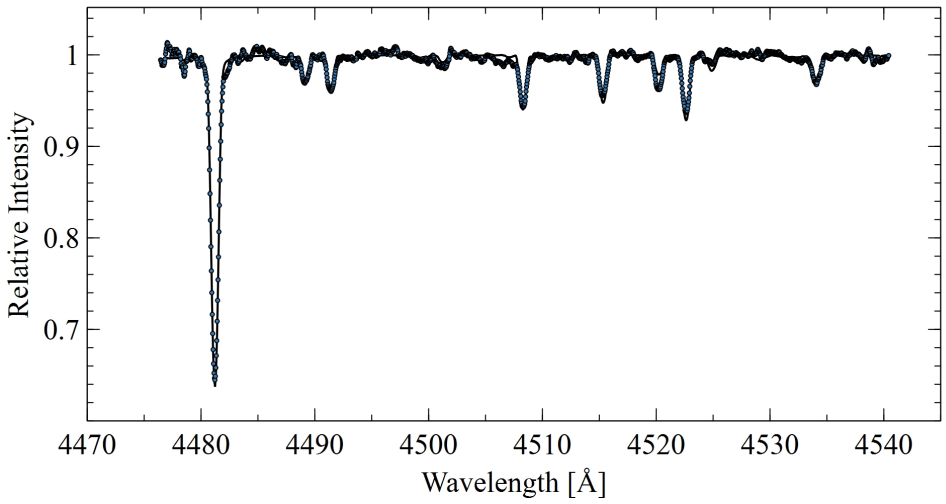


Figure 4.6: The same as in Fig 4.4 but for the region around $\lambda\,4500$ Å.

ionisation level. For the determination of the atmospheric parameters $T_{\rm eff}$, $\log g$, we employed the synthetic spectra method. This approach proves to be a highly effective tool for deriving atmospheric parameters, velocities, and chemical abundances of pivotal elements within stellar atmospheres. It involves a direct comparison between the observed spectrum and the synthesized spectrum, calculated based on an adopted model atmosphere. Among the most successful codes, `SYNSPEC`, developed by Hubeny et al. (1994) stands out, with the latest version being `SYNSPEC 54` (Hubeny & Lanz, 2017; Hubeny et al., 2021). We used Kurucz LTE stellar atmosphere models calculated under `ATLAS 12` code (Kurucz, 1993). Assuming the microturbulence to be $2\,{\rm km\,s^{-1}}$, a typical value for MS stars. The VALD atomic line database (Kupka et al., 1999) was used to create a line list for the synthetic spectra.

Our derived results for the atmospheric parameters $T_{\rm eff}$ and $\log g$ align with those previously published in the literature by Huang et al. (2010).

Through the synthetic procedure, we had the opportunity to ascertain the chemical abundances of selected elements within the stellar atmosphere of TIC 202431888. Our findings indicate that He exhibits a solar abundance, whereas Fe and Mg demonstrate slightly lower abundances than solar, with $[N/H] = -0.06$ for Mg and $[N/H] = -0.07$ for Fe. The lines of Cr II and Ti II are well-fitted assuming these elements are underabundant, with $[N/H] = -0.53$ for Cr and $[N/H] = -0.48$ for Ti. Here, $[N/H]$ represents the logarithmic ratio of the abundance of the element N_{el} to the number density of hydrogen N_H relative to the solar values $N_{el_\odot}$:

$$[N/H] = \log(N_{el}/N_H) - \log(N_{el_\odot}/N_H). \tag{4.4}$$

4.2.2 The location of TIC 202431888 on the HR Diagram

A spectral energy distribution (SED) by use of a Virtual Observatory SED Analyzer (VOSA) (Bayo et al., 2008), SED analysis were carried out to predict the location of the Maia star, TIC 202431888. The `Kurucz ODFNEW/NOVER` atmosphere models (Castelli & Kurucz, 2003)) and `PARSEC1.2` (Bressan et al., 2012) model in the SED analysis were fit to the photometric and calculated stellar parameters.

For the HR Diagram, the model input parameters were set to range between $T_{\rm eff}$ = 11 000 K, and $T_{\rm eff}$ = 12 500 K, and the $\log L$ range was adjusted between 2.2971± 0.041. The distance was adopted as 171.253 pc based on the DR3 (Collaboration et al., 2023) parallax.

The extinction of the star was adjusted at $A = 0.^m$ 7395 (Schlafly & Finkbeiner, 2011) by using the Galactic Dust Reddening and Extinction interface of NASA/IPAC Infrared Science Archive.

The metallicity value is assumed as solar abundance. The best fit values of the $T_{\rm eff}$ and log g were computed between the range 11 000± 125 K and at 4±0.25 dex respectively. The mass of TIC 202431888 was adopted to be M= 3.191$M_\odot$ from the *TESS* Input Catalogue (Stassun et al., 2018).

The mass range was set between 3.19 $M_\odot$ and 3.5 $M_\odot$ as input parameters. The $Vgfb$ (goodness of the fit) of the analyses was calculated at 9.35, which suggests a satisfactory fit in relation to the model limit of 15.

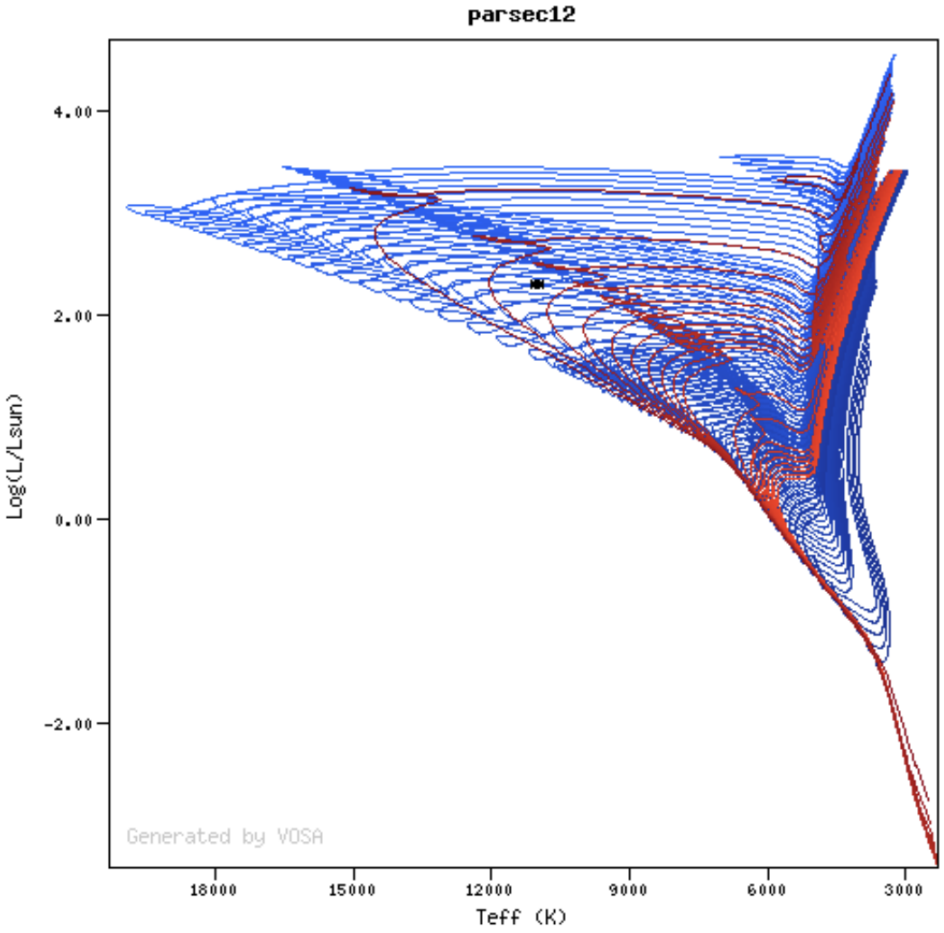


Figure 4.7: The evolutionary track of TIC 202431888 and its location.

The isochrones in the HR diagram presented in Fig 4.7 were obtained by applying the fitted stellar parameters to the stellar models. The evolutionary track of TIC 202431888 and its location are presented with the model (`PARSEC1.2`; stellar tracks and isochrones with the PAdova and TRieste Stellar Evolution Code (Bressan et al., 2012) isochrones for a given range of stellar input parameters. Isochrones and tracks are presented in the range between 0.5 $M_{\odot}$ and 5.8 $M_{\odot}$.

Chapter 5

Summary, Discussion and Conclusions

5.0.1 Summary

In this thesis, a comprehensive study of the *TESS* Maia-type star TIC 202431888 is presented. In order to investigate the Maia-like features of the star, the *TESS* photometry and ground-based high-resolution spectroscopy were used. The `PERIOD04` (Lenz & Breger, 2005) software was used to perform the frequency analysis.

Based on the analysis of the *TESS* time-series, the peaks with the highest amplitude were determined at $f_1 = 19.32\ d^{-1}$ and $f_2 = 22.10 d^{-1}$, along with a few combinations and harmonics (see Table 4.2 and Fig 4.2). Accordingly, the resulting frequencies correspond to an f-value within and above 20 d^{-1} that is given for Maia-type stars (Balona & Ozuyar, 2020). However, the dominant frequency of β Cephei-type stars is known to reach as high as 20 d^{-1}. Therefore, our study also confirms that TIC 202431888 does not meet the frequency range requirements for being classified as a β Cephei-type variable. What is more, Maia-type stars share common characteristics more closely with δ Scuti-type stars, in accordance with their frequency distribution. Our study did not include photometric mode identification modelling for TIC 2024318888 since obtaining such low-amplitudes through multi-colour ground-based observations can be a challenge, but long-term high-resolution spectral observations would be a solution to the problem.

To determine the stellar atmospheric parameters of TIC 202431888, a method of direct comparison was employed to compare the observed spectrum with the synthesized spectrum, which was calculated using a model atmosphere. This was achieved by using the most up-to-date `SYNSPEC 54` code (Hubeny et al., 2021) and Kurucz LTE stellar atmosphere models calculated with the `ATLAS 12` code (Kurucz, 1993). The synthetic procedure enabled us to determine the chemical abundances of selected elements within the stellar atmosphere of TIC 202431888. Due to the fact that TIC 202431888 is a B9-type star, the acquired spectrum showed a limited number

of lines like HI, He I, FeII, MgII, TiII, and CrII. The Balmer line, Hα , was therefore our primary line for obtaining the atmospheric parameters, and we emphasized the Mg II λ 4481 Å line to determine the projected rotational velocity. According to the data, He has a solar abundance, but Fe and Mg have slightly lower abundance values than the solar abundance, with $[N/H] = -0.06$ for Mg and $[N/H] = -0.07$ for Fe. Assuming that Cr II and Ti II are underabundant, the lines are well-represented with $[N/H] = -0.53$ for Cr and $[N/H] = -0.48$ for Ti. The logarithmic ratio of the abundance of N_{el} to H N_H to Hydrogen N_H in relation to solar values is represented by $[N/H]$.

The atmospheric parameters $T_{\rm eff}$ and $\log g$ that we have derived correspond to those published in literature by Huang et al. (2010). The fit of Hα was in the best agreement with the atmosphere model for the values of $T_{\rm eff} = 12\,325$ K, and $\log g = 4.0$ (see Fig 4.4). However, the projected velocity value derived $v \sin i = 30$ km s^{-1}, is lower than the values reported in the literature such as $v \sin i = 42$ km s^{-1}, by Royer et al. (2007), $v \sin i = 44$ km s^{-1} by Balona & Ozuyar (2020), and $v \sin i = 49$ km s^{-1} by Huang et al. (2010).

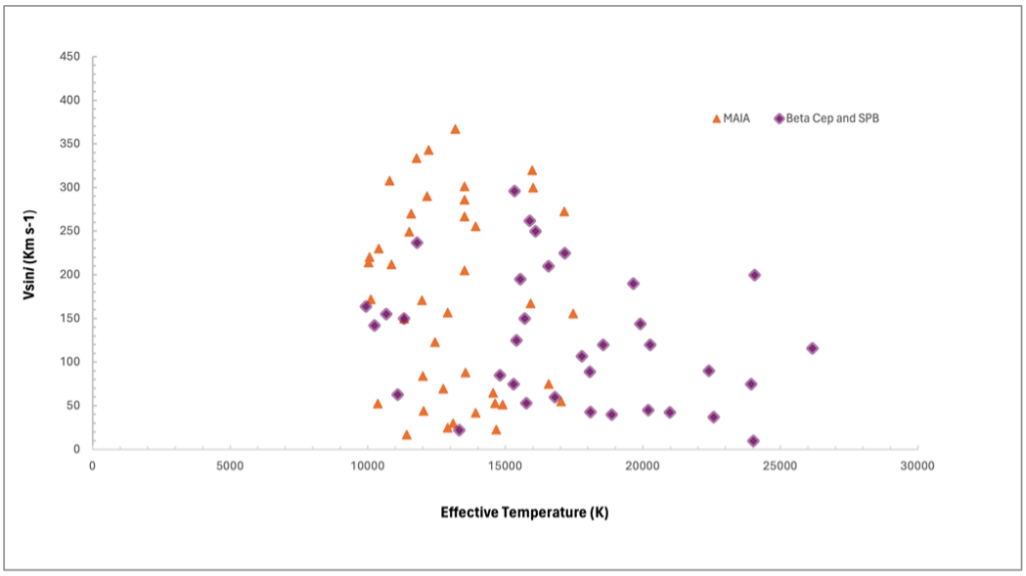


Figure 5.1: A comparison of Projected rotational velocities for Maia, β Cephei and SPB-type stars in the same effective temperature range.

It is evident that Maia stars do not rotate as fast as β Cephei or SPB stars. However, a comparison of the $v \sin i$ values of a list of Maia stars with the ones for β and SPB-type stars is presented in Fig 5.1.

As can be seen from Fig. 5.1, Maia candidates have higher $v \sin i$ values than both other groups. Balona & Ozuyar (2020) suggest that these objects could be a combination of δ Scuti and a non-pulsating B-type star. Although the star TIC 202431888

is not included in the category of fast rotating stars, it is worth considering the possibility of binarity effect or the existence of a planet orbiting it. Additionally, Daszyńska-Daszkiewicz et al. (2017) investigated three possible factors that could explain the rapid rotation in Maia stars. At high frequencies, it appears that instability can be obtained without rapid rotation only if there's a significant increase in opacities and only for high degree modes, and it is clear that there is significant uncertainty and no definite conclusions can be made at this point.

Furthermore, massive stars often exist in multiple systems, adding complexity to theoretical uncertainties due to interactions and mass transfer (Moe & Di Stefano, 2017). TIC 2024318888 is a spectroscopic binary star, and our study primarily focuses on the spectroscopy and photometry since directly determining the semi-major axis is not feasible in the case of spectroscopic binaries. Doppler shift measurements provide information about the orbital velocities of the member stars, but only in their radial components and it becomes challenging to ascertain the inclination of the orbit relative to our line of sight. This limitation restricts the amount of information we can extract essentially, it is not possible to differentiate between a slow-moving binary observed edge-on and a fast moving binary seen nearly face-on, where only a small component of the orbital motion aligns with the line of sight. It is extremely difficult to obtain these amplitudes in ground-based observations. Long-term high-resolution spectral observations are necessary for the solution to this problem.Despite challenges related to rotation, metallicity, mass loss, and magnetic fields, studying massive stars in multiple systems has been valuable for refining model parameters Mahy et al. (2020). For TIC 202431888, the list of orbital parameters is presented in Table 5.1.

Table 5.1: Orbital Paramets from SB9

			SB9			by Huang et al. (2010)			
HD	**P (days)**	**e**	**K1 (km/s)**	**K2 (km/s)**	γ **(km/s)**	**Vr(N1) (km/s)**	**Vr(N2) (km/s)**	**ΔVr (km/s)**	Detected
2054	48.3	0.38	30	...	3	-14	-7	7	n

The most recent study on an elemental abundance study of the star Maia itself showed that the significant underabundance of He and overabundance of Mn in the atmosphere of Maia, reported by (Renson & Manfroid, 2009), does not seem to be a typical He-weak star, nor a classical HgMn star; it may rather be a phosphorus and Ga-rich star. In addition, Balona et al. (2015a, 2016) determined the parameters

for Maia variables candidates KIC 4939281 and EPIC 202061002 classified to be SPB/Maia-type stars with $T_{\rm eff}$ found to be $18\,900 \pm 660$ K, $\log g$ determined to be 4.16 ± 0.17, and [Fe/H] measured at -0.4 ± 0.1. These values provide key insights into the characteristics of SPB/Maia-type stars.

5.0.2 Discussion on the MAIA Classification Conundrum

Pulsating stars in the HR Diagram are classified into different classes. Although majority of those classes have been confirmed and well-studied, some have not been well-understood, like the objects commonly and historically referred to as Maia variables (MAIA). The presence of Maia group was first suggested many decades ago (Struve, 1955) due to pulsating behavior of the prototype star, Maia itself, which was not suggested by the models in between the instability strips. Following this suggestion, several members of this class were observed with anomalous pulsational characteristics between δ Sct and β Cephei instability strips as seen in Figure 5.2.

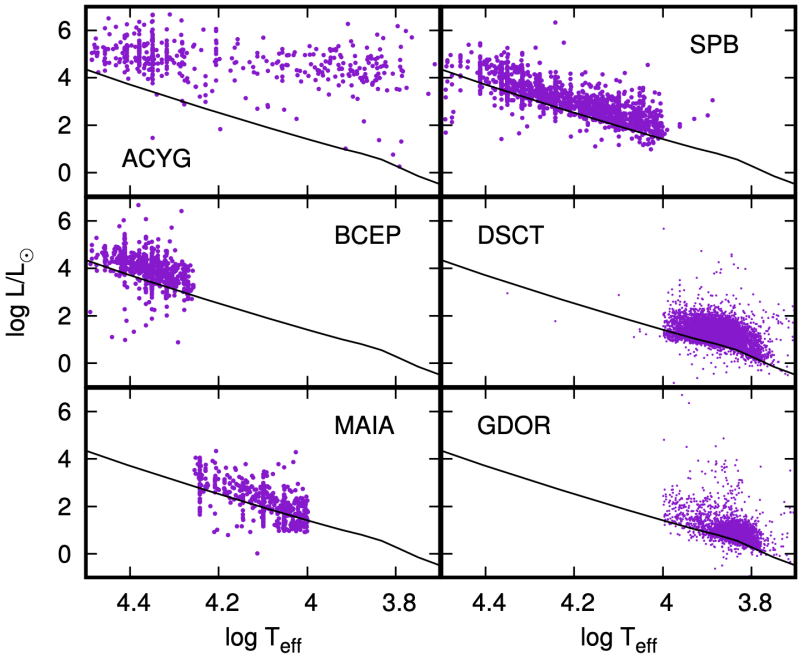


Figure 5.2: The location of certain pulsating stars in the H-R diagram. Solid Lines refer to Zero-Age Sequence Models from Bertelli G. (2009).

In subsequent periods, photometric observations from both ground-based and space-based sources bolstered the idea that there would be a new group of variable stars (Balona, 2023a). The fact that other stars showed such changes in the region where pulsations were not expected to be seen in the HRD led the idea that this new group

should be evaluated separetely. Indeed, *TESS* observations have revealed that stars with frequencies exceeding 5 d^{-1} have been observed throughout the main sequence, including the well-known β Cephei and δ Sct stars (Balona & Ozuyar, 2020; Balona, 2023a).

The main challenge is that the Maia variables are main sequence mid- to late B-type stars which pulsate in multiple high frequecies very similar to δ Sct stars (Balona et al., 2015b, 2016). The distinction of instability strips that pulsating stars are located on due to their hybrid frequency variations are the main concerns why Maia stars have not been considered to be in their own instability zone. SPB stars can be described as Maia stars with a preference for low frequencies, just like γ Dor stars with δ Sct stars with a preference for low frequencies.Thus, it is no longer possible to distinguish current variability groups.

Mode selection may also be determined by the difference between β Cep and SPB variables within the same temperature range. The distinction of SPB and β Cep stars are also arbitrary that may lead to misclassification of the new stars. For instance, instability strip of δ Sct stars merges to Maia variables location and extends to the cool end of the β Cep stars in the HR diagram. Another example indicated by the recent study is that the instability strips of γ Dor stars also lie within the instability strip of δ Sct, while the low- frequency pulsating stars located beyond the cool edge SPB instability strip merge with the γ Dor stars region (Balona, 2023b,a).

The origin of their driving mechanisms is essential for understanding Maia stars, cool SPB stars, and the merging of different variability groups. The significance of discovering the widespread distribution of starspots in the entire main sequence should not be overlooked since surface convection becomes present in all A and B stars, however it could be more than just a factor. This is why it's important to have a clear understanding of the types of physical phenomena that occur in stellar layers for A and B stars. Also, It has been suggested that Maia stars are just rapidly rotating SPB stars (Salmon et al., 2014), but this is not supported by $v \sin i$ measurements by Balona & Ozuyar (2020). Recently, it has been confirmed that Maia stars have frequencies that range widely, and high frequencies are not always linked to rapid rotation (Balona, 2023a) based on the *TESS* observations of 519 main sequence stars in 1-65 sectors.

In addition, the Maia stars merge with the β Cep stars at when they reach high temperatures and with the δ Sct stars at when they reach at lower temperatures. Accordingly, The MAIA class's definition was corrected by setting a limit of $T_{\rm eff}$

between 10000 K, and 18000 K (Balona, 2023a).

5.0.3 Conclusions

The photometry of the *TESS* satellite was used to detect low amplitude and high frequency variations that are not visible through ground-based observations for the late B-type star TIC 202431888. These frequency variations have been confirmed to vary differently from those in the upper instability zone, and TIC 202431888 is classified as a Maia-type variable star with low amplitude and high frequency values that also categorizes the star under MAIAU sugroup suggested by Balona (2023a).

Photometric mode identification of TIC 202431888 was not achievable using current mode identification models, which are only useful for stars with high amplitude changes due to their extremely small frequency amplitudes (Ulusoy et al., 2013). This reason led us to the conduct of spectroscopic observations of the star in order to obtain fundamental stellar parameters and metallicity. the metallicity of TIC 202431888 complies with Maia-like physical features except for having slightly low Fe and Mg values compared to solar values. It's possible that the change in opacity in the stellar atmosphere could be one reason, and it could mean that a different pulsating mechanism has probably arisen in the star. Furthermore, the atmospheric parameters $T_{\rm eff}$ = 12 325 K, and $\log g$ = 4.0 derived from the high-dispersion spectra for TIC 202431888 are also consistent with the range defined for the MAIA class achieved by restricting $T_{\rm eff}$ between 10000 K, and 18000 K (Balona, 2023a).

All in all, it is a fact that the Maia phenomenon has existed since 1955. Stars between in the upper main sequence and δ Scuti range that differ from these classes, have been included in a group called MAIA. Thus, it is crucial to conduct a thorough analysis of every star. The creation of this group's literature provides significant guidance for theoretical studies examining the location of these stars in the instability zones.

We conclude that, the current stellar models and observations, along with the reasons stated above, are required a complete revision of the upper main sequence instability groups with their own pulsational driving mechanisms since these stars will continue to be referred to as MAIA by their observed distinctive features which are contrary to current models, until accurate classification distinctions for instability regions are established.

Bibliography

Adassuriya J., 2022, Ph. D. Thesis

Aerts C., 2021, Reviews of Modern Physics, 93, 015001

Aerts C., Kolenberg K., 2005, Astronomy & Astrophysics, 431, 615

Aerts C., Christensen-Dalsgaard J., Kurtz D. W., 2010, Asteroseismology. Springer Science & Business Media

Aliçavuş F. K., Handler G., Chowdhury S., Niemczura E., Jayaraman R., De Cat P., Ozuyar D., Aliçavuş F., 2024, arXiv preprint arXiv:2404.16988

Allen C. W., Cox A. N., 2000, Allen's astrophysical quantities. Springer Science & Business Media

Anders E. H., et al., 2023, arXiv preprint arXiv:2306.08023

Antoci V., et al., 2014, The Astrophysical Journal, 796, 118

Apellániz J. M., 2006, The Astronomical Journal, 131, 1184

Avramova-Boncheva A., Korhonen H., Stateva I., Antonova A., 2022, in Cambridge Workshop on Cool Stars, Stellar Systems, and the Sun. p. 29

Baker N., Kippenhahn R., 1962, Zeitschrift fur Astrophysik, 54, 114

Baldry I. K., 1999, Ph. D. Thesis

Ball D. W., 2001, The Basics of Spectroscopy. Vol. 49, SPIE Press

Balmer J., 1897, Astrophysical Journal, vol. 5, p. 199, 5, 199

Balmforth N., Cunha M., Dolez N., Gough D., Vauclair S., 2001, Monthly Notices of the Royal Astronomical Society, 323, 362

Balona L., 2014, MNRAS, 437, 1476

Balona L. A., 2018, Monthly Notices of the Royal Astronomical Society, 479, 183

Balona L. A., 2019, MNRAS, 490, 2112

Balona L. A., 2023a, arXiv preprint arXiv:2301.09280

Balona L. A., 2023b, arXiv preprint arXiv:2310.09805

Balona L. A., Ozuyar D., 2020, MNRAS, 493, 5871

Balona L., et al., 2011, MNRAS, 413, 2403

Balona L., Baran A., Daszyńska-Daszkiewicz J., De Cat P., 2015a, MNRAS, 451, 1445

Balona L., Daszyńska-Daszkiewicz J., Pamyatnykh A., 2015b, MNRAS, 452, 3073

Balona L., et al., 2016, MNRAS, 460, 1318

Barbara A. Mikulski 2023, MAST Portal, https://mast.stsci.edu/portal/Mashup/Clients/Mast/Portal.html

Bayo A., Rodrigo C., y Navascués D. B., Solano E., Gutiérrez R., Morales-Calderón M., Allard F., 2008, Astronomy & Astrophysics, 492, 277

Bertelli G. Nasi E. G. L. M. P., 2009, Astronomy and Astrophysics, 508, 355

Bowman D. M., 2020, Frontiers in Astronomy and Space Sciences, 7, 578584

Bradt H., 2008, Astrophysics processes: the physics of astronomical phenomena. Cambridge University Press

Bressan A., Marigo P., Girardi L., Salashnic B., Dal Cero C., Rubelo S., Nanni A., 2012, MNRAS, 427, 127

Bruce MacEvoy 2013, Stellar Spectral Classification, https://www.handprint.com/ASTRO/specclass.html

Burssens S., et al., 2020, A&A, 639, A81

CNX O., 2023, The Spectra of Stars and Brown Dwarfs, https://courses.lumenlearning.com/suny-astronomy/chapter/the-spectra-of-stars-and-brown-dwarfs/

Campante T., et al., 2016, ApJ, 830, 138

Castelli F., Kurucz R., 2003, Modelling of Stellar Atmospheres, 210, A20

Catelan M., Smith H. A., 2015, Pulsating stars. John Wiley & Sons

Chang S.-W., Protopapas P., Kim D.-W., Byun Y.-I., 2013, The Astronomical Journal, 145, 132

Christensen-Dalsgaard J., 2003, Institut for Fysik og Astronomi, Aarhus Universitet, Denmark

Christensen-Dalsgaard J., 2004, SOHO 14 Helio-and Asteroseismology: Towards a Golden Future, 559, 1

Collaboration S., 2023, SDSS SkyServer: Spectral Types and Lines, https://skyserver.sdss.org/dr1/en/proj/basic/spectraltypes/lines.asp

Collaboration G., et al., 2018, VizieR Online Data Catalog, pp I–345

Collaboration G., et al., 2023, VizieR Online Data Catalog, pp I–361

Cox A. N., 2015, Allen's astrophysical quantities. Springer

Cunha M., Alentiev D., Brandão I., Perraut K., 2013, Monthly Notices of the Royal Astronomical Society, 436, 1639

Daszyńska-Daszkiewicz J., Walczak P., Pamyatnykh A., 2017, EPJ Web of Conferences, 160

Davies L., 2023, Hydrostatic Equilibrium Equation Solver, https://luke-davies.com/hydrostaticeq/

De Ridder J., et al., 2022, arXiv preprint arXiv:2206.06075

De Ridder J., et al., 2023, A&A, 674, A36

Degroote P., et al., 2009, A&A, 506, 471

Degroote P., et al., 2010, Astronomische Nachrichten, 331, 1065

Dhouib H., Prat V., Van Reeth T., Mathis S., 2021, A&A, 652, A154

Diaz-Cordoves J., Gimenez A., 1992, A&A (ISSN 0004-6361), vol. 259, no. 1, p. 227-231., 259, 227

Diaz-Cordoves J., Claret A., Gimenez A., 1995, A&A Supplement, v. 110, p. 329, 110, 329

Djorgovski S. G., Williams R., 2005, arXiv preprint astro-ph/0504006

Dopita M. A., Sutherland R. S., Dopita M. A., Sutherland R. S., 2003, Astrophysics of the Diffuse Universe, pp 289–324

Dupret M.-A., Thoul A., Scuflaire R., Daszyńska-Daszkiewicz J., Aerts C., Bourge P.-O., Waelkens C., Noels A., 2004, A&A, 415, 251

Dupret M.-A., Grigahcène A., Garrido R., Gabriel M., Scuflaire R., 2005, Astronomy & Astrophysics, 435, 927

Dziembowski W., Moskalik P., Pamyatnykh A., 1993, Monthly Notices of the Royal Astronomical Society, 265, 588

Eddington A. S., 1988, The internal constitution of the stars. Cambridge University Press

Eldridge J. J., Stanway E. R., 2022, Annual Review of A&A, 60, 455

Eyer L., Mowlavi N., 2008, in Journal of Physics: Conference Series. p. 012010

Eyer L., Holl B., Pourbaix D., Mowlavi N., Siopis C., Barblan F., Evans D., North P., 2013, arXiv preprint arXiv:1303.0303

FROGS 2023, Overview of Stellar Spectra, https://quarknet.fnal.gov/fnal-uc/quarknet-summer-research/QNET2010/Astronomy/

Frost E., 1902, ApJ, 15

Gabriel M., Noels A., Montalban J., Miglio A., 2014, A&A, 569, A63

Georgy C., Saio H., Meynet G., 2014, MNRAS: Letters, 439, L6

Glebocki R., Gnacinski P., 2005, VizieR online data catalog, pp III–244

Gough D. O., 1984, Philosophical Transactions of the Royal Society of London. Series A, Mathematical and Physical Sciences, 313, 27

Gough D., 1986, Hydrodynamic and magnetodynamic problems in the Sun and stars, p. 117

Gough D. O., 2012, Seismology of the Sun and the Distant Stars. Vol. 169, Springer Science & Business Media

Grigahcène A., et al., 2010, ApJ Letters, 713, L192

Guthnick P., 1913, Astronomische Nachrichten, 196, 357

Gutiérrez R., Rodrigo C., Solano E., 2006, in Astronomical Data Analysis Software and Systems XV. p. 19

Guzik J. A., Kaye A. B., Bradley P. A., Cox A. N., Neuforge C., 2000, ApJ, 542, L57

Habets G., Heintze J., 1981, A&AS, 46, 193

Hamann W.-R., Gräfener G., 2003, A&A, 410, 993

Hambly N., Davidson M., Collaboration G., et al., 2022, A&A

Handler G., 2012, arXiv preprint arXiv:1205.6407

Handler G., et al., 2004, MNRAS, 347, 454

Heger A., Fryer C. L., Woosley S. E., Langer N., Hartmann D. H., 2003, ApJ, 591, 288

Hernández A. G., et al., 2013, A&A, 559, A63

Hillier D. J., Miller D. L., 1998, ApJ, 496, 407

Hinkel N. R., Timmes F., Young P. A., Pagano M. D., Turnbull M. C., 2014, AJ, 148, 54

Hoffmeister C., Kholopov P., 1985, Soviet Astronomy, 29, 719

Holdsworth D. L., et al., 2024, Monthly Notices of the Royal Astronomical Society, 527, 9548

Huang W., Gies D. R., McSwain M. V., 2010, ApJ, 722, 605

Hubeny I., Lanz T., 2017, arXiv preprint arXiv:1706.01859

Hubeny I., Lanz T., Jeffery C., 1994, 20

Hubeny I., Prieto C. A., Osorio Y., Lanz T., 2021, arXiv preprint arXiv:2104.02829

Hubrig S., Briquet M., Schöller M., De Cat P., Mathys G., Aerts C., 2006, MNRAS: Letters, 369, L61

IANAO,PenchoMarkishki 2023, National Astronomical Observatory, Chepelare, Bulgaria, https://www.chetec-infra.eu/ta/tna-tels/ianao

Jackiewicz J., 2021, Frontiers in Astronomy and Space Sciences, 7, 595017

Janssens S., Shenar T., Mahy L., Marchant P., Sana H., Bodensteiner J., 2021, A&A, 646, A33

Jaschek C., Jaschek M., 1990, The classification of stars. Cambridge university press

Jenkins J., Chiozzi G., Guzman J. C., 2016.

Kaler J. B., 2011, Stars and their spectra: an introduction to the spectral sequence. Cambridge University Press

Kallinger T., Reegen P., Weiss W., 2002, A&A, 388, L37

Kamilla S., Roy G. S., Nayak M., Sharma N., Das R., Pattnaik S., 2011, Latin-American Journal of Physics Education, 5, 20

Karttunen H., Kröger P., Oja H., Poutanen M., Donner K. J., 2003, Fundamental Astronomy, pp 129–200

Karttunen H., Kröger P., Oja H., Poutanen M., Donner K. J., 2007, Fundamental astronomy. Springer

Kepler S. O., 2008, CoAst, Vol. 157, p. 24-28, 157, 24

Kilkenny D., 2013, Variable Stars – II. Pulsating stars, https://optical-astronomy.education/onewebmedia/var2.pdf

Kippenhahn R., Weigert A., Weiss A., 1990, Stellar structure and evolution. Vol. 192, Springer

Kirkpatrick J. D., 2005, Annu. Rev. Astron. Astrophys., 43, 195

Kupka F., Piskunov N., Ryabchikova T., Stempels H., Weiss W., 1999, A&AS, 138, 119

Kurtz D., 2022, arXiv preprint arXiv:2201.11629

Kurtz D. W., Jayaraman R., Sowicka P., Handler G., Saio H., Labadie-Bartz J., Lee U., 2023, Monthly Notices of the Royal Astronomical Society, 521, 4765

Kurucz R. L., 1993, Kurucz CD-Rom

Langer N., 2012, Annual Review of A&A, 50, 107

Langer N., 2022, arXiv preprint arXiv:2209.04165

Lanz T., Hubeny I., 2003, ApJ Supplement Series, 146, 417

Lara F. E., Rieutord M., 2011, A&A, 533, A43

Lara F. E., Rieutord M., 2012, A&A, 547, A32

Lata S., Yadav R. K., Pandey A., Richichi A., Eswaraiah C., Kumar B., Kappelmann N., Sharma S., 2014, MNRAS, 442, 273

Ledoux P., 1951, ApJ, 114

Ledoux P., Walraven T., 1958, Astrophysics II: Stellar Structure/Astrophysik II: Sternaufbau

Lehmann H., Scholz G., Hildebrandt G., Klose S., Panov K., Reimann H.-G., Woche M., Ziener R., 1995, A&A, 300, 783

Lenz P., Breger M., 2005, CoAst, vol. 146, p. 53-136, 146, 53

Lesh J. R., Aizenman M. L., 1978, Annual review of A&A, 16, 215

Letarte B., 2007, Chemical analysis of the Fornax dwarf galaxy. Rijksuniversiteit Groningen

Levy D. H., 1998, Observing Variable Stars: A Guide for the Beginner. Vol. 5, Cambridge University Press

Lindsay C. J., Ong J. J., Basu S., 2022, ApJ, 931, 116

Lund M. N., et al., 2021, ApJ Supplement Series, 257, 53

Maeder A., 2008, Physics, formation and evolution of rotating stars. Springer Science & Business Media

Maeder A., Meynet G., 2000, Annual Review of A&A, 38, 143

Mahy L., et al., 2020, A&A, 634, A118

Majidi F., Squicciarini V., Ulusoy C., Kgwatalala L., King C., Bonavita M., 2023, in 3rd Annual Conference of the African Astronomical Society (AfAS-2023. p. 13

Mariani G., 2012, AAVSO, c

Martin J. C., Morrison H. L., 1998, AJ, 116, 1724

Massey P., Puls J., Pauldrach A., Bresolin F., Kudritzki R. P., Simon T., 2005, ApJ, 627, 477

Matteucci F., 2001, The chemical evolution of the Galaxy. Vol. 253, Springer Science & Business Media

McNamara B., 1985, ApJ, 289, 213

Meynet G., Eggenberger P., Ekström S., Georgy C., Groh J., Maeder A., Saio H., Moriya T., 2013, European Astronomical Society Publications Series, 63, 373

Michielsen M., Pedersen M. G., Augustson K. C., Mathis S., Aerts C., 2019, A&A, 628, A76

Miglio A., Montalbán J., Dupret M.-A., 2007, MNRAS: Letters, 375, L21

Miglio A., Montalbán J., Noels A., Eggenberger P., 2008, MNRAS, 386, 1487

Mitchell H. B., 1976, The Physics Teacher, 14, 162

Modjaz M., Gutiérrez C. P., Arcavi I., 2019, Nature Astronomy, 3, 717

Moe M., Di Stefano R., 2017, The Astrophysical Journal Supplement Series, 230, 15

Morgan W. W., Keenan P., 1973, Annual Review of A&A, 11, 29

Moskalik P., 1995, in International Astronomical Union Colloquium. pp 44–55

Moskalik P., Dziembowski W., 1992, A&A, 256, L5

Motz L., Weaver J. H., 1989, in , The Unfolding Universe. Springer, pp 273–293

Mowlavi N., Barblan F., Saesen S., Eyer L., 2013, A&A, 554, A108

Mowlavi N., Saesen S., Semaan T., Eggenberger P., Barblan F., Eyer L., Ekström S., Georgy C., 2016, A&A, 554, A108

Mr Toogood's Physics 2023, Dead Stars - A-Level Physics Notes, https://www.alevelphysicsnotes.com/astrophysics/deadstars.php

NASA ESA L. H., 2021, James Webb Space Telescope Image, https://webbtelescope.org/contents/media/images/01F8GF8DK2PRY4FP9DA2XPQC8S

Pais A., 1979, Reviews of modern physics, 51, 863

Palacios A., Gebran M., Josselin E., Martins F., Plez B., Belmas M., Lebre A., 2010, A&A, 516, A13

Pamyatnykh A., 2003, in , Asteroseismology Across the HR Diagram. Springer, pp 97–107

Panov K., 1978, Acad. Sci., Astron. Inst, p. 19

Pavia D. L., Lampman G. M., Kriz G. S., Vyvyan J. A., 2014, Introduction to spectroscopy. Cengage learning

Paxton B., et al., 2018, ApJ Supplement Series, 234, 34

Paxton B., et al., 2019, ApJ Supplement Series, 243, 10

Pedersen M., Aerts C., Pápics P., Rogers T., 2018, A&A, 614, A128

Percy J. R., 2007, Understanding variable stars. Cambridge University Press

Percy J. R., Wilson J. B., 2000, PASP, 112, 846

Prša A., 2006, Univ. of Ljubljana, available in electronic form at http://phoebe. fiz. uni-lj. si

Puls J., Urbaneja M., Venero R., Repolust T., Springmann U., Jokuthy A., Mokiem M., 2005, A&A, 435, 669

Raman C., 1964, Current Science, 33, 355

Rechenberg H., 1982, The historical development of quantum theory. Vol. 1, Springer Science & Business Media

Renson P., Manfroid J., 2009, Astronomy & Astrophysics, 498, 961

Ricker G. R., et al., 2015, Journal of Astronomical Telescopes, Instruments, and Systems, 1, 014003

Rivinius T., 2013, in , Stellar Pulsations. Springer, pp 253–259

Robinson K., 2007, Spectroscopy: The Key to the Stars. Springer

Roxburgh I. W., 2004, in Stellar Structure and Habitable Planet Finding. pp 23–36

Royer F., Zorec J., Gómez A., 2007, Astronomy & Astrophysics, 463, 671

Saio H., Ekström S., Mowlavi N., Georgy C., Saesen S., Eggenberger P., Semaan T., Salmon S., 2017, MNRAS, 467, 3864

Salmon S., Montalbán J., Reese D., Dupret M.-A., Eggenberger P., 2014, A&A, 569, A18

Schlafly E. F., Finkbeiner D. P., 2011, The Astrophysical Journal, 737, 103

Serenelli A., et al., 2021, The A&A Review, 29, 4

Sharma A. N., Bedding T. R., Saio H., White T. R., 2022, MNRAS, 515, 828

Smartt S. J., 2009, Annual Review of A&A, 47, 63

Stassun K. G., et al., 2018, The Astronomical Journal, 156, 102

Stateva I., Niemczura E., Iliev I., 2010, Publications of the Astronomical Observatory of Belgrade, vol. 90, pp. 179-182, 90, 179

Sterken C., Jaschek C., 1996, light Curves of Variable Stars, a pictorial Atlas

Struve O., 1955, PASP, 67, 135

Struve O., Sahade J., Lynds C., Huang S., 1957, ApJ, 125, 115

Sullivan P. W., et al., 2015, The Astrophysical Journal, 809, 77

Suslick K. S., 2001, Sonoluminescence and sonochemistry, 3rd edn. Elsevier Science Ltd, Massachusetts, pp 1–20

Szabados L., Kurtz D., 2012

Szewczuk W., Daszyńska-Daszkiewicz J., 2017, MNRAS, 469, 13

Tanvir N. R., et al., 2009, Nature, 461, 1254

Tarrant N. J., 2010, PhD thesis, University of Birmingham

Tayler R. J., 1994, The stars: their structure and evolution. Cambridge University Press

Tennyson J., 2019, Astronomical Spectroscopy: An Introduction to the Atomic and Molecular Physics of Astronomical Spectroscopy. World Scientific

Tody D., 1986, in Instrumentation in astronomy VI. pp 733–748

Tomov T., Stateva I., Georgiev S., Konstantinova-Antova R., Stoyanov K., 2018, ATel, 11605, 1

Ulusoy C., et al., 2013, MNRAS, 428, 3551

Ulusoy C., et al., 2023, in 3rd Annual Conference of the African Astronomical Society (AfAS-2023. p. 109

Uytterhoeven K., et al., 2011, Astronomy & Astrophysics, 534, A125

Waelkens C., 1991, A&A, 246, 453

Waelkens C., 1996, A&A, 311, 873

Waelkens C., Rufener F., 1985, A&A, 152, 6

Weiss A., Hillebrandt W., Thomas H.-C., Ritter H., 2004, Cox and Giuli's Principles of Stellar Structure

White H. E., Baumgarte T. W., Shapiro S. L., 2012, ApJ, 752, 122

White T., et al., 2017, MNRAS, 471, 2882

Winckel H. V., 2016, Radiation Processes in Astronomy, https://onderwijsaanbod.kuleuven.be/syllabi/e/G0Y53AE.htm#activetab=doelstellingen_idp101536

Young D., 2012, ApJ, 673, 20

Appendix A

Terminology: Spectral lines are defined as the abbreviation of the element followed by a Roman numeral representing the of ionization. In this case the Roman number 'I' represents the element's non-ionized stage, 'II' represents single-ionized, etc. For example, an O I transition represents an atomic transition of non-ionized oxygen, and an O II transition corresponds to an atomic transition of single-ionized oxygen. In addition, the remaining wavelengths of the spectral lines are also recorded. The notation for the atomic transition of single-ionized oxygen, with a rest wavelength of 4169.22 Å, is written as 'O II λ4169.22'.